BENEMÉRITA UNIVERSIDAD AUTÓNOMA DE PUEBLA

INSTITUTO DE FÍSICA “LUIS RIVERA TERRAZAS”

“APPLICATION OF RANDOM MATRIX THEORY TECHNIQUES TO THE STUDY OF COMPLEX NETWORKS”

TESIS

QUE PARA OBTENER EL GRADO DE

DOCTOR EN CIENCIAS (FÍSICA)

PRESENTA

KEVIN PERALTA MARTÍNEZ

DIRECTOR DE TESIS

DR. JOSÉ ANTONIO MÉNDEZ BERMÚDEZ

No. de CVU: 1008062

MARZO 2025

Agradecimientos

Mi más sincero agradecimiento al Dr. José Antonio Méndez Bermúdez, mi asesor de tesis, por su invaluable guía durante este proyecto. Aprecio profundamente su comprensión y apoyo constante, particularmente durante los desafíos que representó iniciar esta investigación en medio de una pandemia global. Su compromiso académico y la libertad que me brindó para explorar temas relevantes han sido fundamentales para mi crecimiento profesional y formación como investigador.

Agradezco al Instituto de Física Ing. Luis Rivera Terrazas por ser el espacio donde culminé mi trayectoria académica: desde los cursos propedéuticos hasta la maestría y el doctorado en ciencias. Su formación de excelencia, las facilidades brindadas y el ambiente académico hicieron de esta etapa una experiencia profundamente enriquecedora y significativa.

Agradezco al Consejo Nacional de Humanidades, Ciencias y Tecnologías (CONAHCyT) por el apoyo económico brindado durante mis estudios de posgrado, el cual fue fundamental para la realización de esta investigación.

Agradezco profundamente a la Benemérita Universidad Autónoma de Puebla (BUAP), mi alma mater, por brindarme la formación académica y las herramientas que han hecho posible este trabajo.

A mis compañeros y amigos que caminaron junto a mí en esta travesía académica, mi más sincero agradecimiento. En especial a mi querido amigo David Abraham, cuyo compañerismo y afinidad hicieron de este proceso una experiencia compartida llena de aprendizaje y crecimiento mutuo. Igualmente, a mi colega y amiga Claudia Teresa, cuya experiencia y apoyo constante fueron de gran ayuda en momentos de presión, siempre dispuesta a guiarme y aliviar el peso de los desafíos.

Finalmente, y con profunda reverencia, extiendo mi gratitud al equipo fundamental de mi vida: mi familia. Sus palabras de aliento, sabios consejos, e incluso aquellos necesarios

regaños han sido tanto faro como sustento en cada desafío emprendido.

A mi madre, mujer de temple excepcional, cuyo amor incondicional ha sido el cimiento de todo lo que soy. Por su dedicación incansable en construir un camino de oportunidades para mí y mi hermana, por su profunda fe en Dios que me inspira a ser un hombre de convicción y voluntad inquebrantable: un millón de gracias.

A mi hermana, que con sincronía perfecta aparece para recordarme mi esencia cuando más lo necesito, y que con sus bromas y ocurrencias aligera mis preocupaciones.

Y sobre todo, a mi Señor Jesucristo, quien en su soberanía me guió a estos senderos de la física. A él entrego este logro, pues en sus manos está mi futuro, confiando en que su fuerza, fidelidad y amor nunca me faltarán.

A mi madre, Verónica,
portadora de la victoria.
Mujer virtuosa que edifica su casa.
Su estima sobrepasa a la de las piedras preciosas.
Mommy "piecitos santos".

A mi hermana, mi bolita.
Compañera de ocurrencias.
Mujer que actúa con sabiduría.

A mi Señor Jesús, El-Shaddai.
El Dios de las montañas.
Porque todo fue creado por él...y para él.

Aplicación de técnicas de teoría de matrices aleatorias al estudio de redes complejas

Resumen

En esta tesis nos dedicamos al estudio de propiedades estructurales, de autovalores y autovectores de redes complejas usando a la matriz de adyacencia en dos versiones: binaria y aleatoriamente pesada. Nos enfocamos en el estudio de propiedades estáticas y propiedades dinámicas. Con relación a propiedades estáticas realizamos el estudio de dos modelos de redes aleatorias:

- El modelo de grafos geométricos aleatorios dirigidos.
- El modelo de grafos hiperbólicos aleatorios no dirigidos.

En el contexto de ensambles de matrices aleatorias, realizamos el estudio de la probabilidad de supervivencia en un modelo base:

- El modelo de redes aleatorias tipo Erdös Renyi no dirigidas.

Usando matrices de adyacencia binarias, nos enfocamos en el estudio de cantidades topológicas o estructurales: el grado promedio, el índice armónico, índice de Randić, coeficiente local, y coeficiente global de clustering. Usando modelos de ensambles de la teoría de matrices aleatorias como referencia de matrices aleatorias pesadas, nos dedicamos al estudio estadístico de cantidades espectrales (de autovalores y autovectores): la razón entre espaciamientos de autovalores consecutivos, la razón entre espaciamientos de autovalores entre el autovalor vecino más cercano y su vecino más próximo, la razón de participación inversa de los autovectores, y la entropía de Shannon de los autovectores.
Particularmente, mostramos que para las cantidades espectrales estáticas es posible definir un parámetro de escalamiento que permite obtener curvas universales para los modelos de redes, definiendo así tres regímenes: estados localizados, la región de transición entre estados localizados a delocalizados, y estados totalmente delocalizados. Asímismo, mostramos que a tráves del grado promedio es posible caracterizar el comportamiento de la probabilidad de supervivencia de redes tipo Erdös Renyi.

Application of random matrix theory techniques to the study of complex networks

Abstract

In this thesis, we study the structural, eigenvalue and eigenvector properties of complex networks using their adjacency matrix representation in two different versions: binary and randomly-weighted. We focus on the study of static and dynamical properties. Regarding static properties, we study two random network models:

- The directed random geometric graph model.
- The undirected random hyperbolic graph model.

In the context of random matrix ensembles, we perform the study of the survivial probability in a reference model:

- The undirected Erdös Renyi random network model.

Using binary adjacency matrices, we focus on the study of topological or structural quantities (measures): the average degree, the Harmonic index, the Randić index, the local and global clustering coefficients. Using models of ensembles of random matrix theory as a reference of randomly-weighted adjacency matrices, we dedicate to the statistical study of spectral and eigenvector quantities: the ratio between consecutive eigenvalue spacings, the ratio between the nearest and next-to-nearest-neighbor spacings, the inverse participation ratio, and the Shannon entropy of the eigenvectors. Particularly, we show that for the static spectral and eigenvector measures it is possible to define a scaling parameter that allows to obtain universal curves for the random network models, and help us to define three different regimes of the network states: localization, localization-to-delocalization crossover, and full delocalization. Finally, we show that by using the average degree we can characterize the general behavior of the survival probability of Erdös Renyi random networks.

Publicaciones

Los resultados reportados en el Capítulo 4 fueron publicados en:

- Kevin Peralta-Martinez, J. A. Méndez-Bermúdez, "Directed random geometric graphs: structural and spectral properties", *Journal of Physics: Complexity* **4** (1), 015002 (2023).

Los resultados reportados en el Capítulo 5 fueron publicados en:

- Kevin Peralta-Martinez, J. A. Méndez-Bermúdez, José M. Sigarreta "Hyperbolic random geometric graphs: Structural and spectral properties", *Phys. Rev. E* **111**, 024309 (2025).

Los resultados reportados en el Capítulo 6 se encuentran en el manuscrito:

- Kevin Peralta-Martinez, J. A. Méndez-Bermúdez, "Survival probability in random networks" (2025).

Participación en eventos

- "Hyperbolic random geometric graph: A scaling analysis", Kevin Peralta-Martinez y J. A. Méndez-Bermúdez, Meeting on Complex Systems and Stochastic Processes, Guadalajara, Jalisco, México (2024).

- "Analysis of the correlation hole of the survival probability in network models", Kevin Peralta-Martinez y J. A. Méndez-Bermúdez, Random matrix theory and its applications, Cuernavaca, Morelos, México (2024).

Contents

List of Abbreviations and symbols

The following list describes the significance of abbreviations, acronyms and symbols used throughout this thesis work. The page of the first use of the abbreviation, acronym or symbol is also given.

`ER`	Erdös Renyi	(p. 5)
`RGG`	Random geometric graph	(p. 6)
`dRGG`	Directed random geometric graph	(p. 6)
`HRG`	Hyperbolic random graph	(p. 6)
`RMT`	Random matrix theory	(p. 7)
`GOE`	Gaussian orthogonal ensemble	(p. 8)
`GUE`	Gaussian unitary ensemble	(p. 8)
$\mathbf{A}$	Denotes a binary adjacency matrix	(p. 19)
G	Denotes graph	(p. 24)
Ω	Denotes connectance	(p. 22)
$R(G)$	Randić connectivity index	(p. 24)
$H(G)$	Harmonic index	(p. 24)
$V_x(G)$	Number of nonisolated vertices	(p. 25)
$\overline{C}(G)$	Local clustering coefficient	(p. 25)
$C_g(G)$	Global clustering coefficient	(p. 26)
$\mathbf{A_O}$	Denotes an orthogonal randomly-weighted adjacency matrix	(p. 30)
`RGE`	Real Ginibre ensemble	(p. 30)
$\mathbf{A_nH}$	Denotes a randomly-weighted non-Hermitian adjacency matrix	(p. 30)
`MRME`	Magnetic random matrix ensemble	(p. 31)

$\mathbf{A_H}$	Denotes a randomly-weighted Hermitian adjacency matrix	(p. 31)
λ_i, Ψ^i	Denote the $i-th$ eigenvalue and normalized eigenvector, respectively	(p. 32)
$r_{\mathbb{R}}$, $r_{\mathbb{C}}$	Ratio between consecutive level spacings, ratio between nearest-and next-to-nearest eigenvalue spacings, respectively	(p. 33)
IPR, S	Inverse participation ratio, Shannon entropy	(p. 33)
PE	Poisson ensemble	(p. 33)
$(\cdot)_{\mathrm{RGE}}$, $(\cdot)_{\mathrm{MRME}}$, $(\cdot)_{\mathrm{PE}}$, $(\cdot)_{\mathrm{GOE}}$	Denote the limit ensemble value of the quantity $(\cdot)$	(p. 34)
n	Number of nodes, also called size of the graph or network	(p. 36)
ℓ	Connection radius, parameter of the RGG model	(p. 36)
ℓ_0	Lowest bound of the support of the radii distribution of the RGG model	(p. 37)
α	Exponent of the radii Pareto distribution of the RGG. Exponent of the node radial coordinate density function of the HRG	(p. 37, 56)
$P(k)$	Degree distribution	(p. 39)
$P(\bar{k})$	Distribution of the normalized degree	(p. 39)
$\langle k \rangle$	Average degree	(p. 41)
ξ	Denotes a scaling parameter	(p. 49)
C, δ	Fitting constants	(p. 50)
$\mathbb{H}^2$	Hyperbolic plane	(p. 50)
ρ	Disk radius of the hyperbolic disk, parameter of the HRG	(p. 56)
K	Gaussian curvature	(p. 56)
ζ	Related to the Gaussian curvature $K = -\zeta^2$, parameter of the HRG	(p. 56)
β	Exponent of the power-law degree distribution of the HRG	(p. 58)

Chapter 1

Introduction

Historically, the emergence of graph theory traces back to the problem of the seven bridges of Königsberg in which Leonhard Euler in 1736 showed that it was not possible to visit all of the mainland banks of the city of Königsberg by crossing the seven bridges just once. He extracted the concepts of vertices and edges, representing the banks and bridges, respectively. Euler showed that the problem had a solution only if none or two vertices had an odd degree [1]. By abstracting this geometric problem, he laid the foundations of graph theory. Later, important fundamentals of graph theory were established with the study of enumeration of trees, and the Kuratowski and the Túran theorems [2]. Also in 1847 Gustav Kirchhoff used trees to describe current flow in electrical networks in the development of Kirchhoff's circuit laws as an important application of graph theory [3]. Then, in order to account for randomness in graphs, in 1951 Solomonoff and Rapoport introduced the first random graph model [4] (named *Erdös Renyi* model after further studies by Paul Erdös and Alfréd Renyi [5]) that set the development of a wide variety of random network models and laid the foundations of modern network science.

Today, networks have become tremendously useful for understanding the structure of systems across scales, containing a few elements or even millions. Depending on their construction principles, networks are broadly classified as *deterministic*, *random*, and *fractal* [6]. However, networks extracted from real-world systems often result in a large number of interconnected heterogeneous elements combining features from multiple categories of networks in a non-trivial way. These networks are, therefore, extremely difficult to analyze and are called *complex networks* [7].

Recently, random graphs, which are probabilistic models where links are added between

nodes according to some probabilistic rule, have gained much attention in mimicking properties of interest in complex networks and aiding in their understanding. Thus, much investigation has been done to understand structural properties of random networks and implement them to the study of real-world networks such as social networks, the World Wide Web (WWW), Internet, biological networks, power grids, word association networks [8, 10–12]; and many others. Additionally, some models have also been characterized and used within the view of statistical mechanics theory [13, 14] as a powerful resource to extend network theory.

Since random networks have become important for the understanding of global properties of real-world complex systems modeled by networks, our study focuses on analyzing the properties of random network models by applying some techniques used in the context of random matrix theory, which is discussed in Sec. 1.2.

1.1 Random network models

Since the introduction of the Erdös Renyi (ER) model and the limits. it has to fully describe specific characteristics of realistic networks such as scale-free degree distributions, high clustering, small-world properties, and the presence of communities; a wide variety of random network models has been introduced in order to amend for these attributes. Among the most popular models we can mention the preferential attachment model of Barabási and Albert [15] (able to reproduce the scale-free property), preferential attachment networks of Watts and Strogatz [16] (with the small-world feature), and the configuration model by Bollobás (for the generation of random graphs with a specified degree sequence). Interestingly, as a natural generalization of the ER model, Caldarelli et al. [17] and Söderberg [18] have proposed the construction of inhomogeneous graphs characterized by an attachment kernel and a fitness distribution (also called hidden variable graphs [19]) allowing the appearance of scale-free degree distributions and correlated structures. Among some applications of the Erdös Renyi model we can mention: epidemic modeling and percolation studies [20]. This reveals that despite the ER model is proved simplistic for the analysis of complex networks, it is still a crucial framework model with general applicability across disciplines. Therefore, the ER model serves as a useful tool for unifying concepts when analyzing different kinds of systems, bridging the gap between the formal mathematical study of networks and real-

world complex systems.

If the system under study is embedded in a geometric space (like road networks, power networks or networks of wireless communication devices) the best suited representation belongs to the so-called *spatial networks* [21]. The rising interest in spatial networks stems from their ability to capture the intrinsic interplay between structure and space, offering a more comprehensive understanding of real-world complex systems. The versatility of spatial networks extends across diverse applications, spanning a spectrum that includes transportation and urban planning, where understanding spatial relationships is pivotal for efficient design, to ecology, where the geographical distribution of species influences ecosystems. Additionally, in fields like epidemiology, the consideration of spatial connections becomes crucial for modeling the spread of diseases, while in telecommunications, the optimization of network infrastructure relies on an appreciation of the spatial relationships between communication nodes. One key aspect of geometric networks is their capacity to uncover hidden patterns, dependencies, and vulnerabilities that are often obscured in conventional network analyses [22, 23, 156]. In this respect, probably the most studied model of spatial networks is the random geometric graph (RGG) model introduced by Gilbert in 1961 [24]. Among many areas of study, random geometric graphs have been used for modelling worm epidemics in wireless, ad hoc networks, stochastic epidemics, rumor propagation, and design of wireless networks [25–27]. In particular, since the arrival of the RGG model different versions of the same have been proposed contrasting in boundary domains from unit circles and squares [8, 28–30] to d-dimensional spheres and squares [28, 31], etc. Since most of the real-world spatial networks are intrisically directed, models of directed RGGs, called dRGGs, have been explored in order to extend its applicability in the study of wireless networks and word association networks [8, 9]. However, Euclidean geometry of RGGs is not always apt to represent exponentially distant node locations or node similarity distances [14]. In this sense, for instance, some studies have shown that hyperbolic spaces show a more accurate interpretation of the structure of brain networks than Euclidean geometry at different scales [32,33]. As a natural extension of spatial networks, the hyperbolic random graph (HRG) model introduced in [14, 34] portraits the quality to represent nodes separated by exponential distances on the hyperbolic plane $\mathtt{H}^2$ as a stereographic projection of the positive hyperboloid, while simultaneously presenting scale-free degree distributions as in the original preferential attachment model, strong clustering, sparseness, community

structure, and self-similarity [156]. Moreover, because of the inherent real-world-like properties, due to negative curvature geometry, some possible applications of the HRG as a null model have been studied on brain dynamics, mapping of the Internet and link prediction [35–38]. Thus, for the relevance of these models in the modeling and understanding of complex networks, we study topological and spectral properties of the dRGG and the HRG models in the context of random matrix theory.

Furthermore, not only the properties of topological and static spectral properties of mostly undirected networks have been extensively analyzed, also the dynamical properties that inherit the structure of networks and graphs have attracted great interest in the studies of rumor spreading, glassy systems modelling with random regular graphs, the return or survival probability of random walks in scale-free trees, and random walks using weighted matrices with a dynamics described by a discrete time Markovian process [39–42]. In addition, studies of the random walk dynamics with long range interactions using fractional calculus has permitted to explore fractional diffusion in networks [43]. And as an extension, fractional quantum transport in ring graphs was also studied in [44] and serving to generalize dynamics based on continuous-time quantum walks [45]. Even more, more recently, Mellin-transformed d-path Laplacian operators have been implemented to the study of quantum transport and return probabilities of ring, complete and star graphs [46]. However, even though the static spectral properties of networks have been analyzed in the context of random matrix theory, their dynamics has not been taken into account in the same context. Hence, in this work we aim to contribute to the study of the dynamics of random networks by analyzing the ER random network model (as a conventional reference in the study of networks) within the framework of random matrix theory (RMT). That is, we focus on the analysis of the survival probability in terms of the inherent parameters of the ER network.

1.2 Random matrix theory

The origins of random matrix theory (RMT) can be traced back to Wishart in 1928 for statistical studies [47], later introduced by Eugene Wigner during the 1950s in the field of nuclear physics. In quantum mechanics the energy levels of a system are completely described by the eigenvalues of its Hamiltonian, but in the study of complex atom nuclei the knowledge of the Hamiltonian and to solve its eigenvalue equation may be quite difficult. Thus, Wigner surmised that the local statistical behavior of levels in a simple sequence

(levels with the same spin, parity, and some other conserved quantities) would be identical to the eigenvalues of a random matrix [48]. In this sense, Wigner introduced the concept of level distribution and showed that the eigenvalues were not independent and exhibited level repulsion [49]. Later Porter and Rosenzweig analyzed nuclear experimental data compiled by Harvey, Hughes and Moore [50, 51] and corroborated Wigner's conjecture to be very proximal to reality. This fact caused the development of random matrix ensembles invariant under symmetry groups as a statistical approach to the study of complex physical systems [52, 53]. As stated by Dyson, the statistical theory would not predict the detailed level sequence of any nucleus, but it would describe the general appearance and degree of irregularity of the level structure. In this way, the complex nucleus was pictured as a "black box" with large number of particles interacting with unknown laws [54]. Therefore, at the core of RMT is the idea that spectral distribution density in random matrices is in fact universal, meaning that it does not matter what is the specific type of matrix or its underlying physical system.

The classical matrix ensembles, also known as *Wigner classical ensembles* describe different types of symmetry in the underlying physical systems and are classified based on the nature of its matrix elements. These ensembles include the Gaussian orthogonal ensemble (GOE), the Gaussian unitary eensemble (GUE), and the Gaussian symplectic ensemble (GSE):

- GOE: Consists of squared $n \times n$ real and symmetric matrices. The matrix elements are independent random variables drawn from a normal distribution with mean zero and variance $2\sigma^2$ in the main diagonal, and variance σ^2 for the off-diagonal elements. This ensemble corresponds to systems with time-reversal symmetry and rotational symmetry.

- GUE: Consists of squared $n \times n$ complex hermitian matrices. The matrix has real elements in the diagonal and complex off-diagonal elements. Both real and imaginary parts are drawn from a normal distribution with mean zero and variance σ, resulting in diagonal elements with variance σ and off-diagonal elements with variance σ too. This ensemble has no time-reversal symmetry but keeps rotational symmetry.

- GSE: Consists of squared $n \times n$ quaternionic self-dual matrices. The matrix elements are real random variables in the diagonal and quaternionic random variables off-diagonal. All random variables have mean zero and variance σ. This ensemble

preserves time reversal symmetry but not rotational symmetry.

Today RMT has numerous applications across different fields, such as condensed matter physics, characterization of chaotic systems, financial markets, quantum gravity, and in mathematics for the analysis of the distribution of values of the Riemann zeta function [55,56], etc. Interestingly, one particularly suitable approach to address the relation between the structure and the dynamics of a networked system is given by RMT, for instance, the random Ising model or spin glass [57] seen as a network where nodes are spins and edges represent interactions between spins. Consequently, RMT is also a suitable framework for the study of random networks. Since random networks even though constructed with a fixed set of parameter values, have themselves a random structure; it is meaningless to study a single random network. Instead a statistical study of an ensemble of networks with the same average properties should be performed. In this sense, the use of RMT techniques might reveal universal properties, see e.g. [58–60], which are always of interest, as they allow to reduce the set of parameters describing the system and deduce its behavior from a few global parameters.

1.3 Methodology

It is possible to distinguish two approaches where RMT is applied to the study of complex networks:

(1) On the one hand, diluted versions of the classical RMT ensembles have been used to characterize ER-like networks. In this line of research the most studied RMT model is the diluted version of the GOE which serves as a null model of ER undirected networks, see e.g. [58–74]. Moreover, recently, diluted versions of the Gaussian Unitary Ensemble and the Ginibre Ensemble were used to study directed ER weighted networks [75].

(2) On the other hand, given a specific complex network model it is possible to design a corresponding RMT null (or reference) model. This approach has been used to study multilayer and multiplex networks [76, 77], bipartite networks [78], and mutualistic networks [79].

Specifically, while approach (1) does not consider the matrix structure representation of a network, approach (2) was designed to take it into account. However, we have to recognize

that approach (2) is mainly a numerical approach. Therefore, in this thesis we study spectral properties of different random network models and contribute to the analysis of dynamical properties within the second approach using as a mathematical tool the *adjacency matrix* that we define in the next chapter.

1.3.1 Thesis organization

In this work we study the topological structure, spectral properties, and the survival probability of some random network models using RMT representations. This work is divided in two parts:

- Part I: This part includes Chapter 2 through Chapter 5. In Chapter 2 we introduce the notion of degree, the different types of graphs according to the nature of their edges, and the topological quantities that we use to study two random network models in Chapter 4 and Chapter 5; namely, the directed random geometric graph model and the hyperbolic random graph model, respectively. In Chapter 3 we emphasize the importance of a RMT approach for the study of random networks and the straightforward connection between random matrix and adjacency matrix for the representation of random network models. Also, in this Chapter we define the standard RMT quantites that we use to characterize the directed random geometric graphs and the hyperbolic random graphs. In Chapter 4 we introduce the directed random geometric graph model, and perform a thorough numerical analysis of the topological and spectral properties of the model. Then we show relevant characterization of topological measures through the average degree, we also show that by use of the average degree we can find a scaling parameter for the spectral measures that permit us to characterize them across different network sizes. In Chapter 5 we define the hyperbolic random graph model, we also perform a numerical analysis of the topological and spectral properties of this model, again, by performing calculations over a large ensemble of binary (for topological quantities) and randomly-weighted adjacency matrices (for spectral quantities) in the context of RMT ensembles. Also for this model we show the existence of a scaling parameter for spectral measures.

- Part II: This part includes Chapter 6, where we define the ER model, and perform the analysis of the survival probability in the context of RMT. Also, in Appendix A

we include complementary results useful for the analysis of the survival probability of Chapter 6.

Finally, in Chapter 7 we present the conclusions of this Thesis work.

Part I

Topological and static spectral measures in random network models

Chapter 2

Classification, representation, and topology of networks

A complex system can be abstracted into a set of vertices, participant components of the system under study, and a set of edges or links, relationships between components, that form a network. Thus, a network can be thought of as the skeleton of a complex system. This permits us to identify and study many properties inherited by the structure of the object of observation. It is crucial to emphasize that depending on the application, vertices and edges may have different interpretations. Consequently, for the great flexibility that networks have in modeling systems of many interacting constituents, this chapter will classify and define networks and some important topological properties and measures as well as matrix representations of them.

2.1 Classification of graphs

A graph is a mathematical structure consisting of a set of vertices or nodes connected by edges or links, they are generally used to represent abstract relationships or connections between entities. The distinction between *graph* and *network* relies on application. While a *graph* is more mathematically based, a *network* typically refers to a real-world system of interconnected entities with applications ranging from exact to social sciences [15, 80–82], Fig. 2.1 shows the components of a network and depicts a possible application in biology. Here, for this thesis work, we must point out that the words *graph* and *network* are used interchangeably. However, since the analysis of complex systems

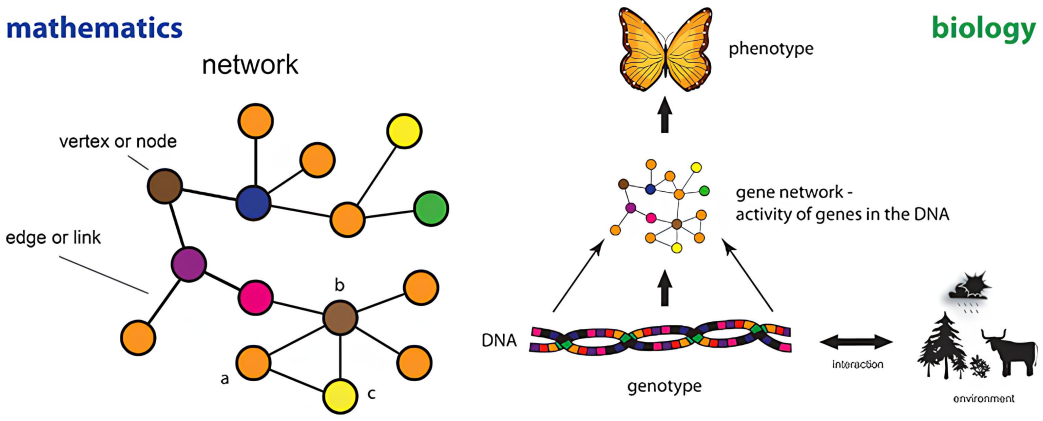

Figure 2.1: Left: Mathematical network and the parts that define it. Right: The principle of the epigenetic landscape showing a gene network as the connection between the genotype of an organism (its DNA) and its phenotype (the way the organism looks). Figure and description taken from [83].

through networks is built upon *graph theory* fundamentals, we introduce some basic concepts.

We can classify any graph by the direction of the connection of its edges. This is, edges can be *directed* or *undirected*. As we can see in Fig. 2.2, a *directed edge* points outward from a starting node towards a destination node; while an *undirected edge* does have nor starting neither destination nodes. In this way, if a graph is constructed only by *directed* edges we talk about a *directed* graph or *digraph*, when this is constructed only by *undirected* links it is called *undirected*. It is also important to mention that in general, graphs can contain loops (an edge that connects a node to itself) and even multiple edges between two nodes (called *multiedges*) as seen in Figs. 2.3(a-b), respectively. This opens a broader categorization of graphs:

- *Simple graphs*: These graphs do not contain multiedges or loops. The edges or links can be undirected (see Fig. 2.2(a)) or directed (see Fig. 2.2(b)). In the directed case multiple arrows with same source and target nodes are not allowed. In this sense Fig. 2.2 is simple, since the bidirectional arrow $\leftrightarrow$ between nodes 3 and 4 denotes an arrow from $3 \rightarrow 4$ and another from $4 \rightarrow 3$.

- *Multigraphs*: They have multiedges but not loops. See multiedges in pairs of nodes (1,2), (1,5), (3,4) from Fig. 2.3(b). By the nature of their edges, they can be undirected multigraphs, or multidigraphs.

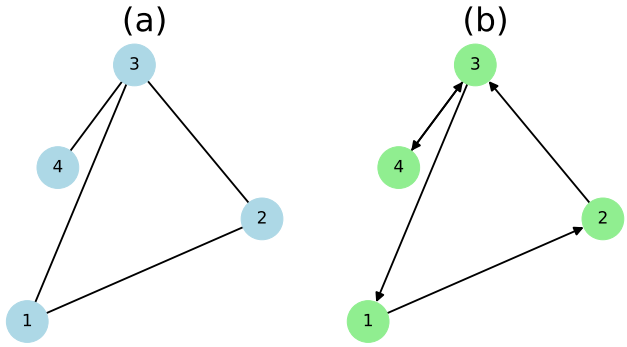

Figure 2.2: Example of (a) an undirected graph and (b) a directed graph with 4 vertices.

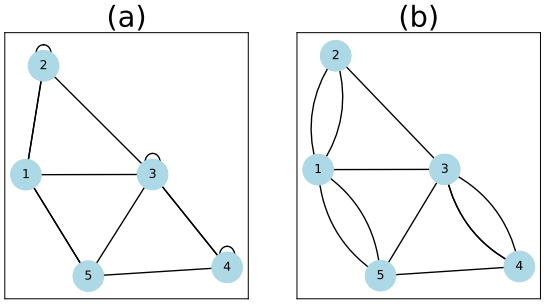

Figure 2.3: (a) Example of a graph of 5 nodes with single edges between nodes and loop edges in nodes 2, 3, and 4. (b) Example of a graph of 5 nodes with multiedges between some pairs of nodes.

- *Pseudographs*: They combine the presence of multiedges and loops. Also edges may have direction or not.

As we observe the broad classification, we focus only on simple undirected and directed graphs since the random network models we analyze in this thesis are simple networks by definition. Then depending on the number of edges a simple graph has, we can identify two extreme stages:

- *Isolated or null graphs*: None of the possible edges exist. See Fig. 2.4(b) where all nodes are isolated because they do not share edges.

- *Complete graphs*: All possible edges exist. See Fig. 2.4(a) for the simple undirected case and Fig. 2.4(c) for the simple digraph case, with bidirectional edges denoting a

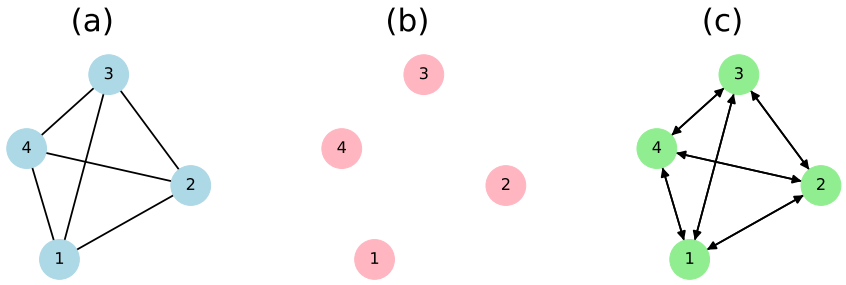

Figure 2.4: Example of a 4 vertex graph as (a) a complete simple undirected graph, (b) an isolated or null graph, and (c) a complete simple directed graph.

single edge per departure node.

Finally, another important possible feature of networks is that their edges may be weighted, and graphs with this characteristic are now called *weighted graphs*. The weights represent some property or characteristic of the relationship between pairs of nodes, thus their meaning varies depending on the context of analysis or applicability. This permits a natural association with complex systems. In Figs. 2.5(a-b) we show a simple weighted graph with the undirected case on the left and the directed one on the right.

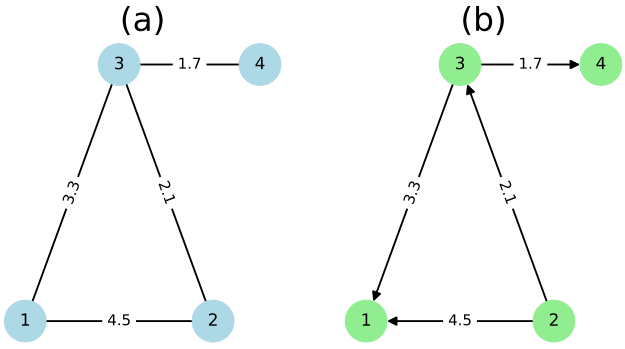

Figure 2.5: Example of (a) a simple undirected weighted graph and (b) a simple directed weighted graph with 4 vertices. Weights are shown on each edge.

2.2 Adjacency matrix

The adjacency matrix **A** is probably the most extensively used matrix representations of networks, **A** is commonly defined as a binary matrix that represents the adjacent connections to every node in the graph,

$$A_{ij} = \begin{cases} 1 & \text{if } i \sim j \\ 0 & \text{otherwise} \end{cases}, \tag{2.1}$$

where $i \sim j$ represents the existence of an edge between nodes i and j. For undirected graphs, we note that the adjacency matrix must be symmetric $A_{ij} = A_{ji}$. Nevertheless, for digraphs, the direction of the edges must be taken into account, therefore we redefine the assignation of one entries as

$$A_{ij} = \begin{cases} 1 & \text{if } j \to i \\ 0 & \text{otherwise} \end{cases}, \tag{2.2}$$

where $j \to i$ indicate the existence of an edge pointing from node j to node i and the resulting adjacency matrix **A** will be, in general, non-symmetric.
Then, the corresponding binary adjacency matrices of the simple undirected and directed graphs of Figs. 2.2(a-b) are

$$A_{(a)} = \begin{pmatrix} 0 & 1 & 1 & 0 \\ 1 & 0 & 1 & 0 \\ 1 & 1 & 0 & 1 \\ 0 & 0 & 1 & 0 \end{pmatrix} \qquad A_{(b)} = \begin{pmatrix} 0 & 0 & 1 & 0 \\ 1 & 0 & 0 & 0 \\ 0 & 1 & 0 & 1 \\ 0 & 0 & 1 & 0 \end{pmatrix}. \tag{2.3}$$

In addition, when having multiedges between nodes, entries become the multiedge cardinality and when having loops, the main diagonal entries corresponding to nodes with loops are replaced by 2. Thus, the adjacency matrix representation of Figs. 2.3(a-b) become

$$A_{(a)} = \begin{pmatrix} 0 & 1 & 1 & 0 & 1 \\ 1 & 2 & 1 & 0 & 0 \\ 1 & 1 & 2 & 1 & 1 \\ 0 & 0 & 1 & 2 & 1 \\ 1 & 0 & 1 & 1 & 0 \end{pmatrix} \qquad A_{(b)} = \begin{pmatrix} 0 & 2 & 1 & 0 & 2 \\ 2 & 0 & 1 & 0 & 0 \\ 1 & 1 & 0 & 2 & 1 \\ 0 & 0 & 2 & 0 & 1 \\ 2 & 0 & 1 & 1 & 0 \end{pmatrix}. \tag{2.4}$$

Moreover, when we treat with weighted graphs and a connection exist, we substitute the one entry for the weight of the edge. Regarding the nature of the links we follow the same previous rules. Then the adjacency matrices of Figs. 2.5(a-b) are given as

$$A_{(a)} = \begin{pmatrix} 0 & 4.5 & 3.3 & 0 \\ 4.5 & 0 & 2.1 & 0 \\ 3.3 & 2.1 & 0 & 1.7 \\ 0 & 0 & 1.7 & 0 \end{pmatrix} \qquad A_{(b)} = \begin{pmatrix} 4.5 & 0 & 3.3 & 0 \\ 0 & 0 & 0 & 0 \\ 0 & 2.1 & 0 & 0 \\ 0 & 0 & 1.7 & 0 \end{pmatrix}. \tag{2.5}$$

2.3 Topology of networks

Within network science, the information that topology provides is crucial for the understanding of complex systems modeled by networks. In this section, we introduce the degree of a node for both simple undirected and directed graphs, the average number of links, the global and local clustering coefficients, and some topological indices such as, the number of non-isolated vertices, the Randić index, and the Harmonic index.

2.3.1 Number of edges, average degree, and connectance

The **degree** is defined as the number of edges or links that connects a vertex to other vertices in the graph. For a node with an assigned tag or label i, we denote the degree as k_i. Since graphs can be *directed* or *undirected*, the degree is classified as follows:

- In-degree: Denoted as k_i^{in}, is the number of edges that point towards node i.
- Out-degree: Denoted as k_i^{out}, is the number of outgoing edges from node i.
- Degree: Denoted as k_i, for *directed* graphs $k_i = k_i^{in} + k_i^{out}$. While for *undirected* graphs $k_i = k_i^{in} = k_i^{out}$ since the in- and out-degrees are the same.

Inasmuch as the adjacency matrix $\mathbf{A}$ from Eqs.(2.1) and (2.2) represents every connection to a node by a unit entry, the degree k_i for a n node graph can be directly computed from $\mathbf{A}$ [12]:

- For in-degree:

$$k_i^{in} = \sum_{j=1}^{n} A_{ij} \tag{2.6}$$

- For out-degree:

$$k_j^{out} = \sum_{i=1}^{n} A_{ij} \tag{2.7}$$

- For the *undirected* case:

$$k_i = k_i^{out} = k_i^{in} \tag{2.8}$$

- For the *directed* case:

$$k_i = k_i^{out} + k_i^{in}. \tag{2.9}$$

Now, the calculation of the **total number of edges**, denoted as L, is straightforward. For *undirected* graphs:

$$2L = \sum_{i=1}^{n} k_i = \sum_{ij} A_{ij}, \tag{2.10}$$

where the factor 2 is given due to double counting of edges in the summation of k_i as incoming and outcoming edges are undistinguishable for the undirected scenario (see Fig. 2.2(a)).

On the other hand, for *directed* graphs:

$$L = \sum_{i=1}^{n} k_i^{in} = \sum_{i=1}^{n} k_i^{out} = \sum_{ij} A_{ij}, \tag{2.11}$$

in this case the factor of 2 does not appear since directed graphs count incoming and outgoing edges separately.

Then, the **average degree**, $\langle k \rangle$, of a graph can be known in terms of L using Eqs. (2.10) and (2.11):

- For the *undirected* case:

$$\langle k \rangle = \frac{1}{n} \sum_{i=1}^{n} k_i = \frac{2L}{n} \tag{2.12}$$

- For the *directed* case:

$$\langle k \rangle = \frac{1}{n} \sum_{i=1}^{n} k_i = \frac{L}{n} \tag{2.13}$$

From Eqs. (2.12) and (2.13) we can see that the average degree $\langle k \rangle$ is a measure of how densely connected a graph may be. Moreover, owing to the lack of multiedges and self-loops of simple graphs, the maximum number of edges will be $L_{max} = \binom{n}{2}$ for undirected and $L_{max} = 2\binom{n}{2}$ for directed graphs. Therefore, we can define the **connectance** [12] of a

graph, known as the fraction of the existent edges in the graph from the possible maximum number of edges:

$$\Omega = \frac{L}{L_{max}} = \frac{\langle k \rangle}{n-1}. \tag{2.14}$$

When the average degree $\langle k \rangle \to 0$, the connectance $\Omega \to 0$ and when $\langle k \rangle \to n-1$ (the maximum average degree of a graph), $\Omega \to 1$. Thus, the connectance Ω ranges between 0 and 1. In particular, as the size n of a network increases $n \to \infty$ and $\Omega \to 0$ we say that the network is *sparse*. The connectance is an indicator of "sparsity" in the graph. In fact, most of the real-world networks are sparse [84] with $\Omega << 1$. Furthermore, the connectance is also the fraction of non-zero off-diagonal elements of the adjacency matrix **A**. Fig. 2.6 exemplifies the non-zero off-diagonal elements of the adjacency matrix **A** for different values of Ω for *directed* and *undirected* graphs with $n = 5$ nodes. We observe that as the connectance Ω increases, the adjacency matrix **A** becomes fuller (disregarding main diagonal elements).

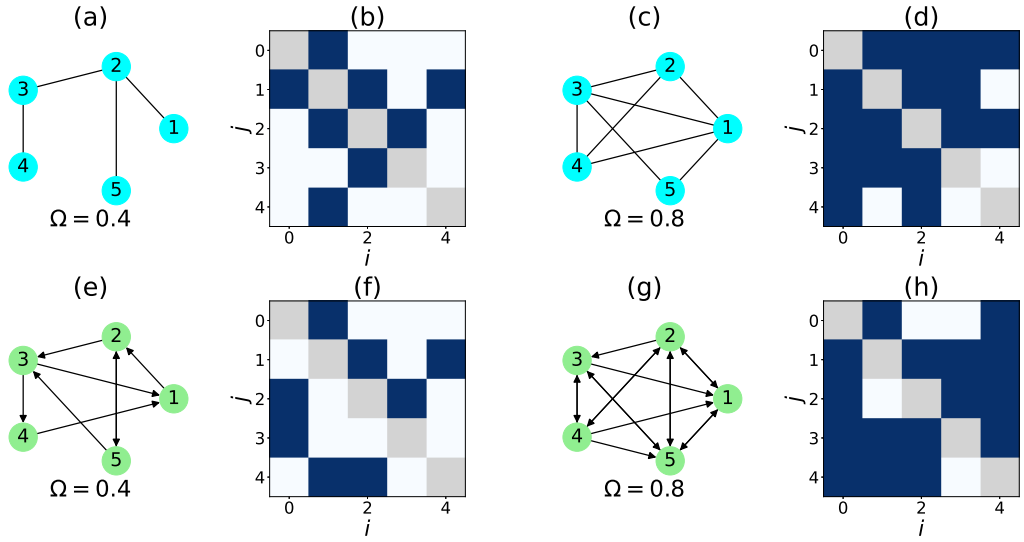

Figure 2.6: (a) Undirected graph with connectance $\Omega = 0.4$ and (b) its corresponding nonzero adjacency matrix elements. (c) Unidirected graph with connectance $\Omega = 0.8$ and (d) its corresponding nonzero adjacency matrix elements. (e) Digraph with connectance $\Omega = 0.4$ and (f) its corresponding nonzero adjacency matrix elements. (g) Digraph with connectance $\Omega = 0.8$ and (g) its corresponding nonzero adjacency matrix elements. Nonzero off-diagonal elements are shown in dark blue. Diagonal elements are colored in light grey only to guide the eye, but they remain zero since graphs are simple.

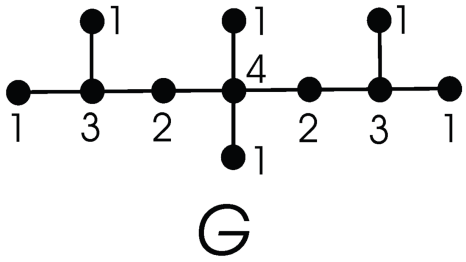

Figure 2.7: Molecular graph G of 2,4,4,6-tetramethylheptane. The degree is indicated next to every vertex. Figure taken from [85].

2.3.2 Degree-based topological indices

Molecular-graph-based structure descriptors also known as *topological indices* have been widely studied in chemistry graph theory as a form to associate a numerical value to a chemical structure [85, 86]. This association is achieved by the extraction of the skeleton of the structure of a molecule, known as a *molecular graph*, that permits quantitative studies to predict biological activity, pattern recognition, toxicity, molar refractions, partition coefficients, boiling points [89–93], and many physicochemical properties of a particular feature of the structure of the compounds being studied [87]. Then, a molecular graph is a simple graph where vertices represent atoms and edges represent the bonds between atoms [85]. Fig. 2.7 exemplifies the graph representation of a branched-chain hydrocarbon with the chemical formula C11H24 with bonds as edges and vertices as atoms.

Topological indices were first introduced by Wiener in his work *"Structural determination of paraffin boiling points"* [88, 99], where he studied physical properties of alkanes in relation to the distances of their molecular graph. After this seminal work was published in 1947, many topological indices were proposed in the context of chemistry and gained attention of mathematicians [94, 95] after the introduction of the first degree-based descriptor proposed by Randić in 1975 in his paper entitled *"On characterization of molecular branching"* [96]. Randić took the bond descriptor (the number of bonds of an atom, equal to its degree) of every atom and proposed an index as the summation of the products of bond descriptor values to the minus one-half power of the pairs of atoms with a sharing bond (see Eq. (2.15)). This index was known as a branching index and proved good correlation with alkane properties such as: boiling points, chromatographic retention times, enthalpies of formation, surface areas, etc. [97, 99]. Thus, among many molecular-graph-

based descriptors, the Randić index is the most explored in chemistry, pharmacology, in mathematics and mathematical chemistry [96, 98]. Interestingly, relationships between the Randić topological index and many other degree-based topological indices have been proved in [96]. Even more, besides the physicochemical applications, this index has been applied to the study of robustness [100], similarity [101], heterogeneity of networks [102], and more recently; applications to the analysis of random networks [103].

Given a simple graph $G = (V(G), E(G))$ with $V(G)$ and $E(G)$ the vertex set and edge set, respectively, the Randić connectivity index is defined as [99]

$$R(G) = \sum_{i \sim j \in E(G)} \frac{1}{\sqrt{k_i k_j}}, \tag{2.15}$$

Another important topological index is the Harmonic index [104]. This index is defined as follows [104]:

$$H(G) = \sum_{i \sim j \in E(G)} \frac{2}{k_i + k_j}. \tag{2.16}$$

Interestingly, this graph invariant has also reported relationships with other indices such as the first geometric-arithmetic index and the sum connectivity index [106,109]. Even Favaron et. al. proposed a relation of the Harmonic index with the eigenvalues of graphs [107]. Some other works, with respect to this index, have analyzed the characterization of extremal graphs that maximize or minimize this topological graph invariant under given constraints, while others have analyzed its minimum and maximum values for unicyclic, simple, bicyclic graphs, and trees [109–111, 115–117].

Other studies refer to this index as having a better correlation with some physicochemical properties than the Randić index. On that account, this index has been used to push forward studies of nanostructures. For example, a fifth harmonic index was introduced in [105] to contribute to the study of H-Naphtalenic and TUC4[m,n] nanotubes, an explicit formula of the Harmonic index for nanocones CNC_k[n] was explored in [108], also inspired on the degree-based index, a Harmonic index of temperature was suggested in [112]. Even the generalized version of the Harmonic index presented in [113] has been focus of studies of graphene [114].

Finally, another measure we use in this dissertation is the *number of non-isolated vertices*, denoted as V_x. Since a topological index is defined as the summation of a function of the degrees of vertices with a common edge [85], the *number of non-isolated vertices* V_x is also a topological index, defined as:

$$V_x = \sum_{i \sim j} \left(\frac{1}{k_i} + \frac{1}{k_j} \right) \tag{2.17}$$

In particular, this index has been correlated to other topological and spectral properties in the study of random networks (see, for instance, [118]).

Here, $i \sim j$ denotes the edge connecting vertices i and j, and k_i the degree of vertex i. Note that edge nature (directed or undirected) is considered in the definition of the degree k_i from Eqs. (2.8) and (2.9).

2.3.3 Local and global clustering coefficients

Specially proposed for the analysis of social networks to reveal a collaborative relationship between agents [119, 120], the *local clustering coefficient* also known as *Watts-Strogatz (WS) clustering coefficient* [16] is a measure of the tendency of nodes to cluster (or form complete subgraphs) as edges between neighbors to a node form. Then, the local clustering coefficient of a node i is the likelihood that its neighbor nodes connect to each other. It is defined as the ratio of the number of edges E_i that exist between neighbors of node i to the total number of possible edges between them $\binom{k_i}{2}$ [16],

$$C_i = \begin{cases} 0, & \text{if } \; k_i = 0, 1 \\ \frac{2E_i}{k_i(k_i-1)}, & \text{if } \; k_i \geq 2 \end{cases} . \tag{2.18}$$

Also in terms of the binary adjacency matrix $\mathbf{A}$, the WS clustering coefficient given by Eq. (2.18) when $k_i \geq 2$ takes the form [121]

$$C_i = \frac{1}{k_i(k_i - 1)} \sum_{j,k} A_{ij} A_{jk} A_{ki}. \tag{2.19}$$

Figs. 2.8(a-c) show an example of the clustering coefficient of a node 1 (red node) at different stages of connection for a graph with 4 vertices. As exemplified in the Fig. 2.8, and according

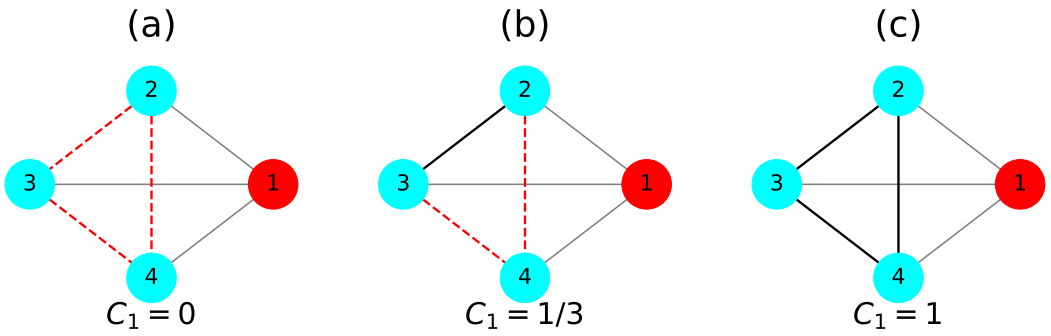

Figure 2.8: Example of the measurement of the local clustering coefficient of a simple undirected graph with 4 vertices. Gray solid lines show the edges connecting to node 1, red dashed lines show the possible and non-existent edges between neighbors (nodes connected to node 1), an actual edge between neighbors is denoted by a black solid line. (a) None of the edges between neighbors exist and $C_1 = 0$. (b) An edge exists between nodes 2 and 3, one out of three, thus $C_1 = 1/3$. (c) All edges exist and a comple graph forms $C_1 = 1$.

to definition of Eq. (2.18), C_i transits from 0 to 1 as local subgraphs of a node form. This quantity is equally described as the ratio of the number of triangles (three nodes forming a closed graph, see, for instance, Fig. 2.8(c)) to the total number of possible triangles that share a node i.

A straightforward way to measure the overall level of local clustering of any network is by using the *average local clustering coefficient* of a graph G, defined as

$$\overline{C}(G) = \frac{1}{n}\sum_{i}^{n} C_i = \sum_{i}^{n} \frac{2t_i}{k_i(k_i - 1)}, \tag{2.20}$$

where $t_i = E_i$ is the number of triangles of i and n is the number of vertices of the graph. One important trait of this quantity is that networks which have a high average clustering coefficient are considered to be of the *small world* type [16].

A different way to measure clustering in a network is through the use of the *global clustering coefficient or transitivity* [122, 123]. In contrast to the WS coefficient, the transitivity gives the tendency of the whole network to form clusters and focuses on the formation of triplets to quantify it. See Fig. 2.9. It is defined as the ratio of the number of closed triplets (triangles) to the the total number of triplets (open and closed) of the graph [122, 123],

$$C_g(G) = \frac{\text{number of closed triplets}}{\text{total number of triplets}} = \frac{\sum_i^n t_i}{\sum_i^n k_i(k_i - 1)}. \tag{2.21}$$

That in terms of the binary adjacency matrix $\mathbf{A}$, becomes:

$$C_g(G) = 2\frac{\sum_{i,j,k} A_{ij}A_{jk}A_{ki}}{\sum_i^n k_i(k_i-1)}. \tag{2.22}$$

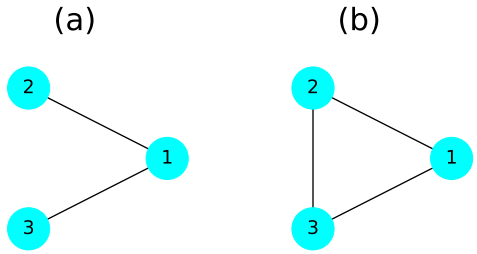

Figure 2.9: Example of (a) an open triplet and (b) a closed triplet or triangle graph.

Chapter 3

Spectral measures in random matrix theory

For the study of a single random network cannot shed light on global network properties, as stated earlier, we use random matrix theory (RMT) as a mainly numerical approach to derive global properties of random network ensembles. Thus, in this chapter we define the RMT adjacency matrices and common RMT spectral static measures that we use for the study of random network models in the next chapters.

3.1 RMT adjacency matrix

The connection between RMT and random networks seems straightforward through the use of weighted graphs. As discussed in Chapter 2, the edges may contain weights which can be represented in every entry of the adjacency matrix (See Eq. (2.5) and its corresponding graphs in Fig. 2.5). Then an ensemble of adjacency matrices from graphs with random weights will become RMT ensemble-like. In addition, for any ensemble of random simple graphs (directed or undirected), when the connectance becomes $\Omega = 1$ the off-diagonal adjacency matrix elements are different from zero (they are 1, indeed in the binary adjacency matrix representation); however, the main diagonal remains empty. In this sense, for many random network models, generally simple, it is impossible to recover any of the classical RMT ensembles (GOE, GSE, or GSE), which are full random matrices, by using typical adjacency matrix representations. This puts forward the need to introduce a different adjacency matrix representation capable to convey the structural information of

random networks, possible edge weights (or interaction strength between nodes) that resemble complex systems modeled by networks, and at the same time makes use of RMT ensembles as top and bottom limit references when the connectance transits from $\Omega = 1$ to $\Omega = 0$.

In this sense, we define the RMT reference ensembles that we use throughout this thesis work for the analysis of random network models according to their constructions, directed or undirected edge assignation.

3.1.1 Gaussian Orthogonal ensemble

The gaussian orthogonal ensemble (GOE), known as one of the classical Wigner-Dyson random matrix ensembles, was firstly introduced for the analysis on the eigenvalue distribution of heavy nuclei with level repulsion [49]. Since the GOE is invariant under orthogonal transformations, it has been used to study systems invariant under time-reversal and rotational symmetry. Some applications of the GOE extend from quantum systems with a chaotic classical limit, where the energy spectrum follows the GOE [125], to condensed matter physics, describing disordered metals and transport properties [126]. Interestingly, regarding applications to graph theory, it has been showed that the adjacency matrix spectrum of certain random graphs (undirected) follows GOE statistics [124]. In fact, since the adjacency matrix of undirected random networks are real and symmetric, as shown in Fig. 2.2(a) and Eq. (2.1) in Chapter 2, the connection to random orthogonal symmetric matrices of the GOE is straightforward. A clear example of this connection is reported in the analysis of the distribution of level spacings for random networks matching the GOE prediction even when the connectance $\Omega << 1$ [58]. Therefore, we can use the GOE matrix representation as a convenient top limit ensemble of undirected random networks through weighted adjacency matrices. This approach has been applied to characterize spectral properties of random networks in [30, 58, 118, 149, 158]. Accordingly, we define the randomly-weighted version of the adjacency matrix for undirected networks as:

$$[\mathbf{A}_O]_{uv} = \begin{cases} \sqrt{2}\epsilon_{uv} & u = v, \\ \epsilon_{uv} & u \sim v, \\ 0 & \text{otherwise}, \end{cases} \tag{3.1}$$

where ϵ_{uv} are independent random variables drawn from a normal distribution with zero mean and unit variance, and $u \sim v$ depicts the undirected edge between nodes u and v. With this definition, diagonal random matrices (known in RMT as the Poisson Ensemble (PE) [125]) are obtained when the graphs consist of disconnected vertices ($\Omega = 0$); whereas the GOE (i.e. full real and symmetric random matrices [125]) is recovered when the graphs are complete ($\Omega = 1$). This means that as a graph becomes more densely connected we expect to observe a transition from the PE to the GOE as Ω increases. Thus, the ensemble defined by the randomly-weighted adjacency matrices $\mathbf{A_O}$ corresponds, indeed, to a diluted GOE during the crossover from disconnected (also known as isolated) to complete graphs.

3.1.2 Real Ginibre ensemble

After the formulation of the Wigner-Dyson classical ensembles (GOE, GUE, GSE), Ginibre formulated, as a mathematical extension to RMT, non-Hermitian random matrix ensembles to account for relevant physical systems where the governing operators or matrices are non-Hermitian [127]. In particular, the real formulation of the Ginibre ensembles, called real Ginibre ensemble (RGE), have proved useful in the analysis of open quantum dissipative systems, and the stability of large random neural networks and biological networks [128, 129, 150]. Since adjacency matrices extracted from directed networks are non-Hermitian (see Eq. (2.2) and (2.5)(b)), some studies have focused on the spectral analysis of directed complex networks in relation to the Ginibre ensemble and have shown that short-range and long-range eigenvalue correlations agree well with Ginibre ensemble predictions [131]. For this straightforward connection, the analysis of directed random networks through a randomly-weighted non-Hermitian adjacency matrix has been considered in [149]. In this work, we use this non-Hermitian adjacency matrix $\mathbf{A_{nH}}$ for directed graphs defined as follows:

$$[A_{nH}]_{uv} = \begin{cases} \epsilon_{uu} & u = v, \\ \epsilon_{uv} & u \to v, \\ 0 & \text{otherwise}, \end{cases} \tag{3.2}$$

where ϵ_{uv} are independent random variables drawn from a normal distribution with zero mean and unit variance, and $u \to v$ denotes the edge oriented from node u towards v; note that in general $\epsilon_{uv} \neq \epsilon_{vu}$ when a graph G is directed. Thus, when we analyze spectral properties of a large ensemble of random graphs represented by this definition, diagonal random matrices (Poisson ensemble) are obtained when the graphs consist mostly of disconnected

vertices; whereas the Real Ginibre Ensemble (RGE) (i.e. full real and non-symmetric random matrices [127]) is recovered when the graphs are complete. Therefore, in the statistical analysis of a random graph, we expect to observe, for any spectral quantity, a transition from the PE to the RGE for increasing connectance Ω or average degree $\langle k \rangle$. Thus, the ensemble defined by $\mathbf{A_{nH}}$ corresponds to a diluted RGE [149].

3.1.3 Magnetic random matrix ensemble

In 1993, Lieb and Loss introduced a Laplacian operator associated to a graph as a discretization of space for the analysis of a quantum particle as an attempt to study electron magnetic field interactions in condensed matter physics. This operator, called the magnetic Laplacian operator, has been used as a tool for the study of the stability of an eigenvalue of a graph under a magnetic perturbation and correlation to the number of zeros of its corresponding eigenfunction [133], among other applications; such as community detection and signal processing algorithm development for directed graphs [134, 135]. Furthermore, the characterization of directed networks has been analyzed thorough the spectra of the magnetic Laplacian operator [138]. Indeed, the first appearance of a weighted adjacency matrix inspired on the magnetic Laplacian operator applied to the study of random networks was introduced in [149], although Hermitian adjacency operators (also inspired on the magnetic Laplacian framework) for unweighted directed networks were already defined in [136,137]. In this sense, we consider the randomly-weighted Hermitian adjacency matrix formulation for directed random graphs proposed in [149] as the building block for what we call the *magnetic random matrix ensemble* (MRME).

Given the standard binary adjacency matrix $\mathbf{A}$ of Eq. (2.2) extracted from a directed graph, we consider the following Hermitian adjacency matrix $\mathbf{A_H}$:

$$[A_H]_{uv} = \begin{cases} \sqrt{2}\epsilon_{uu} & u = v, \\ \epsilon_{uv} A_{uv} & u \leftrightarrow v, \\ i\epsilon_{uv} A_{vu} & u \to v, \\ -i\epsilon_{uv} A_{vu} & v \to u, \\ 0 & \text{otherwise.} \end{cases} \tag{3.3}$$

Again, ϵ_{uv} are independent random variables taken from a normal distribution with zero mean and variance one [149], $u \to v$ [$v \to u$] depicts the edge orientation from u [v] towards v [u], and $u \leftrightarrow v$ denotes the existence of the two edges $u \to v$ and $v \to u$. It is clear

that $[A_H]_{vu} = [A_H]^*_{uv}$ by construction. The main advantage of $\mathbf{A_H}$ over $\mathbf{A_{nH}}$ is that the former has a real spectrum, thus some spectral measures from RMT can be computed easier [30, 149]. Therefore, when considering an ensemble of random directed networks, the MRME defined by $\mathbf{A_H}$ transits from the PE, when graphs consist mostly of disconnected vertices, to the Gaussian Orthogonal Ensemble (GOE) (i.e. full real and symmetric random matrices [125]), when graphs are complete. This convergence to the GOE is clearly seen from Eq. (3.3), as any pair of vertices is connected by two edges (each with a different orientation) when $\Omega = 1$, giving as a result Eq. (3.1). Here it is important to note that the MRME can not be considered as a diluted GOE since for any connectance $\Omega < 1$ ($\langle k \rangle < n - 1$), $\mathbf{A_H}$ is still a complex Hermitian matrix.

3.2 Spectral measures

As previously stated, we are interested in the statistical analysis of ensembles of random matrices characterized by randomly-weighted adjacency matrices to understand global network properties. Hence, we perform numerical diagonalization of orthogonal $\mathbf{A_O}$, non-Hermitian $\mathbf{A_{nH}}$ and Hermitian $\mathbf{A_H}$ weighted adjacency matrices defined, respectively, in Eqs. (3.1), (3.2) and (3.3) to obtain the eigenvalues λ_i and normalized eigenvectors Ψ^i of directed and undirected random network models. Thus, in this work we do not consider the binary adjacency matrix $\mathbf{A}$ for the analysis of spectral and eigenvector properties, only the weighted versions defined above. Consequently, in this numerical approach, we use standard RMT measures to characterize spectral and eigenvector properties.

It is important to clarify that, in this work, the term *spectral measure* is not used in the formal sense of functional analysis, where it refers to a projection-valued measure associated with a self-adjoint operator, as defined by the spectral theorem [139]. Nor is it related to the concept of measure in the Lebesgue sense, which assigns sizes to subsets of the real line and is used, for example, to describe spectral densities [139]. Instead, we use *spectral measure* or *spectral property* in an informal, statistical sense common in RMT to refer to functions of eigenvalues such as the ratio between consecutive eigenvalue spacings, which are analyzed across ensembles of random matrices to capture features of spectral statistics.

Then, regarding eigenvalue properties, in this work, we compute the ratio between

consecutive level spacings $r_{\mathbb{R}}$ and the ratio between nearest- and next-to-nearest eigenvalue spacings $r_{\mathbb{C}}$. The former quantity is suitable for the analysis of real and ordered spectrum $\lambda_1 > \lambda_2 > \cdots > \lambda_{n-1} > \lambda_n$, where the i–th ratio is given by [140, 141]

$$r^i_{\mathbb{R}} = \frac{\min(\lambda_{i+1} - \lambda_i, \lambda_i - \lambda_{i-1})}{\max(\lambda_{i+1} - \lambda_i, \lambda_i - \lambda_{i-1})}. \tag{3.4}$$

When the spectrum is complex, such as in the case of $\mathbf{A_{nH}}$, we use the ratio between nearest- and next-to-nearest-neighbor spacings $r_{\mathbb{C}}$, with the i–th ratio defined as [142]

$$r^i_{\mathbb{C}} = \frac{|\lambda_i^{\mathrm{NN}} - \lambda_i|}{|\lambda_i^{\mathrm{NNN}} - \lambda_i|}; \tag{3.5}$$

where λ_i^{NN} and λ_i^{NNN} are, respectively, the nearest and the next-to-nearest neighbors of λ_i in $\mathbb{C}$. However, $r_{\mathbb{C}}$ can also be computed for real spectra, so it works for both $\mathbf{A_{nH}}$ and $\mathbf{A_H}$. These two eigenvalue quantities provides valuable information on the local spectral rigidity as well as being considered measures of complexity that indicate the localization-to-delocalization transition of directed random networks represented by random adjacency matrices. Particularly, in this work, we focus on the average of these quantities over an ensemble of random graph models $\langle r_{\mathbb{R}} \rangle$ and $\langle r_{\mathbb{C}} \rangle$.

Regarding eigenvector properties, given the normalized eigenvectors Ψ^i (that is, $\sum_{m=1}^n |\Psi^i_m|^2 = 1$) of $\mathbf{A_{nH}}$ or $\mathbf{A_H}$, we compute the inverse participation ratios [140]

$$\mathrm{IPR}_i = \left[\sum_{m=1}^{n} |\Psi^i_m|^4 \right]^{-1} \tag{3.6}$$

and the Shannon entropies [143, 144]

$$S_i = \sum_{m=1}^{n} |\Psi^i_m|^2 \ln |\Psi^i_m|^2. \tag{3.7}$$

Both IPR and S measure the extension of eigenvectors on a given basis. In the case of random graphs, IPR is commonly used to characterize the localization properties of a network (see e.g. [145–147]) while S has been used to prove percolation transitions (see e.g. [30, 58, 149]). As IPR and S give the number of main components of an eigenvector, and we want to globally characterize random network models, we focus on the average of these quantities over all eigenvectors of ensembles of randomly weighted adjacency matrices; $\langle \mathrm{IPR} \rangle$ and $\langle S \rangle$.

From definitions (3.4-3.7), when $\Omega \approx 0$; that is when $\mathbf{A_O}$, $\mathbf{A_{nH}}$ and $\mathbf{A_H}$ are mostly diagonal, $r_{\mathbb{C}}(G) \approx (r_{\mathbb{C}})_{\mathrm{PE}}$, $r_{\mathbb{R}}(G) \approx (r_{\mathbb{R}})_{\mathrm{PE}}$, $\mathrm{IPR}(G) \approx (\mathrm{IPR})_{\mathrm{PE}}$, and $S(G) \approx (S)_{\mathrm{PE}}$; while

for $\Omega = 1$, when $\mathbf{A_O}$, $\mathbf{A_{nH}}$ and $\mathbf{A_H}$ are full random matrices, all spectral and eigenvector measures are expected to acquire their corresponding full random matrix values [30,149] for they permit us to characterize the transition from isolated to complete graphs in relation to RMT ensemble limits. Thus, these eigenvector measures are relevant to our study. Therefore, since we are interested on the characterization of these quantities for random network models with varying number of vertices (network sizes), we conveniently normalize them to ease the comparison

$$\langle \overline{r}_{\mathbb{R}}(G)\rangle \equiv \frac{\langle r_{\mathbb{R}}(G)\rangle - (r_{\mathbb{R}})_{\mathrm{PE}}}{(r_{\mathbb{R}})_{\mathrm{RME}} - (r_{\mathbb{R}})_{\mathrm{PE}}}, \tag{3.8}$$

$$\langle \overline{r}_{\mathbb{C}}(G)\rangle \equiv \frac{\langle r_{\mathbb{C}}(G)\rangle - (r_{\mathbb{C}})_{\mathrm{PE}}}{(r_{\mathbb{C}})_{\mathrm{RME}} - (r_{\mathbb{C}})_{\mathrm{PE}}}, \tag{3.9}$$

$$\langle \overline{\mathrm{IPR}}(G)\rangle \equiv \frac{\langle \mathrm{IPR}(G)\rangle - \mathrm{IPR}_{\mathrm{PE}}}{\mathrm{IPR}_{\mathrm{RME}} - \mathrm{IPR}_{\mathrm{PE}}}, \tag{3.10}$$

and

$$\langle \overline{S}(G)\rangle \equiv \frac{\langle S(G)\rangle}{S_{\mathrm{RME}}}; \tag{3.11}$$

where the subscript RME stands for random matrix ensemble, denoting the value of the quantity for the random matrix ensemble under study. In addition, G denotes the graph, so $\langle X(G)\rangle$ denotes the average over the ensemble of graphs, here $X(G)$ stands for any eigenvalue and eigenvector measure previously defined.

	PE	GOE	RGE	MRME ($\Omega \to 1$)
$(r_{\mathbb{R}})_{\mathrm{RME}}$	0.3867 [149]	0.5307 [141, 149]	–	0.5995 [149]
$(r_{\mathbb{C}})_{\mathrm{RME}}$	0.5006 [149]	0.5688 [118, 149]	0.737 [149]	0.6175 [149]
$(\mathrm{IPR})_{\mathrm{RME}}$	1	$n/3$ [118]	$n/2.04^{**}$	$n/2$ [148]
$(S)_{\mathrm{RME}}$	0	$\ln(n/2.07)$ [149]	$\ln(n/1.56)$ [149]	$\ln(n/1.53)$ [143]

Table 3.1: Values of the eigenvalue and eigenvector measures of Eqs. (3.8)-(3.11) for the limit random matrix ensembles PE, GOE, RGE, and MRME. The references where these quantities are reported appear in every cell. The asterisks indicate a value computed numerically in this work.

Thus, in Table 3.1, we show the limiting values of spectral and eigenvector measures for every random matrix ensemble. One important fact about the MRME is that the values of the measures as $\Omega \to 1$ (when the random matrix is Hemitian complex) tend to the GUE predictions. Indeed, the transition from GUE to GOE has been reported in the literature for this RME. Thus, the values reported for MRME when $\Omega \to 1$ correspond to the GUE

predictions. Finally, we note that since we did not find an expression for $(\text{IPR})_{\text{RME}}$ for the RGE in the literature, we computed it numerically for the graph sizes used in this work [30]; see Chapter 4.

Hence, with these quantities properly defined, we establish the framework for our study of random networks in the following chapters. Specifically, we analyze topological properties using binary adjacency matrices and static spectral properties using randomly weighted adjacency matrices, respectively, through the use of large random matrix ensembles.

Chapter 4

Directed random geometric graphs

In this chapter we present a model of directed random geometric graphs that we define in Section 4.1. We perform a thorough numerical analysis of the model for the whole transition, from isolated to full graphs, and show that through the use of the average degree $\langle k \rangle$ we can find a scaling parameter for the structural and spectral properties. In particular, we utilize two random matrix theory ensembles as reference for the analysis of spectral measures, the RGE and the MRME. This chapter is based on the work published in [30].

4.1 Random graph model

In Gilbert's original version a random geometric graph (RGG) consists of n vertices uniformly and independently (randomly) distributed on the plane, where two vertices u and v are connected by an undirected edge if their Euclidean distance is less or equal than a connection radius ℓ [24]. Although there are many space embedding configurations for RGGs, one of the most simple representations is the unit square with rigid walls, where n vertices are uniformly and independently (randomly) distributed in it. In Fig. 4.1 we show a RGG in the unit square with $n = 45$ vertices and a radius of connection $\ell = 0.2$. Each highlighted red node is surrounded by a red dashed circle that depicts its connection disk of radius ℓ; vertices lying inside the disk are linked to the central vertex exemplifying the construction of the entire undirected graph.

Interestingly, even when most of the real-world spatial networks that could be modeled by random geometric graphs (RGGs) (i.e. transportation networks like cargo ship networks,

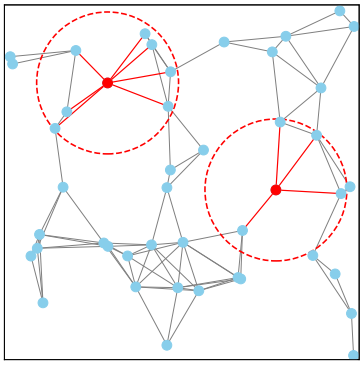

Figure 4.1: RGG in the unit square with $n = 45$ vertices and radius of connection $\ell = 0.2$. Two vertices, their corresponding connection disks (circles), and their corresponding links are showed in red.

infrastructure networks like power networks or road networks, communication networks, etc.) and the processes associated to them (i.e. disease spreading, urban sprawl, commuter behavior, etc.) are intrinsically directed, models of directed RGGs have been scarcely studied. There are some exceptions where models of directed RGGs have been used to study wireless networks and word association networks, respectively [8, 9].

Therefore, as an extension of the RGG defined above, in this work, we consider a directed RGG (dRGG) with n vertices uniformly and independently (randomly) distributed in the unit square with randomly assigned connection radius ℓ_u to the vertex u, where ℓ_u is taken from a Pareto distribution,

$$f(\ell) = \begin{cases} \eta/\ell^{\alpha} & \ell_0 \leq \ell \leq \sqrt{2}, \\ 0 & \text{otherwise.} \end{cases} \tag{4.1}$$

Here, $\alpha > 0$ is the exponent of the power-law decay of the Pareto distribution, $\ell_0 \in (0, \sqrt{2}]$ is the lowest bound of the support of the distribution, and

$$\eta = \begin{cases} (\alpha - 1)\ell_0^{\alpha-1}[1 - (\ell_0/\sqrt{2})^{\alpha-1}]^{-1} & \alpha \neq 1, \\ [\ln(\sqrt{2}/l_0)]^{-1} & \alpha = 1, \end{cases} \tag{4.2}$$

is a normalization factor such that $\int_{\ell_0}^{\sqrt{2}} f(\ell)d\ell = 1$. With this assignation, every vertex of the graph may have a different radius of connection; in Fig. 4.2 we show some examples of

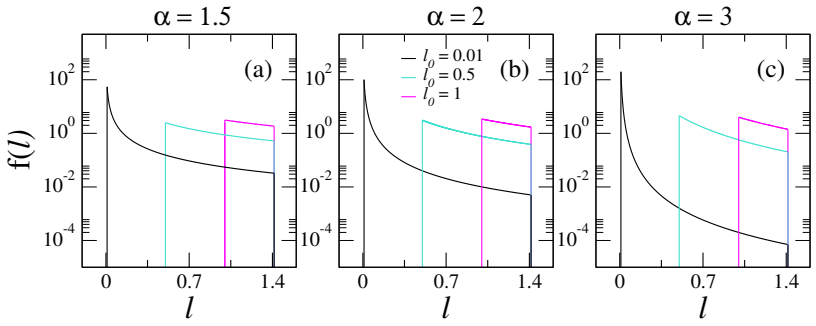

Figure 4.2: Probability distribution functions $f(\ell)$, see Eq. (4.1), for (a) $\alpha = 1.5$, (b) $\alpha = 2$, and (c) $\alpha = 3$. Each panel displays $f(\ell)$ with $\ell_0 = 0.01$, 0.5, and 1. Figure taken from [30].

probability distribution functions $f(\ell)$ for different combinations of α and ℓ_0. Then, if the vertex v lies within the disk of radius ℓ_u, centered at u, there exists a directed edge from u to v, $u \to v$. Note that since $\ell_u \neq \ell_v$, the existence of $u \to v$ does not imply $u \leftarrow v$, so the graph is directed. In Fig. 4.3 we show an example of a dRGG with $n = 45$ vertices. Three nodes are highlighted in different colors with their corresponding connection disks, contrasting with Fig. 4.1 since every vertex has a different radius of connection, ensuring that the formation of directed edges is independent of the existence of others between pairs of nodes. The directed links emanating from the highlighted nodes (source nodes) are shown in the same color.

Thus, this model of dRGGs depends on three parameters: $G(n, \alpha, \ell_0)$. Here, the low bound of the support of the Pareto distribution ℓ_0 is considered as a free parameter in the range $(0, \sqrt{2}]$, then this graph shows a transition by increasing ℓ_0, for fixed parameters (n, α), from isolated vertices when $\ell_0 \approx 0$ to complete graphs for $\ell_0 = \sqrt{2}$. On the other hand, as $\alpha > 0$ when $\alpha \to 0$ we note that the distribution $f(\ell)$ becomes flat and as $\alpha \to \infty$ we can also enhance the existence of isolated vertices as seen in Fig. 4.2(c) for $\ell_0 = 0.01$. Therefore, the transition from isolated (disconnected) to fully connected graphs depends on the proper election of both parameters (α, ℓ_0).

4.2 Structural properties

First, we study the statistical properties of the vertex degree k of the dRGGs, which is defined according to Eq. (2.9). Thus, in Fig. 4.4 we present examples of the degree distribution $P(k)$ for different graph sizes n (different columns correspond to different values

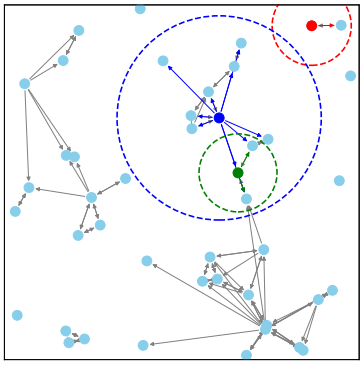

Figure 4.3: dRGG in the unit square with $n = 45$ vertices and lower bound radius $\ell_0 = 0.1$ and exponent $\alpha = 4$. Three vertices are highlighted in colors (red, blue, and green; from top to bottom) and their corresponding connection disks are depicted as dashed circles in the same color.

of n) and two values of the exponent of the Pareto distribution α: $\alpha = 1.5$, panels (a-d), and $\alpha = 7$, panels (i-l). We note that, for fixed α, the support of $P(k)$ grows with n while keeping the same shape; indeed the shape of $P(k)$ evolves with α. Specifically, while for small values of α, $P(k)$ develops a two-peak structure (one broad peak for $k \to 1$ and one sharp peak at $k = n - 1$, see e.g. Figs. 4.4(a-d) for $\alpha = 1.5$), $P(k)$ is unimodal for large α (see e.g. panels (i-l) for $\alpha = 7$). Moreover, we observe a smooth transition in the shape of $P(k)$ from the two-peak structure to the unimodal form for increasing α; see for example Figs. 4.5(a-e), where we show $P(k)$ for several values of α. The existence of the second peak at large k is understood from the Pareto distribution of Eq. (4.1), for small α we expect a still significant proportion of radii $\ell \to \sqrt{2}$ and since the degree k is given as the summation of *in-* and *out-* degrees (see Eq. (2.9)), we observe a significant contribution for large k. Thus, as observed in Figs. 4.5(a-e), this second peak is lessened as α increases. Notice, though, that in Figs. 4.5(a-e) we are plotting distributions of the normalized degree $\overline{k} = (k - \langle k \rangle)/\sigma(k)$, where $\sigma^2(k)$ is the variance of k, to show that the shape of $P(\overline{k})$ depends on α only.

As stated in Chapter 2, the average degree $\langle k \rangle$ indicates the level of sparsity of the graph, therefore, we characterize the average degree of dRGGs. Then, also in Fig. 4.4 we show the average degree $\langle k \rangle$ as a function of ℓ_0 for dRGGs characterized by $\alpha = 1.5$, panels

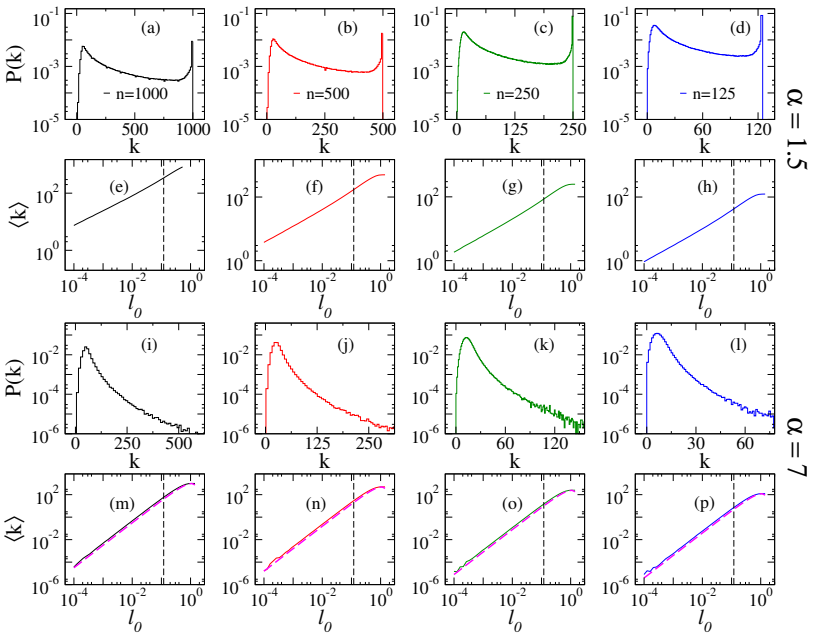

Figure 4.4: (a-d,i-l) Degree distributions $P(k)$, at $\ell_0 = 0.12$, and (e-h,m-p) average degree $\langle k \rangle$ as a function of ℓ_0 for dRGGs. Each column corresponds to random graphs of different size n. Panels (a-h) and (i-p) correspond to $\alpha = 1.5$ and $\alpha = 7$, respectively. Vertical black-dashed lines in (e-h,m-p) mark $\ell_0 = 0.12$, the value of ℓ_0 used to compute $P(k)$ in (a-d,i-l). Magenta dashed lines in (m-p) are Eq. (4.3). Both $P(k)$ and $\langle k \rangle$ were computed from $10^6/n$ random graphs. Figure taken from [30].

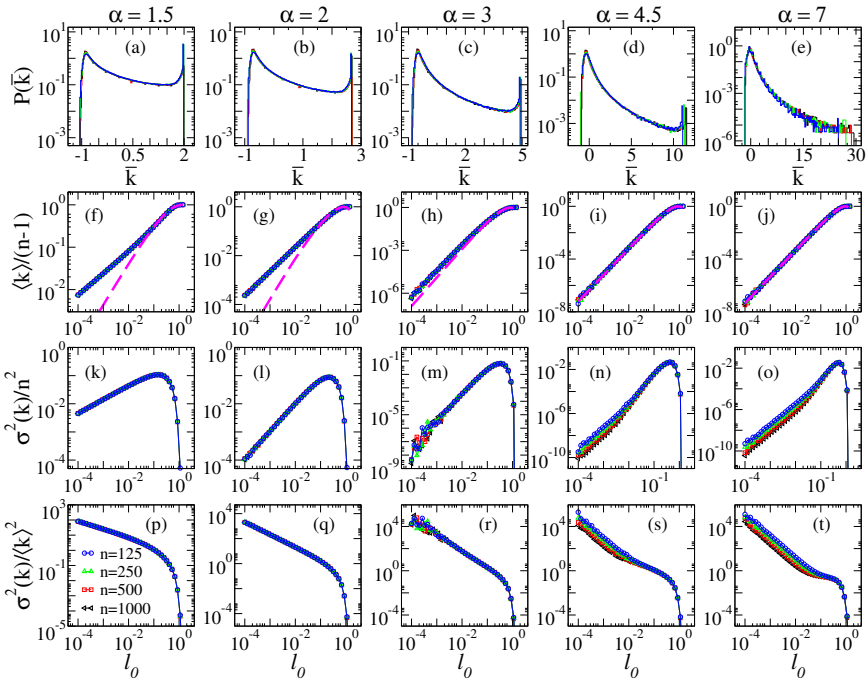

Figure 4.5: (a-c) Probability distribution function of the normalized degree $P(\overline{k})$ for dRGGs with $\ell_0 = 0.12$. (f-j) Average degree $\langle k \rangle$ (normalized to $n-1$) as a function of ℓ_0. Magenta dashed lines in (f-j) are the best fittings of Eq. (4.4) to the data; the fitting constants are reported in Table 4.1. (k-o) The variance of the degree $\sigma^2(k)$ (normalized to n^2) and (p-t) the ratio $\sigma^2(k)/\langle k \rangle^2$ as a function of ℓ_0. In all panels we report results for four different graph sizes n. Each column corresponds to a different value of the power-law decay α. Figure taken from [30].

(e-h), and $\alpha = 7$, panels (m-p). In particular, we notice that the curves $\langle k \rangle$ vs. ℓ_0 for $\alpha = 7$ can be well described by the expression for $\langle k(n, \ell) \rangle$, derived in [151], for standard RGGs when replacing ℓ by ℓ_0:

$$\langle k \rangle = (n-1)\ell_0^2 \left(\pi - \frac{8}{3}\ell_0 + \frac{1}{2}\ell_0^2 \right); \tag{4.3}$$

see the magenta dashed lines in Figs. 4.4(m-p). This fact makes sense because for large α, the Pareto distribution $f(\ell)$ is strongly peaked at ℓ_0 so most radii get the value of ℓ_0; see Fig. 4.2(c). Moreover, taking into account that we are dealing with a distribution of radii ℓ, we found that

$$\langle k \rangle = (n-1)\langle \ell \rangle^2 \left(C_1 - C_2\langle \ell \rangle + C_3\langle \ell \rangle^2 \right) \tag{4.4}$$

describes the average degree of dRGGs with $\alpha > 3$ even better than Eq. (4.3). In this case, C_i are fitting constants and $\langle \ell \rangle$ is the average connection radius that we computed directly

from Eq. (4.1) as

$$\langle \ell \rangle = \begin{cases} \eta \left[2^{(2-\alpha)/2} - {\ell_0}^{2-\alpha} \right] [2-\alpha]^{-1} & \alpha \neq 1, 2, \\ \eta \left[2^{(2-\alpha)/2} - {\ell_0}^{2-\alpha} \right] & \alpha = 1, \\ \eta \ln(\sqrt{2}/\ell_0) & \alpha = 2, \end{cases} \tag{4.5}$$

where η is given in Eq. (4.2). An important consequence of Eq. (4.4) is that the ratio $\langle k \rangle/(n-1)$ does not depend on n, as it is verified in Figs. 4.5(f-j) for all values of α (not only for $\alpha > 3$): There, in each panel, we present four curves for different graph sizes n that fall one on top of the other, as anticipated. Thus, in Figs. 4.5(f-j) we plot Eq. (4.4) (as magenta dashed lines) and see a very good correspondence with the numerical data for $\alpha > 3$, while for smaller α we see good correspondence for large ℓ_0 only. Notice from Table 4.1 that the value of the fitting constant C_1 is approximately equal to π for all α; therefore, the prediction for $\langle k(n, \ell) \rangle$ for standard RGGs from [151] with $\ell \to \langle \ell \rangle$ approximately coincides with Eq. (4.4) to the leading order.

	$\alpha = 1.5$	$\alpha = 2$	$\alpha = 3$	$\alpha = 4.5$	$\alpha = 7$
C_1	3.203	3.147	3.192	3.274	3.340
C_2	3.220	3.081	3.113	3.216	3.292
C_3	0.929	0.857	0.856	0.887	0.907

Table 4.1: Values of the fitting constants C_i of Eq. (4.4) for different values of α. The fittings were performed on the data of Figs. 4.5(f-j).

To complete the statistical inspection of k, in Figs. 4.5(k-o), we show that the variance of k grows with ℓ_0, approaches a maximum, and then decreases to zero for $\ell \to \sqrt{2}$; where the maximum is higher the larger the value of α is. Also, in Figs. 4.2(p-t), we plot the ratio $\sigma^2(k)/\langle k \rangle^2$ as a function of ℓ_0. It is interesting to note that for small α, $\sigma^2(k)/\langle k \rangle^2$ remains constant for increasing graph size (that is, the curves in panels (p,q) fall one on top of the other for different n), meaning that k is not a self-averaging quantity. On the contrary, for large α and small ℓ_0, the ratio $\sigma^2(k)/\langle k \rangle^2$ decreases with n (see the left part of the curves in panels (s,t)); so, under these conditions, k is a self-averaging quantity.

Now, we recall that increasing ℓ_0 from $\ell_0 \approx 0$ to $\ell_0 = \sqrt{2}$ drives the model of dRGGs from mostly isolated vertices to complete graphs. This transition, as a function of ℓ_0, could be well characterized by computing the average number of nonisolated vertices $\langle V_x(G) \rangle$ as well as the average values of the Randić and the Harmonic indices, see e.g. [118].

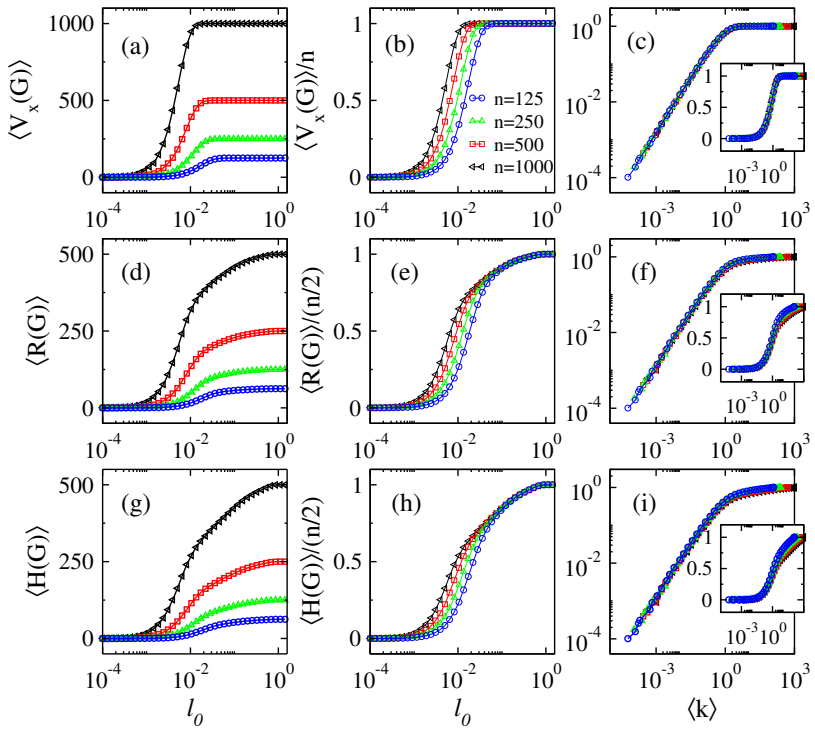

Figure 4.6: (a) Average number of nonisolated vertices $\langle V_x(G)\rangle$, (d) average Randić index $\langle R(G)\rangle$, and (g) average Harmonic index $\langle H(G)\rangle$ as a function of ℓ_0 of dRGGs characterized by $\alpha = 3$. In each panel we report results for graphs of four different sizes n. Normalized average indices $\langle V_x(G)\rangle/n$, $\langle R(G)\rangle/(n/2)$, and $\langle H(G)\rangle/(n/2)$ as a function of (b,e,h) ℓ_0 and (c,f,i) $\langle k\rangle$. The insets in (c,f,i) show the same curves of the main panels but in semilog scale. All averages were computed from $10^6/n$ random graphs. Figure taken from [30].

Certainly, we expect $\langle V_x(G)\rangle \approx 0$ when $\ell_0 \approx 0$ (that can be enhanced for large $\alpha > 0$ values) and $\langle V_x(G)\rangle = n$ for $\ell_0 = \sqrt{2}$.

Then, in Figs. 4.6(a,d,g) we present, respectively, the average number of nonisolated vertices $\langle V_x(G)\rangle$, the average Randić index $\langle R(G)\rangle$, and the average Harmonic index $\langle H(G)\rangle$ as a function of ℓ_0 of dRGGs characterized by $\alpha = 3$. We show curves for four different graph sizes n in each panel. As can be clearly seen, the three quantities $\langle X(G)\rangle$ (where X represents V_x, R or H) undergo a smooth transition (in log scale) from $\langle X(G)\rangle \approx 0$ for small ℓ_0 to the corresponding maxima $\max[X(G)]$ at $\ell_0 = \sqrt{2}$. Moreover, the normalized curves $\langle X(G)\rangle/\max[X(G)]$ vs. ℓ_0 have a very similar functional form but they are displaced to the left on the ℓ_0–axis for increasing n; see Figs. 4.6(b,e,h). In fact it was shown, for standard RGGs [118] and also for non-uniform RGGs [158], that these three normalized quantities scale with $\langle k\rangle$; that is, the curves $\langle X(G)\rangle/\max[X(G)]$ vs. $\langle k\rangle$ fall one on top

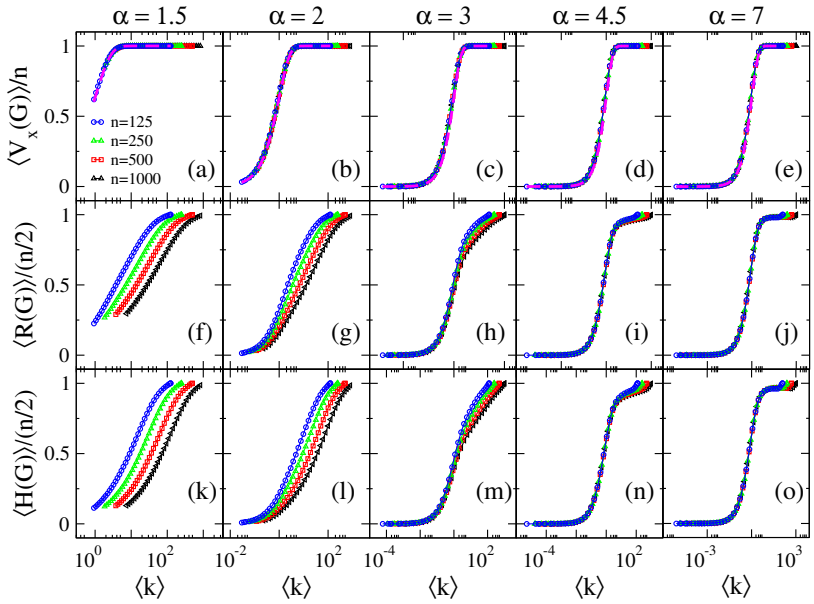

Figure 4.7: (a-e) Normalized average number of nonisolated vertices $\langle V_x(G)\rangle/n$, (f-j) normalized average Randić index $\langle R(G)\rangle/(n/2)$, and (k-o) normalized average Harmonic index $\langle H(G)\rangle/(n/2)$ as a function of the average degree $\langle k\rangle$ for dRGGs of four different sizes n. Magenta dashed lines in (a-e) are Eq. (4.7). Each column corresponds to a different value of the power-law decay α. All averages were computed from $10^6/n$ random graphs. Figure taken from [30].

of the other for different graph sizes. Therefore, we validate this scaling for dRGGs in Figs. 4.6(c,f,i) where we plot $\langle V_x(G)\rangle/n$, $\langle R(G)\rangle/(n/2)$ and $\langle H(G)\rangle/(n/2)$ vs. $\langle k\rangle$ in log-log scale (main panels) as well as in semilog scale (insets). We observe a very good scaling for the three quantities.

Furthermore, in Fig. 4.7 we explore the scaling of $\langle X(G)\rangle/\max[X(G)]$ with $\langle k\rangle$ for dRGGs characterized by values of α ranging from 1.5 to 7. We do confirm that $\langle V_x(G)\rangle/n$ shows a perfect scaling with $\langle k\rangle$ for all the values of α examined in this work; see Figs. 4.7(a-e). In contrast, the scaling of $\langle R(G)\rangle/n$ and $\langle H(G)\rangle/n$ with $\langle k\rangle$ is reasonably good for $\alpha > 3$ only; indeed for $\alpha < 3$ these two indices do not scale in any range of $\langle k\rangle$, see Figs. 4.7(f,g,k,l). We surmise that the lack of scaling of $\langle R(G)\rangle/n$ and $\langle H(G)\rangle/n$ with $\langle k\rangle$, for small α, may be related to the non self-averaging property of k for those values of α.

We also recall that an expression for $V_x(G)$ is known for standard RGGs [152]:

$$V_x(G) \approx n[1 - \exp(-n\pi\ell^2)], \tag{4.6}$$

which was recently generalized for both RGGs and non-uniform RGGs as [158]

$$\langle V_x(G)\rangle \approx n[1-\exp(-\langle k\rangle)]. \tag{4.7}$$

Then, given the perfect scaling of $\langle V_x(G)\rangle/n$ with $\langle k\rangle$ (meaning that $\langle V_x(G)\rangle/n$ is a function of $\langle k\rangle$ only), we test Eq. (4.7) on dRGGs by plotting it in Figs. 4.7(a-e); see the magenta dashed lines. Indeed, we do confirm that Eq. (4.7) describes perfectly well our numerical data for all α. This is a remarkable result because it stresses the universality of Eq. (4.7) on RGG models.

In fact, Eq. (4.7) allow us to write down an explicit expression for $\langle V_x(G)\rangle$ in terms of the model parameters $(n, \alpha > 3, \ell_0)$ by the use of Eqs. (4.2),(4.4), and (4.5):

$$\langle V_x(G)\rangle \approx n\left[1-\exp\left(-n\pi\left[\frac{\alpha-1}{\alpha-2}\,\ell_0^{\alpha-1}\frac{2^{1-\alpha/2}-\ell_0^{2-\alpha}}{(\ell_0/\sqrt{2})^{\alpha-1}-1}\right]^2\right)\right]. \tag{4.8}$$

4.3 Spectral properties

We now explore some spectral properties of dRGGs. We perform exact numerical diagonalization to obtain the eigenvalues λ_i and eigenvectors Ψ^i $(i = 1,\ldots,n)$ of large ensembles of randomly-weighted adjacency matrices characterized by the parameter set (n, α, ℓ_0) : $\mathbf{A_{nH}}$ from Eq. (3.2) and $\mathbf{A_H}$ from Eq. (3.1). Therefore, we can compute relevant spectral measures, such as $\langle r_{\mathbb{R}}(G)\rangle$, $\langle r_{\mathbb{C}}(G)\rangle$, $\langle \mathrm{IPR}(G)\rangle$, and $\langle S(G)\rangle$ defined in Chapter 3.

Thus, in Figs. 4.8(a,d,g) we present, respectively, the average ratio between consecutive eigenvalue spacings $\langle r_{\mathbb{C}}(G)\rangle$, the average inverse participation ratio $\langle \mathrm{IPR}(G)\rangle$, and the average Shannon entropy $\langle S(G)\rangle$ as a function of ℓ_0 for dRGGs characterized by $\alpha = 3$. Here the dRGGs are represented by the diluted RGE as stated in Subsection 3.1.2; i.e. by the non-Hermitian adjacency matrices $\mathbf{A_{nH}}$ of Eq. (3.2). In each panel we report results for graphs of four different sizes n. As for the structural measures (see Figs. 4.6(a,d,g) as a reference), the three spectral measures $\langle X(G)\rangle$ (where X represents $r_{\mathbb{C}}$, IPR or S) undergo a smooth transition (in log scale) from $\langle X(G)\rangle \approx X_{\mathrm{PE}}$ for $\ell_0 \approx 0$ to the corresponding maxima $\max[X(G)] = X_{\mathrm{RGE}}$ at $\ell_0 = \sqrt{2}$. To ease the analysis of these average quantities we normalize them according to Eqs. (3.9)-(3.11).

Then, in Figs. 4.8(b,e,h) we plot, respectively, the normalized average measures $\langle \overline{r}_{\mathbb{C}}(G)\rangle$, $\langle \overline{\mathrm{IPR}}(G)\rangle$, and $\langle \overline{S}(G)\rangle$ as a function of ℓ_0. Now the curves $\langle \overline{X}(G)\rangle$ vs. ℓ_0 have a very similar functional form but they are displaced to the left on the ℓ_0–axis for increasing

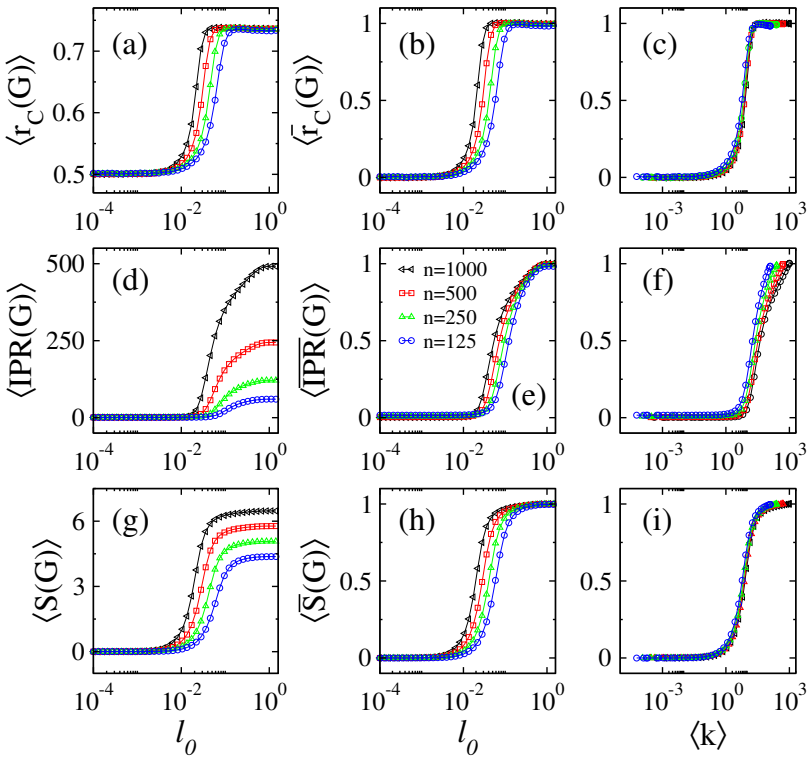

Figure 4.8: (a) Average ratio between consecutive eigenvalue spacings $\langle r_{\mathbb{C}}(G)\rangle$, (d) average inverse participation ratio $\langle IPR(G)\rangle$, and (g) average Shannon entropy $\langle S(G)\rangle$ as a function of ℓ_0 for dRGGs characterized by $\alpha = 3$. In each panel we report results for graphs of four different sizes n. Normalized average measures $\langle \overline{r}_{\mathbb{C}}(G)\rangle$, $\langle \overline{IPR}(G)\rangle$, and $\langle \overline{S}(G)\rangle$) as a function of (b,e,h) ℓ_0 and (c,f,i) $\langle k\rangle$. Here the dRGGs are represented by the diluted RGE. Figure taken from [30].

n. Following the idea of the previous section, in Figs. 4.8(c,f,i) we test whether the curves $\langle \overline{X}(G)\rangle$ scale with $\langle k\rangle$. Indeed we observe a reasonable good scaling of $\langle \overline{r}_{\mathbb{C}}(G)\rangle$ and $\langle \overline{S}(G)\rangle$ with $\langle k\rangle$; that is, the curves of $\langle \overline{r}_{\mathbb{C}}(G)\rangle$ and $\langle \overline{S}(G)\rangle$ vs. $\langle k\rangle$ fall one on top of the other for different graph sizes n. In contrast, we note that the scaling of $\langle \overline{\text{IPR}}(G)\rangle$ is not good, see Fig. 4.8(f). However, note that in Fig. 4.8 we are reporting results for dRGGs characterized by $\alpha = 3$ only. Then, in Fig. 4.9 we explore the scaling of $\langle \overline{X}(G)\rangle$ with $\langle k\rangle$ for dRGGs characterized by several values of α. As for the topological indices reported in Fig. 4.7, here we observe better scaling of spectral and eigenvector properties the larger the value of α is, even for $\langle \overline{\text{IPR}}(G)\rangle$; see Figs. 4.9(f-j).

We recall that the results in Figs. 4.8 and 4.9 are for dRGGs represented by the non-Hermitian adjacency matrices $\mathbf{A_{nH}}$ of Eq. (3.2). The question now is whether the Hermitian

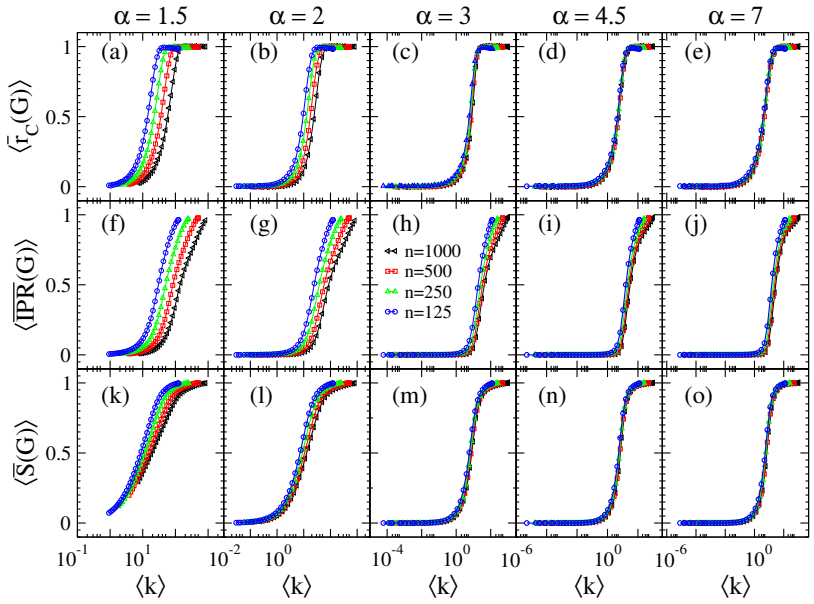

Figure 4.9: (a-e) Normalized average ratio between consecutive eigenvalue spacings $\langle \overline{r}_{\mathbb{C}}(G) \rangle$, (f-j) normalized average inverse participation ratio $\langle \overline{\text{IPR}}(G) \rangle$, and (k-o) normalized average Shannon entropy $\langle \overline{S}(G) \rangle$ as a function of $\langle k \rangle$ for dRGGs of four different sizes n. Each column corresponds to a different value of the power-law decay α. Here the dRGGs are represented by the diluted RGE. Figure taken from [30].

adjacency matrices $\mathbf{A_H}$ of Eq. (3.3) provide equivalent results. Then in Fig. 4.10 we plot the average normalized ratios $\langle r_{\mathbb{C}}(G) \rangle$ and $\langle r_{\mathbb{R}}(G) \rangle$ (we recall that $r_{\mathbb{C}}$ can be computed for real spectra too) for dRGGs represented by the MRME and characterized by several values of the power-law decay α. Again, these quantities are normalized according to their PE and MRME values (Eqs. (3.8)-(3.11)).

We just want to add that since the MRME reproduces the GOE only when the corresponding graphs are complete, the values for spectral and eigenvector measures have different values for $\ell \to \sqrt{2}$ and exactly at $\ell = \sqrt{2}$, as shown in Fig. 4.10 where we can see an abrupt decay of the curves at $\langle k \rangle_{max} = n - 1$, that is at $\ell = \sqrt{2}$.

Then, taking the $\mathbf{A_H}$ representation, we observe from Fig. 4.10, that the ratios $\langle r_{\mathbb{C}}(G) \rangle$ and $\langle r_{\mathbb{R}}(G) \rangle$ scale better with $\langle k \rangle$ the larger the value of α is. However, even for small α (see Fig. 4.10(a,f) corresponding to $\alpha = 1.5$) the scaling is reasonably good. This is in contrast with $\langle r_{\mathbb{C}}(G) \rangle$ when computed on $\mathbf{A_{nH}}$, see Fig. 4.9(a), where the curves of $\langle r_{\mathbb{C}}(G) \rangle$ for different graph sizes n are clearly displaced on the $\langle k \rangle$–axis. Additionally, in Fig. 4.11 we plot $\langle \overline{\text{IPR}}(G) \rangle$ and $\langle \overline{S}(G) \rangle$ as a function of $\langle k \rangle$ for dRGGs represented by

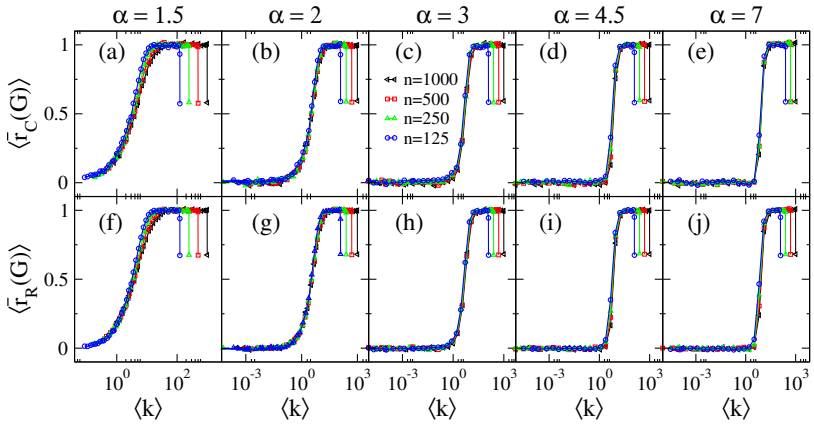

Figure 4.10: Normalized average ratios (a-e) $\langle \overline{r}_{\mathbb{C}}(G) \rangle$ and (f-j) $\langle \overline{r}_{\mathbb{R}}(G) \rangle$ as a function of $\langle k \rangle$ for dRGGs of four different sizes n. Each column corresponds to a different value of the power-law decay α. Here the dRGGs are represented by the MRME. Figure taken from [30].

the MRME. A visual comparison of Fig. 4.11 with Fig. 4.9 reveals that the eigenvector properties of the MRME scale with $\langle k \rangle$ better than those computed for the diluted RGE. Therefore, to support this statement in what follows we perform a scaling study of the spectral and eigenvector properties of both adjacency matrix ensembles $\mathbf{A_{nH}}$ and $\mathbf{A_H}$ for dRGGs.

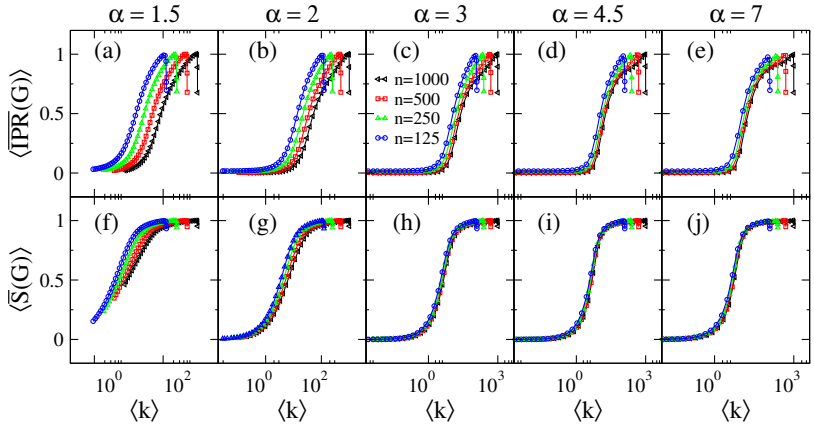

Figure 4.11: (a-e) Normalized average inverse participation ratio $\langle \overline{\mathrm{IPR}}(G) \rangle$ and (f-j) normalized average Shannon entropy $\langle \overline{S}(G) \rangle$ as a function of $\langle k \rangle$ for dRGGs of four different sizes n. Each column corresponds to a different value of the power-law decay α. Here the dRGGs are represented by the MRME. Figure taken from [30].

4.4 Scaling analysis

So far, we analyzed spectral properties of dRGGs. Specifically, we reported the average ratio between consecutive eigenvalue spacings $\langle r_{\mathbb{C}}(G)\rangle$, the average inverse participation ratio $\langle \mathrm{IPR}(G)\rangle$, and the average Shannon entropy $\langle S(G)\rangle$ of dRGGs represented by the diluted RGE (i.e. by random non-Hermitian adjacency matrices $\mathbf{A_{nH}}$), see Figs. 4.8 and 4.9. And for dRGGs represented by the MRME (i.e. by random Hermitian adjacency matrices $\mathbf{A_H}$) we have reported the same measures plus the ratio between consecutive level spacings $\langle r_{\mathbb{R}}(G)\rangle$, see Fig. 4.10. Until now, we have observed that the average degree $\langle k\rangle$ do not scale the curves of the spectral and eigenvector measures $X(G)$ since the curves are displaced in the $\langle k\rangle$-axis showing a clear dependence on the size of the network n. In addition, we observed that the MRME ensemble seems to perform a better scaling prediction with $\langle k\rangle$ than the RGE. Consequently, we perform a scaling analysis; that is, to find the scaling parameter ξ such that the properly normalized curves $\langle \overline{X}(G)\rangle$ vs. ξ are *universal* curves; here X representes both spectral and structural measures. We stress that finding a scaling parameter is of very practical importance for the complete characterization of the measures permits to predict properties of networks of any other size without the need of additional computation. Thus, here we look for the scaling parameter $\xi = \xi(n, \langle k\rangle)$, of both $\mathbf{A_{nH}}$ and $\mathbf{A_H}$, such that the curves $\langle \overline{X}(G)\rangle$ vs. ξ remain invariant; here X stands for $r_{\mathbb{C}}$, IPR, and S.

Note that all curves $\langle \overline{X}(G)\rangle$ vs. $\langle k\rangle$ show a transition from approximately 0, when $\ell_0 \approx 0$, to 1, when $\ell_0 \to \sqrt{2}$, (see Figs. 4.9, 4.10 and 4.11) but they are displaced along the $\langle k\rangle$–axis for different values of n (also note from Fig. 4.10 that this displacement is almost negligible for $r_{\mathbb{C}}$ and $r_{\mathbb{R}}$ in the case of the MRME, meaning that $\xi \approx \langle k\rangle$ in that case). Then, we characterize the position of the curves $\langle \overline{X}(G)\rangle$ vs. $\langle k\rangle$ along the $\langle k\rangle$–axis by the values of $\langle k\rangle$ for which $\langle \overline{X}(G)\rangle \approx 0.5$. We label the values of $\langle k\rangle$ at half of the full transition as $\langle k\rangle^*$. As observed in Figs. 4.14 and 4.15, a linear trend of the data sets (in log-log scale) $\langle k\rangle^*$ vs. n suggests a power-law behavior of the form

$$\langle k\rangle^* = Cn^{\delta}. \tag{4.9}$$

Thus we define the scaling parameter as the ratio between $\langle k\rangle$ and $\langle k\rangle^*$:

$$\xi \equiv \frac{\langle k\rangle}{\langle k\rangle^*} = \frac{\langle k\rangle}{Cn^{\delta}} \propto n^{-\delta}\langle k\rangle. \tag{4.10}$$

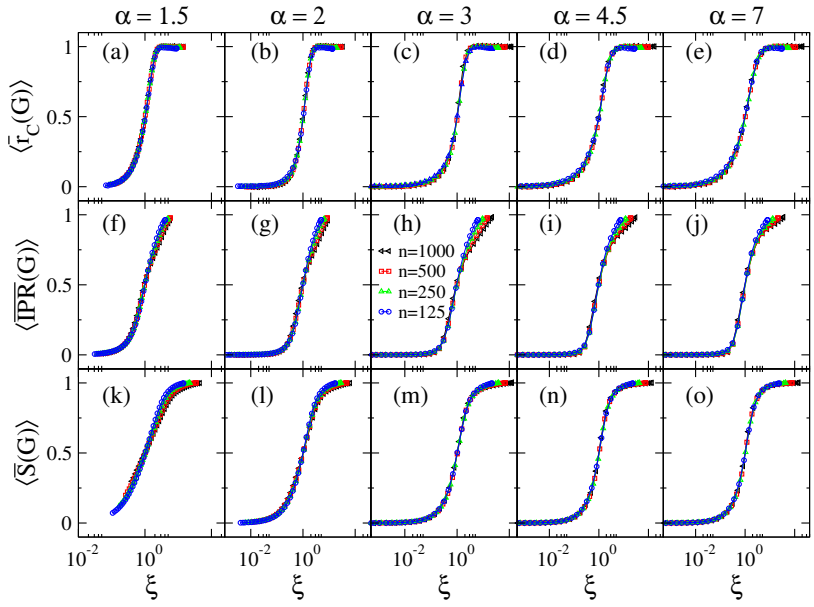

Figure 4.12: (a-e) Normalized average ratio $\langle \overline{r}_{\mathbb{C}}(G) \rangle$, (f-j) normalized average inverse participation ratio $\langle \overline{\mathrm{IPR}}(G) \rangle$, and (k-o) normalized average Shannon entropy $\langle \overline{S}(G) \rangle$ as a function of ξ for dRGGs of four different sizes n. Each column corresponds to a different value of the power-law decay α. Here the dRGGs are represented by the diluted RGE. Figure taken from [30].

Therefore, by plotting again the curves of $\langle \overline{X}(G) \rangle$ now as a function of ξ we observe, in particular for $\alpha \geq 3$, that curves for different graph sizes n collapse on top of universal curves; see Fig. 4.12 for the diluted RGE and Fig. 4.13 for the MRME.

$\langle \overline{r}_{\mathbb{C}}(G) \rangle$		$\alpha = 1.5$	$\alpha = 2$	$\alpha = 3$	$\alpha = 4.5$	$\alpha = 7$
diluted RGE	C	0.519	1.012	2.372	2.837	2.586
	δ	0.679	0.458	0.181	0.095	0.092
MRME	C	1.514	2.449	2.588	3.538	5.992
	δ	0.141	0.054	0.099	0.090	0.056

Table 4.2: Values of the parameters C and δ of Eq. (4.10) obtained from the fittings of the curves $\langle k \rangle^*(\langle \overline{r}_{\mathbb{C}}(G) \rangle)$ vs. n for the diluted RGE and the MRME with different values of α.

In addition, it is useful to look at the values of the exponent δ of Eq. (4.10) obtained from the fittings of the curves $\langle k \rangle^*$ vs. n, which are reported in Tables 4.2, 4.3 and 4.4 for $\langle \overline{r}_{\mathbb{C}}(G) \rangle$, $\langle \overline{\mathrm{IPR}}(G) \rangle$ and $\langle \overline{S}(G) \rangle$, respectively. From Table 4.2 we can clearly see, for all the values of α reported here, that the values of δ for the MRME are smaller than those for the diluted RGE. Moreover, since $\delta \approx 0$ for the MRME, we can claim that $\langle k \rangle$

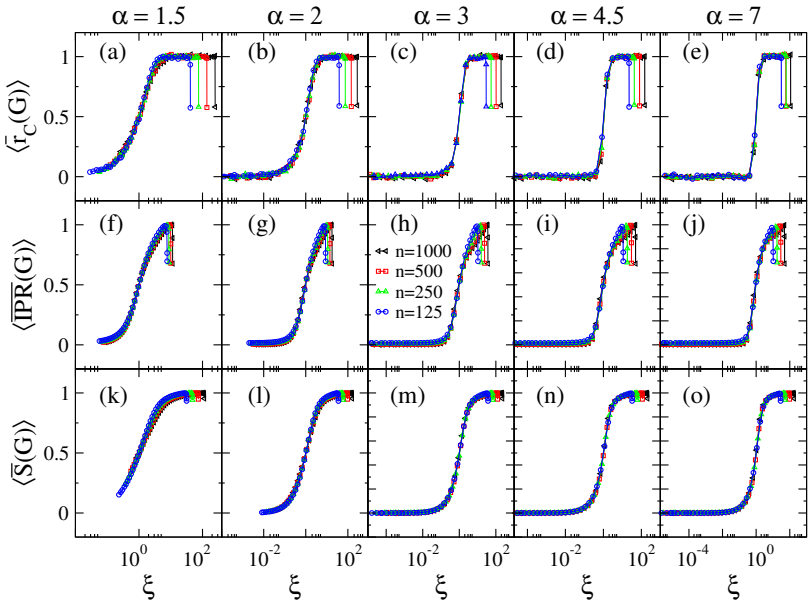

Figure 4.13: (a-e) Normalized average ratio $\langle \overline{r}_{\mathbb{C}}(G) \rangle$, (f-j) normalized average inverse participation ratio $\langle \overline{\mathrm{IPR}}(G) \rangle$, and (k-o) normalized average Shannon entropy $\langle \overline{S}(G) \rangle$ as a function of ξ for dRGGs of four different sizes n. Each column corresponds to a different value of the power-law decay α. Here the dRGGs are represented by the MRME. Figure taken from [30].

$\langle \overline{\mathrm{IPR}}(G) \rangle$		$\alpha = 1.5$	$\alpha = 2$	$\alpha = 3$	$\alpha = 4.5$	$\alpha = 7$
diluted RGE	C	0.804	1.298	2.824	3.476	3.557
	δ	0.751	0.612	0.402	0.323	0.303
MRME	C	0.320	0.578	1.738	2.847	3.505
	δ	0.812	0.662	0.398	0.283	0.254

Table 4.3: Values of the parameters C and δ of Eq. (4.10.xi) obtained from the fittings of the curves $\langle k \rangle^*(\langle \overline{\mathrm{IPR}}(G) \rangle)$ vs. n for the diluted RGE and the MRME with different values of α.

$\langle \overline{S}(G) \rangle$		$\alpha = 1.5$	$\alpha = 2$	$\alpha = 3$	$\alpha = 4.5$	$\alpha = 7$
diluted RGE	C	1.487	1.960	2.669	2.746	2.691
	δ	0.364	0.270	0.158	0.136	0.139
MRME	C	0.602	0.888	1.701	2.189	2.383
	δ	0.389	0.282	0.138	0.113	0.124

Table 4.4: Values of the parameters C and δ of Eq. (4.10) obtained from the fittings of the curves $\langle k \rangle^*(\langle \overline{S}(G) \rangle)$ vs. n for the diluted RGE and the MRME with different values of α.

is indeed the scaling parameter of $\langle \overline{r}_{\mathbb{C}}(G) \rangle$ for this ensemble of adjacency matrices, as was already observed in Fig. 4.10. The situation is quite different for $\langle \overline{\mathrm{IPR}}(G) \rangle$ and $\langle \overline{S}(G) \rangle$,

$\langle\overline{r}_{\mathbb{R}}(G)\rangle$		$\alpha = 1.5$	$\alpha = 2$	$\alpha = 3$	$\alpha = 4.5$	$\alpha = 7$
MRME	C	1.641	2.583	2.752	3.424	3.135
	δ	0.131	0.058	0.098	0.12	0.14

Table 4.5: Values of the parameters C and δ of Eq. (4.10) obtained from the fittings of the curves $\langle k\rangle^*(\langle\overline{r}_{\mathbb{C}}(G)\rangle)$ vs. n for the diluted RGE and the MRME with different values of α.

see Tables 4.3 and 4.4 there the values of δ for the MRME are smaller than those for the diluted RGE only when $\alpha \geq 3$. This means that only for $\alpha \geq 3$ (when k is a self-averaging quantity) the eigenvector measures scale better with $\langle k\rangle$ for the MRME than for the diluted RGE. Anyway, the scaling of the eigenvector measures of both random adjacency matrix ensambles seems to be acceptable for $\alpha \geq 3$ only, where the curves $\langle\overline{X}(G)\rangle$ vs. ξ are clearly invariant (i.e. they fall one on top of the other for different n). So, a deeper study of the statistical properties of k, in particular the self-averaging property, seems to be necessary.

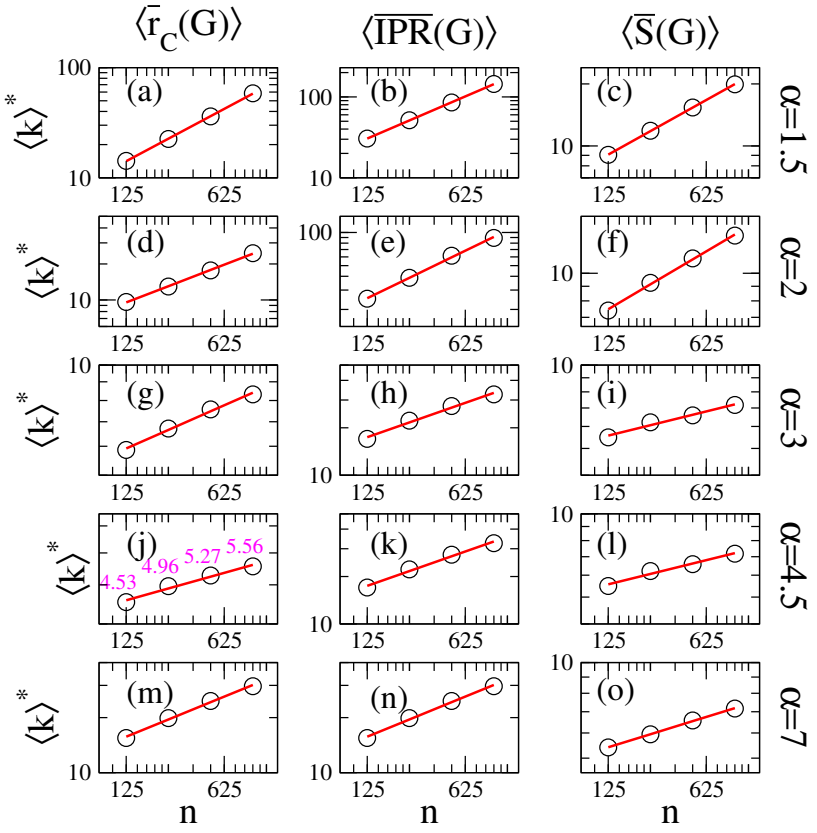

Figure 4.14: Curves $\langle k \rangle^*$ vs. n in log-log scale for the (a, d, g, j , m) normalized average ratio between nearest- and next to-nearest-neighbor eigenvalue distances $\langle \overline{r}_{\mathbb{C}}(G) \rangle$, (b, e, h, k, n) normalized average inverse participation ratio $\langle \overline{\text{IPR}}(G) \rangle$, and (c, f, i, l, o) normalized average Shannon entropy $\langle \overline{S}(G) \rangle$ of the dRGG using the RGE ensemble. We show the five different power-law exponent configurations $\alpha = 1.5$, $\alpha = 2$, $\alpha = 3$, $\alpha = 4.5$, and $\alpha = 7$ (from top to bottom). In every panel the red line is the best fit to the data as Eq. (4.9). The fiting values are reported in Tables 4.2, 4.3, and 4.4. In some panels the data values are shown to help visualize the scale.

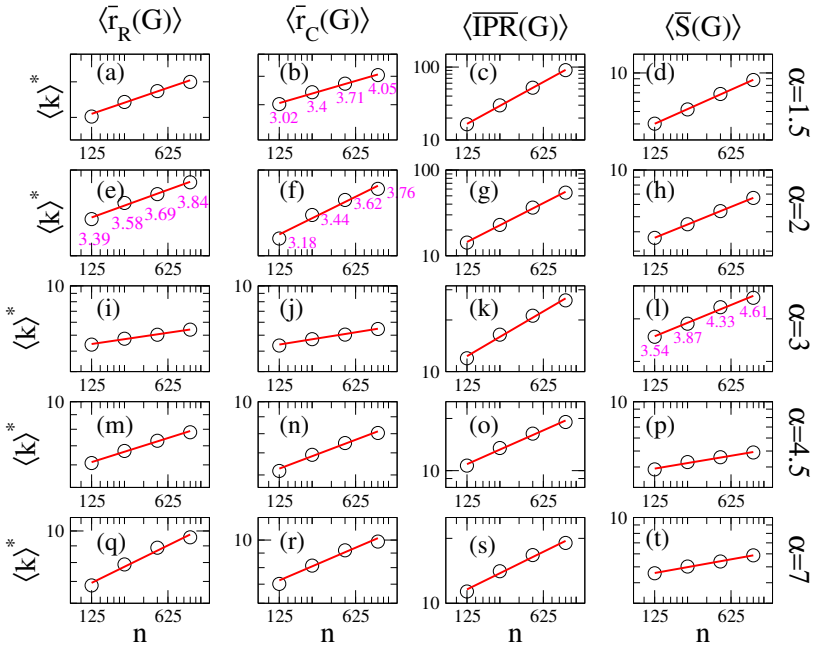

Figure 4.15: Curves $\langle k\rangle^*$ vs. n in log-log scale for the (a, e, i, m ,q) normalized average ratio between consecutive eigenvalue spacings $\langle \overline{r}_{\mathbb{R}}(G)\rangle$, (b, f, j, n, r) normalized average ratio between nearest- and next to-nearest-neighbor eigenvalue distances $\langle \overline{r}_{\mathbb{C}}(G)\rangle$, (c, g, k, o, s) normalized average inverse participation ratio $\langle \overline{\text{IPR}}(G)\rangle$, and (d, h, l, p, t) normalized average Shannon entropy $\langle \overline{S}(G)\rangle$ of the dRGG using the MRME ensemble. We show the five different power-law exponent configurations $\alpha = 1.5$, $\alpha = 2$, $\alpha = 3$, $\alpha = 4.5$, and $\alpha = 7$ (from top to bottom). In every panel the red line is the best fit to the data as Eq. (4.9). The fiting values are reported in Tables 4.2, 4.3, 4.4, and 4.5. In some panels the data values are shown to help visualize the scale.

Chapter 5

Hyperbolic random graph

In this chapter we show a study of structural and spectral properties of hyperbolic random geometric graphs (HRGs) with quasi-uniform node density and arbitrary curvature by means of a random matrix theory (RMT) approach. Specifically, through a numerical study of the topological indices and clustering coefficients defined in Chapter 2, and the spectral measures defined in Chapter 3 by using orthogonal random adjacency matrices. As in Chapter 4, here we perform a scaling analysis through the use of the average degree $\langle k \rangle$ and show that Euclidean random geometric graphs and hyperbolic random graph share important average properties over a graph ensemble. This chapter is based on the work published in [153].

5.1 Random graph model

As a natural extension of conventional spatial networks such as the random geometric graph (RGG), the hyperbolic random graph (HRG) model introduced in [14, 34] allows to represent nodes separated by exponential distances on the hyperbolic plane $\mathbb{H}^2_\zeta$, while simultaneously presenting scale-free degree distributions (as in the original preferential attachment model [15]), strong clustering, sparseness, community structure [14, 154, 155], and self-similarity [156]. Hyperbolic random geometric graphs (HRGs) are formed by distributing n nodes in a hyperbolic disk $\mathbb{H}^2_\zeta$ of fixed radius ρ as follows:

- The vertex radial coordinates r are drawn from the density function [14]

$$f(r) = \alpha \frac{\sinh(\alpha r)}{\cosh(\alpha \rho) - 1}, \tag{5.1}$$

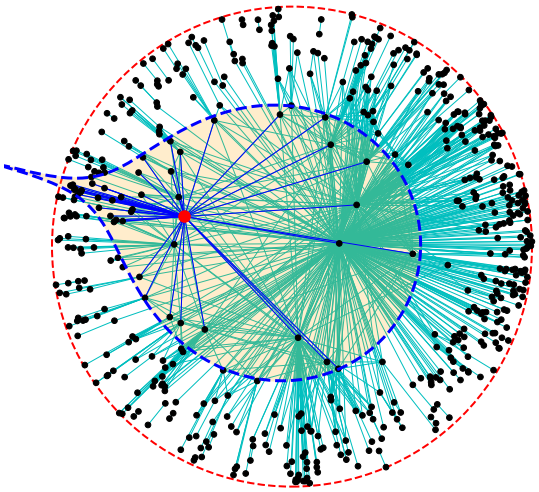

Figure 5.1: HRG with $n = 1000$ vertices, $\rho = 5$, $\zeta = 4$ ($K = -16$), and distribution exponent $\alpha = 2$. The connection disk of radius ρ of the highlighted red node is delimited by blue dashed line (orange shaded area). The vertices within the disk of connection are linked to the red node, those edges are displayed in solid blue lines.

where α is the exponent of the distribution.

- Angular coordinates θ of the vertices are assigned from the uniform density

$$g(\theta) = \frac{1}{2\pi}. \tag{5.2}$$

- Vertices are connected with the connection probability function

$$p(x_{ij}) = \Theta(\rho - x_{ij}), \tag{5.3}$$

where x_{ij} is the hyperbolic distance between nodes i and j (with polar coordinates (r_i, θ_i) and (r_j, θ_j), respectively) which satisfies the hyperbolic law of cosines

$$\cosh \zeta x_{ij} = \cosh(\zeta r_i) \cosh(\zeta r_j) - \sinh(\zeta r_i) \sinh(\zeta r_j) \cos(\Delta\theta). \tag{5.4}$$

Here, $\Delta\theta = \pi - |\pi - |\theta_i - \theta_j||$ and ζ is the parameter that controls the curvature of the embedding hyperbolic space: $K = -\zeta^2$. Here K is Gaussian curvature.

In Fig. 5.1 we show a HRG with $n = 1000$ nodes inside a hyperbolic disk of radius $\rho = 5$ from the origin and gaussian curvature $K = -16$. The connection disk of the highlighted

red node is depicted by a blue dashed line (orange shaded area) according to Eq. (5.3); where vertices lying inside the connection disk are linked to the red node (central node of the connection disk) exemplifying the construction of the entire graph. Here, we should note that the connection disk is deformed to the eye due to the fact that the distances in the hyperbolic plane $\mathbb{H}^2$ increase exponentially as they part from the origin. This can be clearly seen from Eq. (5.4): as r increases, distances x grow exponentially. For this reason, nodes located near the center of the disk have smaller hyperbolic distances and connect more easily, while nodes located near the boundary have exponentially large distances between them and fewer edges, even if they look close.

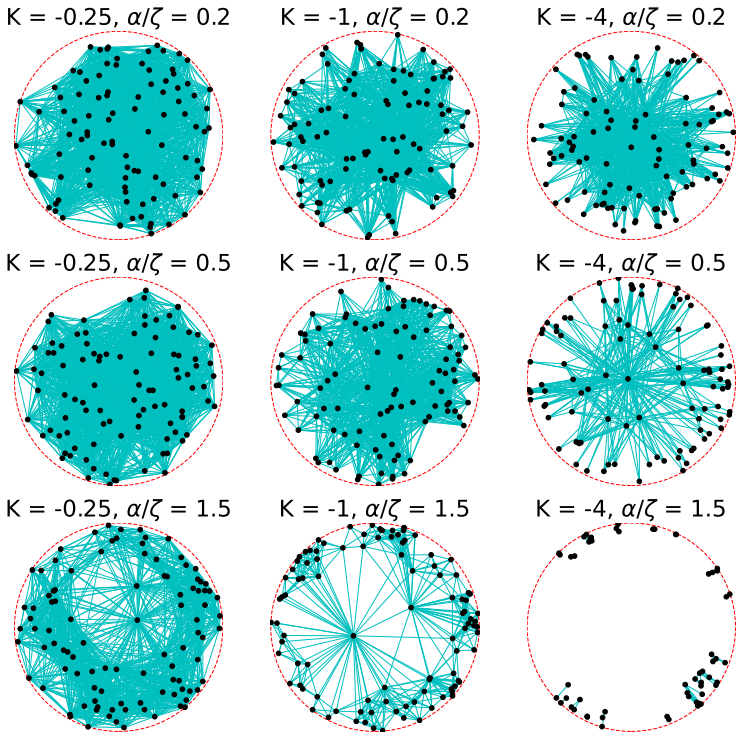

Figure 5.2: HRGs with $n = 100$ nodes and disk radius $\rho = 5$. Different curvatures are shown: $K = -0.25$ (left column), $K = -1$ (middle column), and $K = -4$ (left column). Different ratios α/ζ are shown: $\alpha/\zeta = 0.2$ (upper row), $\alpha/\zeta = 0.5$ (middle row), and $\alpha/\zeta = 1.5$ (lower row).

Thus, the HRG model is defined by the number of nodes n, the disk radius ρ, the radial distribution exponent $\alpha > 0$, and the curvature parameter $\zeta > 0$. Moreover, the purely intrinsic geometry construction of the graph allows for heterogeneous degree

distributions of the form [14]

$$P(k) \propto k^{-\beta}, \quad \text{with} \quad \beta = \begin{cases} 2\alpha/\zeta + 1 & \text{if } \alpha/\zeta \geq 1/2 \\ 2 & \text{if } \alpha/\zeta \leq 1/2 \end{cases}. \tag{5.5}$$

From Eq. (5.5) we see that the power-law exponent β of the degree distribution is determined by the ratio α/ζ. Then, the structure of the HRG is defined as a graph $G = G(n, \rho, \alpha/\zeta)$, with α/ζ completely defining the heterogeneity of the degrees and the intrinsic geometry. Therefore, since we want to explore the general behavior of the model, we characterize structural and spectral properties of HRGs for three parametric scenarios: $\alpha/\zeta < 1/2$, $\alpha/\zeta = 1/2$ and $\alpha/\zeta > 1/2$. Specifically, without loss of generality, we consider the ratios $\alpha/\zeta = 0.2$, $\alpha/\zeta = 0.5$ and $\alpha/\zeta = 1.5$ and explore different curvature configurations. In Fig. 5.2 we show HRGs with $n = 100$ and $\rho = 5$ for different curvatures and different ratios; namely, $\alpha/\zeta = 0.2$, $\alpha/\zeta = 0.5$, and $\alpha/\zeta = 1.5$. For a fixed radius ρ we observe that as the curvature K [ratio α/ζ] increases (from left to right [from top to bottom]) nodes are located (visually) farther apart from the center of the disk.

5.2 Structural properties

We first revise the properties of the vertex degree k. In Figs. 5.3(a-c) we plot the average degree $\langle k \rangle$ as a function of the Poincaré disk radius ρ of HRGs characterized by $\alpha/\zeta = 0.2$ (left panel), $\alpha/\zeta = 0.5$ (middle panel), and (c) $\alpha/\zeta = 1.5$ (right panel). In each panel we show curves for five values of the curvature $K = -\zeta^2$ (different symbols) for graphs of size $n = 1000$. As expected, the curves $\langle k \rangle$ vs. ρ show a crossover from full graphs, $\langle k \rangle = n - 1$ when $\rho \to 0$, to isolated vertices. Indeed, the exponential decay of $\langle k \rangle$ with ρ is well described by the analytical prediction of [14],

$$\langle k \rangle = \begin{cases} \frac{n\zeta\rho}{2}\left(1 + \frac{\zeta\rho}{2\pi}\right)e^{-\zeta\rho/2}, & \text{if } \frac{\alpha}{\zeta} = \frac{1}{2} \\ \frac{2\xi^2 n}{\pi}\left(e^{-\zeta\rho/2} + e^{-\alpha\rho}\left\{\frac{\alpha\rho}{2}\left[\frac{\pi\zeta^2}{4\alpha^2}\right.\right.\right. & \\ \left.\left.\left. -\frac{(\pi-1)\zeta}{\alpha} + \pi - 2\right] - 1\right\}\right), & \text{if } \frac{\alpha}{\zeta} < \frac{1}{2},\ \frac{\alpha}{\zeta} > \frac{1}{2} \end{cases} \tag{5.6}$$

where $\xi = (\alpha/\zeta)\,(\alpha/\zeta - 1/2)$; see the cyan lines in Figs. 5.3(a-c). Moreover, in Figs. 5.3(d-f) we present the variance of k normalized to n^2 as a function of $\langle k \rangle$ for three graph sizes, $n = 250$, 500 and 1000, using different values of the curvature K while keeping a constant ratio α/ζ in each panel. From Figs. 5.3(d-f), we observe the rapid increase of $\sigma^2(k)$ with

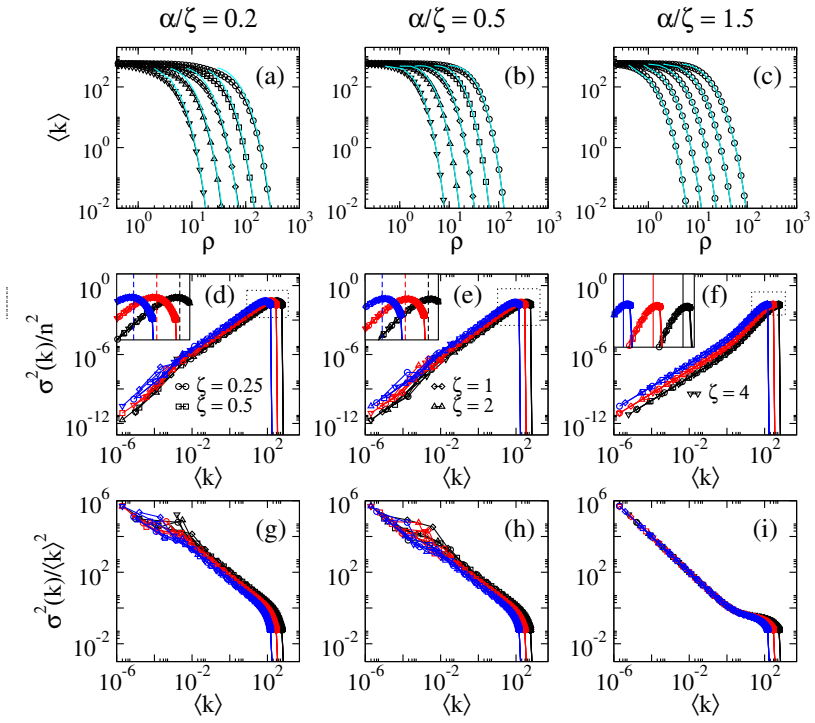

Figure 5.3: (a-c) Average degree $\langle k \rangle$ of hyperbolic random graphs of size $n = 1000$ as a function of the hyperbolic disk radius ρ for five different values of the curvature $K = -\zeta^2$ (symbols). Cyan solid lines correspond to the analytical prediction of $\langle k \rangle$ given by Eq. (5.6). (d-f) The variance of k, $\sigma^2(k)$, normalized to n^2 as a function of $\langle k \rangle$. (g-i) The relative variance of k as a function of $\langle k \rangle$. The HRGs are characterized by the ratios $\alpha/\zeta = 0.2$ (left panels), $\alpha/\zeta = 0.5$ (middle panels), and (c) $\alpha/\zeta = 1.5$ (right panels). Insets in (d-f) zoom in on the black dashed squares. In (d) and (e), vertical dashed lines mark $\langle k \rangle = n/3$ (log-log scale); in (i), solid lines mark $\langle k \rangle = n/2$ (log-log scale). Each panel (d-i) displays curves for five values of the curvature $K = -\zeta^2$ (different symbols) for each of three graph sizes: $n = 250$ (blue), $n = 500$ (red) and $n = 1000$ (black). Each data value was computed from an ensemble of $10^6/n$ graphs. Figure and description taken from [153].

$\langle k \rangle$, reaching a maximum about $\langle k \rangle \approx 10^2$ before dropping to zero. In fact, the normalized variance $\sigma^2(k)/n^2$ is size dependent as in insets of panel (d-f) we observe that the maximum of each curve is reached at $\langle k \rangle \approx n/3$ when $\alpha/\zeta \leq 1/2$ and at $\langle k \rangle \approx n/2$ when $\alpha/\zeta = 1.5$ in the inset of panel (f). This is an evidence of the level of heterogeneity of the network as described by Eq. (5.5) since maximum variance is gotten for $\langle k \rangle > n/3$ as $\alpha/\zeta > 1/2$. In addition we observe, for any fixed graph size no matter the curvature, that the curves $\sigma^2(k)/n^2$ vs. $\langle k \rangle$ fall one on top of the other. Then, in Figs. 5.3(g-i) we explore the relative variance of k as a function of $\langle k \rangle$. We note then, that the fact that $\sigma(k)^2/\langle k \rangle^2$ does not

decrease with n (for a fixed $\langle k \rangle$) makes k a non self-averaging quantity. Also we note that the non self-averaging property of k is stronger for $\alpha/\zeta \leq 0.5$.

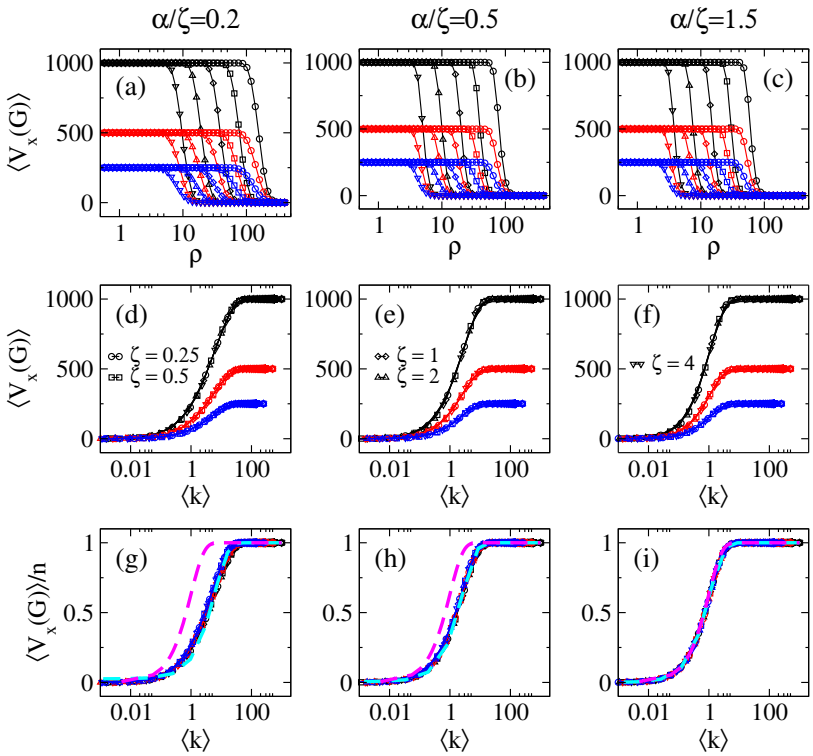

Figure 5.4: Number of non-isolated vertices $\langle V_x(G) \rangle$ of hyperbolic random graphs as a function of (a-c) the disk radius ρ and (d-f) the average degree $\langle k \rangle$. (g-i) $\langle V_x(G) \rangle$, normalized to the graph size n, as a function of $\langle k \rangle$. The HRGs are characterized by the ratios $\alpha/\zeta = 0.2$ (left panels), $\alpha/\zeta = 0.5$ (middle panels), and (c) $\alpha/\zeta = 1.5$ (right panels). Each panel displays curves for five values of the curvature $K = -\zeta^2$ (different symbols) for each of three graph sizes: $n = 250$ (blue), $n = 500$ (red) and $n = 1000$ (black). Each data value was computed from an ensemble of $10^6/n$ graphs. Magenta dashed lines in panels (g-i) correspond to Eq. (5.7). Cyan dashed lines in panels (g,h) correspond to fittings of Eq. (5.8) to the data with the fitting parameter (g) $\gamma \approx 0.2$, (h) $\gamma \approx 0.44$, and (i) $\gamma \approx 0.93$. Figure and description taken from [153].

Then in Figs. 5.4(a-c) we present the average number of non-isolated vertices $\langle V_x(G) \rangle$ (see Eq. (2.17)) as a function of the disk radius ρ of HRGs characterized by $\alpha/\zeta = 0.2$ (left panel), $\alpha/\zeta = 0.5$ (middle panel), and (c) $\alpha/\zeta = 1.5$ (right panel). In each panel we include curves for five values of the curvature $K = -\zeta^2$ (different symbols) for each of three graph sizes n (different colors). First, we note that for each parameter combination (n, α, ζ), the curves $\langle V_x(G) \rangle$ vs. ρ show a crossover from full graphs, $\langle V_x(G) \rangle = n$ when

$\rho \to 0$, to isolated vertices, $\langle V_x(G)\rangle = 0$ for $\rho \gg 1$. Indeed, from Figs. 5.4(a-c) we can clearly see that the smaller the value of the ratio α/ζ the wider the range of ρ (at small ρ) for which $\langle V_x(G)\rangle$ is maximal, meaning complete graphs. In fact, this observation coincides with the results reported in [157] for $\alpha/\zeta < 0.5$.

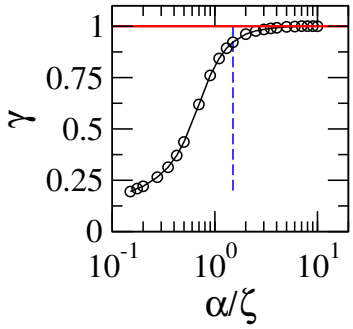

Figure 5.5: Parameter γ as a function of the ratio α/ζ as obtained from the fittings of Eq. (5.8) to numerical data. Red full line marks $\gamma = 1$. Blue dashed line corresponds to $\alpha/\zeta = 1.5$. Error bars are not shown since they are much smaller than the symbol size. Figure and description taken from [153].

In previous works, the number of nonisolated vertices $\langle V_x(G)\rangle$ for RGGs has been reported as a simple function of the average degree $\langle k\rangle$, specifically, [30, 158]

$$\langle V_x(G)\rangle \approx n[1 - \exp(-\langle k\rangle)]. \tag{5.7}$$

Therefore, in Figs. 5.4(d-f) we show again the curves of $\langle V_x(G)\rangle$ of Figs. 5.4(a-c) but now as a function of $\langle k\rangle$. Indeed, we observe that curves for different values of K collapse on top of a single curve. Moreover, in Figs. 5.4(g-i) we present $\langle V_x(G)\rangle$, normalized to the graph size n, as a function of $\langle k\rangle$ and observe the complete collapse of all curves in each panel. Also in Figs. 5.4(g-i) we include Eq. (5.7), as magenta dashed lines, and observe that it coincides with the numerical data for $\alpha/\zeta = 1.5$ only; see Fig. 5.4(i). For this reason, as a next step, we perform a numerical fitting as we observe that

$$\langle V_x(G)\rangle \approx n[1 - \exp(-\gamma\langle k\rangle)], \tag{5.8}$$

where $\gamma \equiv \gamma(\alpha/\zeta)$ is a fitting parameter, reproduces well the curves $\langle V_x(G)\rangle$ vs. $\langle k\rangle$ for all the ratios α/ζ; see the cyan dashed lines in Figs. 5.4(g-i) where the values of γ obtained from the fittings are $\gamma \approx 0.2$, $\gamma \approx 0.44$ and $\gamma \approx 0.93$ (see the blue-dashed line in Fig. 5.5). In fact, a detailed characterization of the dependence of γ on the ratio α/ζ is illustrated

in Fig. 5.5 where the asymptotic convergence to $\gamma = 1$ is clear as α/ζ grows. This shows that the number of non-isolated vertices $V_x(G)$ for HRGs tends to the prediction for RGGs when $\alpha/\zeta \to \infty$.

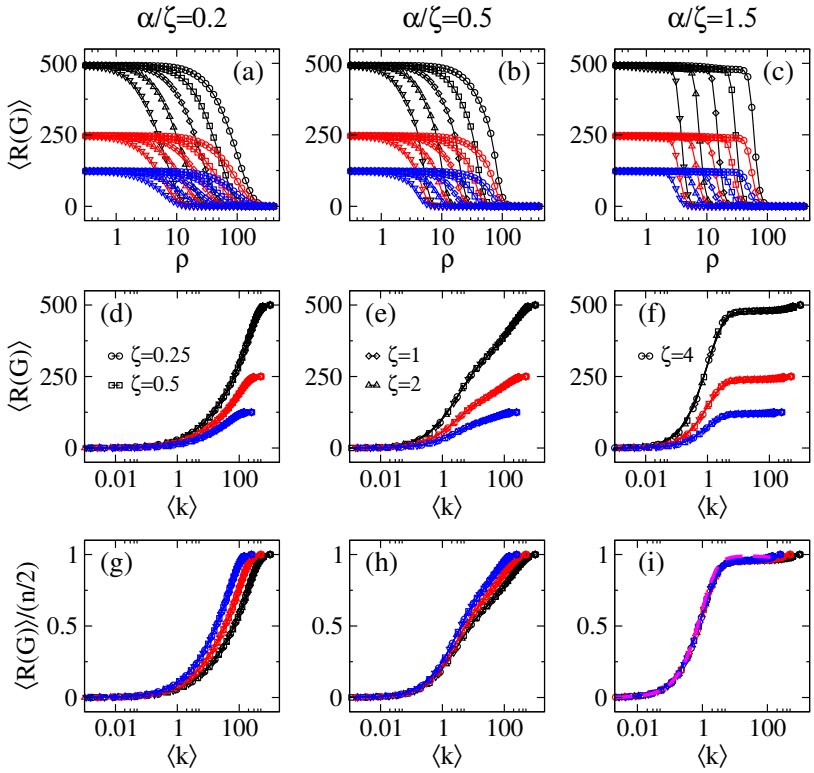

Figure 5.6: Average Randić index $\langle R(G)\rangle$ of hyperbolic random graphs as a function of (a-c) the disk radius ρ and (d-f) the average degree $\langle k\rangle$. (g-i) $\langle R(G)\rangle$, normalized to $n/2$, as a function of $\langle k\rangle$. The HRGs are characterized by the ratios $\alpha/\zeta = 0.2$ (left panels), $\alpha/\zeta = 0.5$ (middle panels), and (c) $\alpha/\zeta = 1.5$ (right panels). Each panel displays curves for five values of the curvature $K = -\zeta^2$ (different symbols) for each of three graph sizes: $n = 250$ (blue), $n = 500$ (red) and $n = 1000$ (black). Each data value was computed from an ensemble of $10^6/n$ graphs. Magenta dashed line in panel (i) corresponds to RGGs in the unit square with $n = 250$. Figure and description taken from [153].

Now, in Figs. 5.6 and 5.7 we present the average Randić and Harmonic indices from Eqs. (2.15)-(2.16), respectively, of HRGs characterized by $\alpha/\zeta = 0.2$ (left panels), $\alpha/\zeta = 0.5$ (middle panels), and (c) $\alpha/\zeta = 1.5$ (right panels). For comparison purposes Figs. 5.6 and 5.7 have the same format as Fig. 5.4 for $\langle V_x(G)\rangle$: Panels (a-c) show $\langle R(G)\rangle$ and $\langle H(G)\rangle$ as a function of ρ, panels (d-f) show $\langle R(G)\rangle$ and $\langle H(G)\rangle$ as a function of $\langle k\rangle$, while panels (g-i) show $\langle R(G)\rangle$ and $\langle H(G)\rangle$, normalized to $n/2$, as a function of $\langle k\rangle$. Each

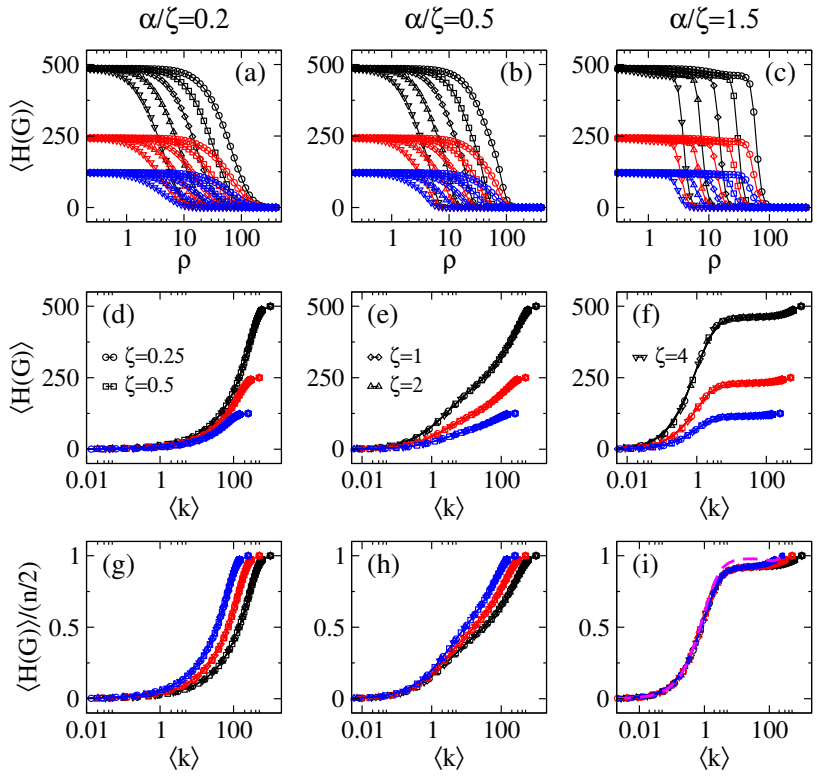

Figure 5.7: Average Harmonic index $\langle H(G)\rangle$ of hyperbolic random graphs as a function of (a-c) the disk radius ρ and (d-f) the average degree $\langle k\rangle$. (g-i) $\langle H(G)\rangle$, normalized to $n/2$, as a function of $\langle k\rangle$. The HRGs are characterized by the ratios $\alpha/\zeta = 0.2$ (left panels), $\alpha/\zeta = 0.5$ (middle panels), and (c) $\alpha/\zeta = 1.5$ (right panels). Each panel displays curves for five values of the curvature $K = -\zeta^2$ (different symbols) for each of three graph sizes: $n = 250$ (blue), $n = 500$ (red) and $n = 1000$ (black). Each data value was computed from an ensemble of $10^6/n$ graphs. Magenta dashed line in panel (i) corresponds to RGGs in the unit square with $n = 250$. Figure and description taken from [153].

panel includes curves for five values of the curvature $K = -\zeta^2$ (different symbols) for each of three graph sizes n (different colors). Also, from Figs. 5.6 and 5.7 we can make similar observations to those made for $\langle V_x(G)\rangle$ in Fig. 5.4 (i) The curves $\langle R(G)\rangle$ vs. ρ and $\langle H(G)\rangle$ vs. ρ show a crossover from full graphs, $\langle R(G)\rangle = \langle H(G)\rangle = n/2$ when $\rho \to 0$, to isolated vertices, $\langle R(G)\rangle = \langle H(G)\rangle = 0$ for $\rho \gg 1$; see Figs. 5.6(a-c) and 5.7(a-c). (ii) The curves $\langle R(G)\rangle$ vs. $\langle k\rangle$ and $\langle H(G)\rangle$ vs. $\langle k\rangle$ for different values of K collapse on top of a single curve; see Figs. 5.6(d-f) and 5.7(d-f). (iii) The curves $\langle R(G)\rangle/(n/2)$ vs. $\langle k\rangle$ and $\langle H(G)\rangle/(n/2)$ vs. $\langle k\rangle$ collapse on top of a single universal curve for $\alpha/\zeta > 0.5$ only; see Figs. 5.6(g-i) and 5.7(g-i). We understand the lack of scaling of $\langle R(G)\rangle/(n/2)$ and $\langle H(G)\rangle/(n/2)$ with

$\langle k \rangle$ as a consequence of the lack of self-averaging of k, mainly for $\alpha/\zeta \leq 0.5$, as reported in Fig. 5.3; a situation also observed in dRGGs [30]. Moreover, in Figs. 5.6(i) and 5.7(i) we also plot $\langle R(G) \rangle/(n/2)$ and $\langle H(G) \rangle/(n/2)$ for the RGGs in the unit square (see Fig. 4.1) and observe a perfect correspondence with the curves for HRGs before saturation, since the curves for RGGs saturate at smaller values of $\langle k \rangle$.

Finally, we compute the clustering measures of Eqs. (2.18)-(2.20) and Eqs. (2.21)-(2.22). Therefore, in Fig. 5.8 we present the average Watts-Strogatz clustering coefficient $\langle \overline{C} \rangle$ (upper panels) and the average global clustering coefficient $\langle C_g \rangle$ (lower panels) of HRGs as a function of the average degree $\langle k \rangle$. As for the topological indices reported above, here each panel of Fig. 5.8 includes curves for five values of the curvature $K = -\zeta^2$ (different symbols) for each of three graph sizes n (different colors). Also, we consider HRGs characterized by $\alpha/\zeta = 0.2$ (left panels), $\alpha/\zeta = 0.5$ (middle panels), and (c) $\alpha/\zeta = 1.5$ (right panels). We observe two main differences between the curves of $\langle \overline{C} \rangle$ and $\langle C_g \rangle$ as a function of $\langle k \rangle$: First, while $\langle C_g \rangle$ is a monotonically increasing function of $\langle k \rangle$ for $\alpha/\zeta \geq 0.5$, $\langle \overline{C} \rangle$ is not. Second, while $\langle k \rangle$ scales $\langle \overline{C} \rangle$ (i.e. curves for different curvatures and graph sizes fall one on top of the other), it does not scale $\langle C_g \rangle$ (even though the scaling is good for a fixed graph size). Moreover, for $\alpha/\zeta < 0.5$, monotonicity of $\langle C_g \rangle$ is only present at small graph sizes (see panel (d)) due to the appearance of a crest and a valley (local extrema) for larger sizes (see red and black curves). For $\alpha/\zeta = 1.5$, in panel (f), we observe a rapid increase of $\langle C_g \rangle$ in the interval from $\langle k \rangle \approx 0.01$ to $\langle k \rangle \approx 1$. Then it becomes plateaued for increasing $\langle k \rangle$ and afterwards the further increase of $\langle C_g \rangle$ until reaches the value of 1. In fact, this behavior reflects the scale-free property of HRGs, since for larger β values we expect higher clustering even with relatively low average degrees; see Eq. (5.5). Moreover, the appearance of bumps in panels (d-e) is a signature of transitivity phase transition due to hyperbolic proximity; that is, even though the network is still sparse (small $\langle k \rangle$), nodes begin forming small and tightly connected clusters due to their proximity in hyperbolic space, but as hubs (central nodes with high degrees) begin connecting to more peripheral nodes as $\langle k \rangle$ increases, the triangle density can be significantly reduced (due to large hyperbolic distances between their neighbors) then affecting the global clustering coefficient $\langle C_g \rangle$ growth rate as a function of $\langle k \rangle$. On the other hand, regarding the average local clustering coefficient, when $\alpha/\zeta \leq 0.5$, the curves for $\langle \overline{C} \rangle$ exhibit a peak at $\langle k \rangle \approx 40$ for $\alpha/\zeta = 0.2$ and at $\langle k \rangle \approx 30$ for $\alpha/\zeta = 0.5$. We observe that this peak is flattened when $\alpha/\zeta = 0.5$ and disappears for $\alpha/\zeta = 1.5$ ($\beta = 4$). Indeed, since $\langle \overline{C} \rangle = \sum_k P(k)C(k)$, the peaks show the contribution of the graph size on

$C(k)$ when $\beta < 2.5$ in accordance with [159]. Explicitly, when $k > \sqrt{n}$ and $\beta < 2.5$ the local clustering in terms of the degree is given as $C(k) \propto k^{2\beta-6}n^{5-2\beta}$ [159], then leaving us with a size contribution of $\sim n^{2.2}$ for $\beta = 1.4$ ($\alpha/\zeta = 0.2$) and $\sim n$ for $\beta = 2$ ($\alpha/\zeta = 0.5$). Consequently, as the average degree $\langle k \rangle > \sqrt{n}$ bumps of the $\langle \overline{C} \rangle$ are expected to appear.

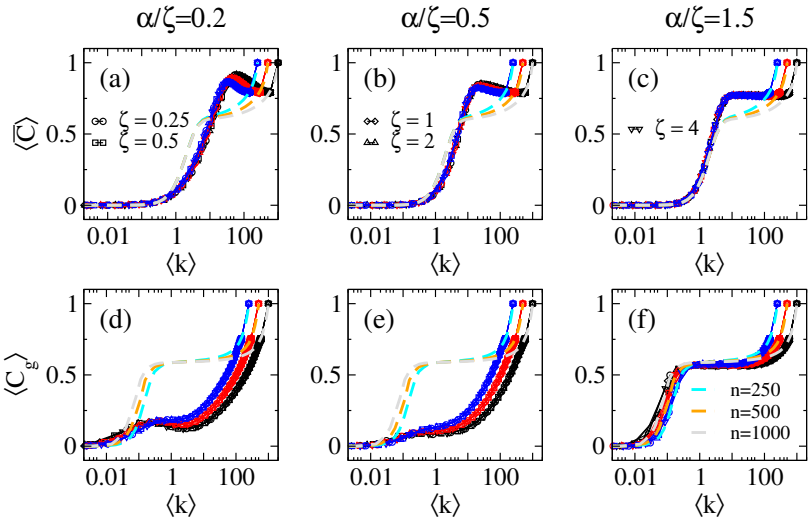

Figure 5.8: (a-c) Average Watts-Strogatz clustering coefficient $\langle \overline{C} \rangle$ and (d-f) Average global clustering coefficient $\langle C_g \rangle$ of hyperbolic random graphs as a function of the average degree $\langle k \rangle$. The HRGs are characterized by the ratios $\alpha/\zeta = 0.2$ (left panels), $\alpha/\zeta = 0.5$ (middle panels), and (c) $\alpha/\zeta = 1.5$ (right panels). Each panel displays curves for five values of the curvature $K = -\zeta^2$ (different symbols) for each of three graph sizes: $n = 250$ (blue), $n = 500$ (red) and $n = 1000$ (black). Dashed lines in panels (a-c) [(d-f)] are $\langle \overline{C} \rangle$ [$\langle C_g \rangle$] of RGGs in the unit square with $n = 250$ (cyan), $n = 500$ (orange), and $n = 1000$ (gray). Each data value was computed from an ensemble of $10^6/n$ graphs. Figure and description taken from [153].

Additionally, for comparison purposes, in Fig. 5.8 we include (as dashed lines) $\langle \overline{C} \rangle$ and $\langle C_g \rangle$ of RGGs in the unit square with $n = 250$ (cyan), $n = 500$ (orange), and $n = 1000$ (gray). As expected, we observe the convergence of the properties of HRGs to those of RGGs when increasing the ratio α/ζ. Moreover, notice the large difference of the average global clustering coefficients of both network models, mainly for $0.1 < \langle k \rangle < 10$ when the HRGs are characterized by $\alpha/\zeta \leq 0.5$, meaning that the heterogeneous topology of the HRG creates high-degree nodes with hubs that dominate the degree distribution leading to lower average global clustering compared to the RGG; which has an homogeneous degree distribution.

5.3 Spectral properties

To characterize the spectral properties of the HRG model we apply a RMT approach, see e.g. [30,58,118,149,158]. Accordingly, we use the randomly-weighted version of the adjacency matrix, defined as Eq. (3.1). With this definition, diagonal random matrices (PE [125]) are obtained for $\rho \gg 1$, when the graphs consist of disconnected vertices; whereas the GOE (i.e. full real and symmetric random matrices [125]) is recovered for $\rho \to 0$, when the graphs are complete. Thus, the ensemble defined by the randomly-weighted adjacency matrices $\mathbf{A_O}$ corresponds to a diluted GOE. Then, we use standard RMT measures to characterize the eigenvalue and eigenvector properties of $\mathbf{A_O}$. Therefore, as mentioned in Chapter 3, all RMT measures will transit from their corresponding PE values to their GOE values as ρ increases.

For the computation of spectral measures of HRGs, we perform exact numerical diagonalization to obtain the eigenvalues λ_i and normalized eigenvectors Ψ^i $(i = 1, \ldots, n)$ of large ensembles of randomly-weighted adjacency matrices $\mathbf{A_O}$ characterized by the parameter set (n, ρ, α, ζ).

In Figs. 5.9(a-c)-5.12(a-c) we present, respectively, the average ratio between consecutive eigenvalue spacings $\langle r_{\mathbb{R}}(G)\rangle$ (from Eq. 3.4), the average ratio between nearest- and next-to-nearest-neighbor eigenvalue distances $\langle r_{\mathbb{C}}(G)\rangle$ (from Eq. 3.5), the average inverse participation ratio $\langle \mathrm{IPR}(G)\rangle$ (from Eq. 3.6), and the average Shannon entropy $\langle S(G)\rangle$ (from Eq. 3.7) of HRGs as a function of the hyperbolic disk radius ρ. Each panel in Figs. 5.9-5.12 includes curves for five values of the curvature $K = -\zeta^2$ (different symbols) for each of three graph sizes n (different colors); the HRGs are characterized by $\alpha/\zeta = 0.2$ (left panels), $\alpha/\zeta = 0.5$ (middle panels), and (c) $\alpha/\zeta = 1.5$ (right panels). As expected from the analysis of the structural properties of the previous section, here for each parameter combination (n, α, ζ), the curves $\langle X(G)\rangle$ vs. ρ show a crossover from full graphs, $\langle X(G)\rangle = X_{\mathrm{GOE}}$ when $\rho \to 0$, to isolated vertices, $\langle X(G)\rangle = X_{\mathrm{PE}}$ for $\rho \gg 1$. Here X represents $r_{\mathbb{R}}$, $r_{\mathbb{C}}$, IPR, and S; while X_{GOE} and X_{PE} are the RMT values of the spectral measures in the GOE and PE limits, respectively. Then, in Figs. 5.9(d-f)-5.12(d-f) we present again the curves of Figs. 5.9(a-c)-5.12(a-c) but now as a function of $\langle k\rangle$. Here we observe a reasonably good scaling of $\langle r_{\mathbb{R}}(G)\rangle$ and $\langle r_{\mathbb{C}}(G)\rangle$, while $\langle \mathrm{IPR}(G)\rangle$ and $\langle S(G)\rangle$ still show a graph size dependence. Anyway, for a fixed graph size we observe the collapse of the curves characterized by different curvatures.

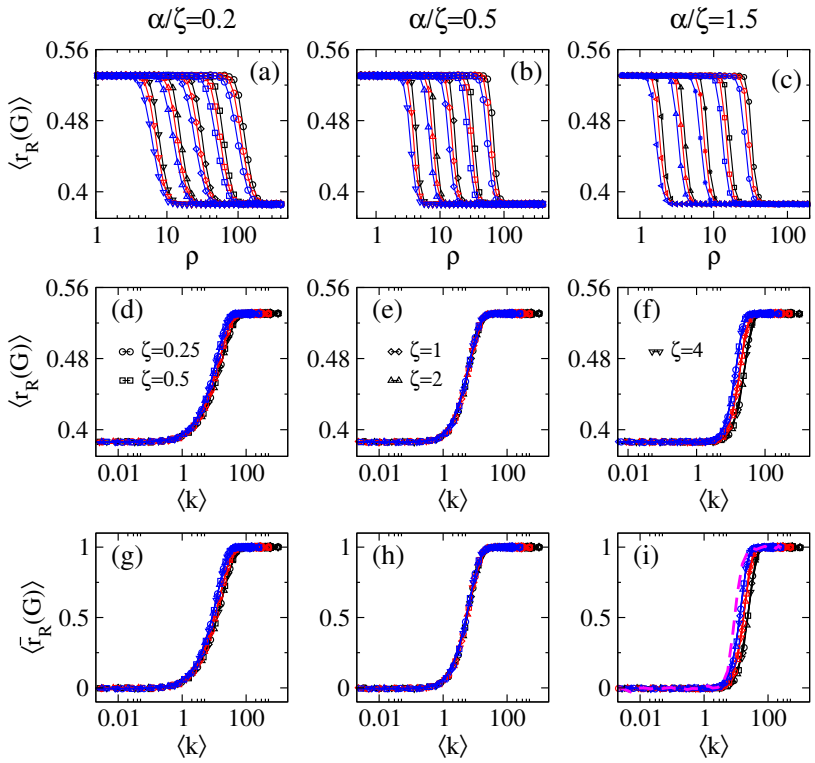

Figure 5.9: Average ratio between consecutive eigenvalue spacings $\langle r_{\mathbb{R}}(G)\rangle$ of hyperbolic random graphs as a function of (a-c) the disk radius ρ and (d-f) the average degree $\langle k\rangle$. (g-i) $\langle \overline{r}_{\mathbb{R}}(G)\rangle$, see Eq. (3.8), as a function of $\langle k\rangle$. The HRGs are characterized by the ratios $\alpha/\zeta = 0.2$ (left panels), $\alpha/\zeta = 0.5$ (middle panels), and (c) $\alpha/\zeta = 1.5$ (right panels). Each panel displays curves for five values of the curvature $K = -\zeta^2$ (different symbols) for each of three graph sizes: $n = 250$ (blue), $n = 500$ (red) and $n = 1000$ (black). Each data value was computed from an ensemble of $10^6/n$ graphs. Magenta dashed line in panel (i) corresponds to RGGs in the unit square with $n = 250$. Figure and description taken from [153].

To ease the comparison of the spectral measures we conveniently normalize them according to Eqs. (3.8)-(3.11). Therefore, in Figs. 5.9(g-i)-5.12(g-i) we show the normalized spectral measures in terms of the average degree $\langle k\rangle$. From these figures we can see that $\langle k\rangle$ serves as the scaling parameter of $\langle \overline{r}_{\mathbb{R}}(G)\rangle$, $\langle \overline{r}_{\mathbb{C}}(G)\rangle$ and $\langle \overline{S}(G)\rangle$ for $\alpha/\zeta = 0.5$, while $\langle \overline{\mathrm{IPR}}(G)\rangle$ does not scale at all for any value of α/ζ. In fact, we have already observed that the spectral properties of models of dRGGs do not scale with $\langle k\rangle$ [30] (in Chapter 4) for all model parameter combinations, which is what we also observe here for HRGs. However, it was possible to find the scaling parameter ξ of the spectral properties of RGGs by performing a proper scaling analysis that incorporates an additional dependence of the graph size [30], i.e. $\xi \equiv \xi(\langle k\rangle, n)$. Indeed, we perform the scaling analysis of the spectral

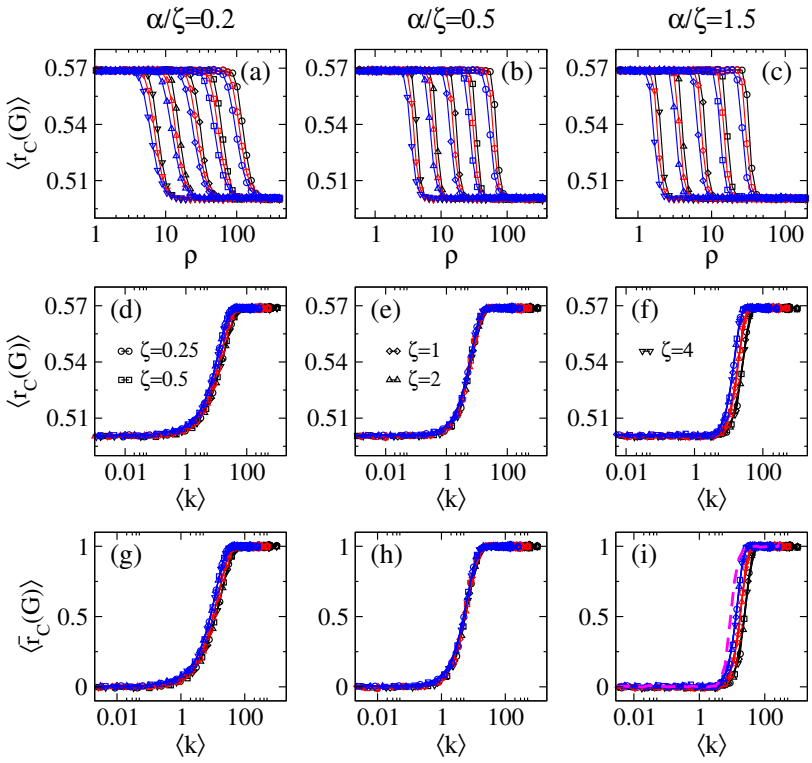

Figure 5.10: Average ratio between nearest- and next-to-nearest-neighbor eigenvalue distances $\langle r_{\mathbb{C}}(G)\rangle$ of hyperbolic random graphs as a function of (a-c) the disk radius ρ and (d-f) the average degree $\langle k\rangle$. (g-i) $\langle \overline{r}_{\mathbb{C}}(G)\rangle$, see Eq. (3.9), as a function of $\langle k\rangle$. The HRGs are characterized by the ratios $\alpha/\zeta = 0.2$ (left panels), $\alpha/\zeta = 0.5$ (middle panels), and (c) $\alpha/\zeta = 1.5$ (right panels). Each panel displays curves for five values of the curvature $K = -\zeta^2$ (different symbols) for each of three graph sizes: $n = 250$ (blue), $n = 500$ (red) and $n = 1000$ (black). Each data value was computed from an ensemble of $10^6/n$ graphs. Magenta dashed line in panel (i) corresponds to RGGs in the unit square with $n = 250$. Figure and description taken from [153].

properties of HRGs in the next section, so we properly define ξ. Also, as well as in Sec. 5.2, for comparison purposes in Figs. 5.9(i)-5.12(i) we include results for RGGs in the unit square with $n = 250$; see magenta dashed lines. As expected, we observe the convergence of the spectral properties of HRGs to those of RGGs for large α/ζ.

5.4 Scaling analysis

In Sec. 5.3 we analyzed spectral properties of HRGs. Specifically, we reported the average ratio between consecutive eigenvalue spacings $\langle r_{\mathbb{R}}(G)\rangle$, the average ratio between

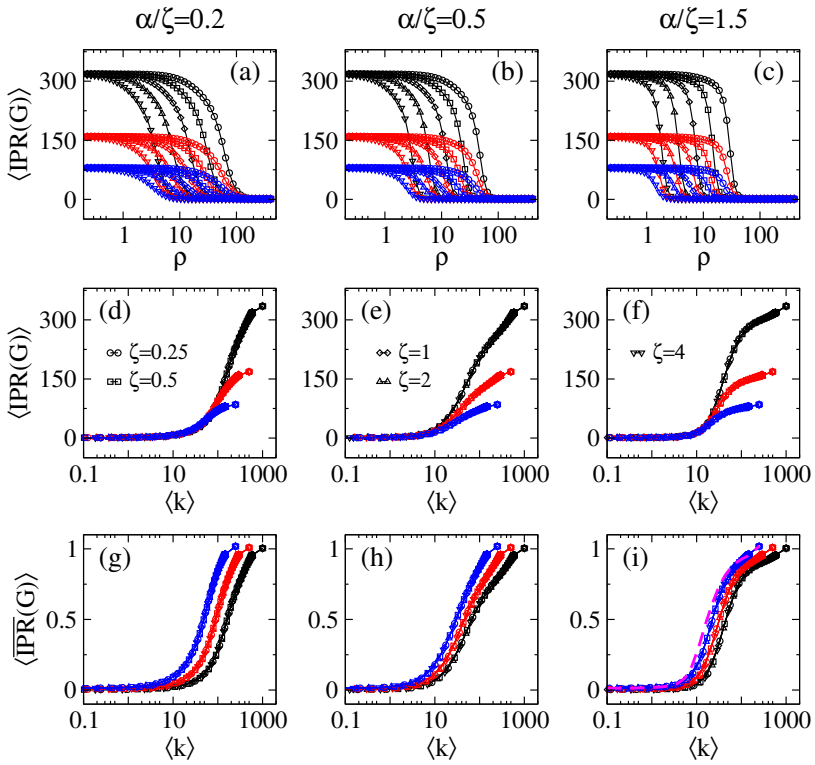

Figure 5.11: Average inverse participation ratio $\langle \mathrm{IPR}(G) \rangle$ of hyperbolic random graphs as a function of (a-c) the disk radius ρ and (d-f) the average degree $\langle k \rangle$. (g-i) $\langle \overline{\mathrm{IPR}}(G) \rangle$, see Eq. (3.10), as a function of $\langle k \rangle$. The HRGs are characterized by the ratios $\alpha/\zeta = 0.2$ (left panels), $\alpha/\zeta = 0.5$ (middle panels), and (c) $\alpha/\zeta = 1.5$ (right panels). Each panel displays curves for five values of the curvature $K = -\zeta^2$ (different symbols) for each of three graph sizes: $n = 250$ (blue), $n = 500$ (red) and $n = 1000$ (black). Each data value was computed from an ensemble of $10^6/n$ graphs. Magenta dashed line in panel (i) corresponds to RGGs in the unit square with $n = 250$. Figure and description taken from [153].

consecutive nearest- and next-to-nearest-neighbor eigenvalue distances $\langle r_{\mathbb{C}}(G) \rangle$, the average inverse participation ratio $\langle \mathrm{IPR}(G) \rangle$, and the average Shannon entropy $\langle S(G) \rangle$, see Figs. 5.9-5.12.

Furthermore, we found that curves $\langle \overline{X}(G) \rangle$ vs. $\langle k \rangle$ (where X represents $r_{\mathbb{R}}$, $r_{\mathbb{C}}$, IPR, and S), characterized by the same graph size n and ratio α/ζ, fall one on top of the other; that is, the curves $\langle \overline{X}(G) \rangle$ scale with $\langle k \rangle$. However, as n decreases, the arrays of scaled curves are displaced to the left on the $\langle k \rangle$-axis. This last observation indicates the additional dependence of the curves $\langle \overline{X}(G) \rangle$ vs. $\langle k \rangle$ on n and the possible existence of a true scaling parameter $\xi \equiv \xi(\langle k \rangle, n)$. Therefore, a scaling analysis of $\langle \overline{X}(G) \rangle$ seems pertinent. Again, as in the scaling analysis of dRGGs in Chapter 4, we try to find a parameter ξ such

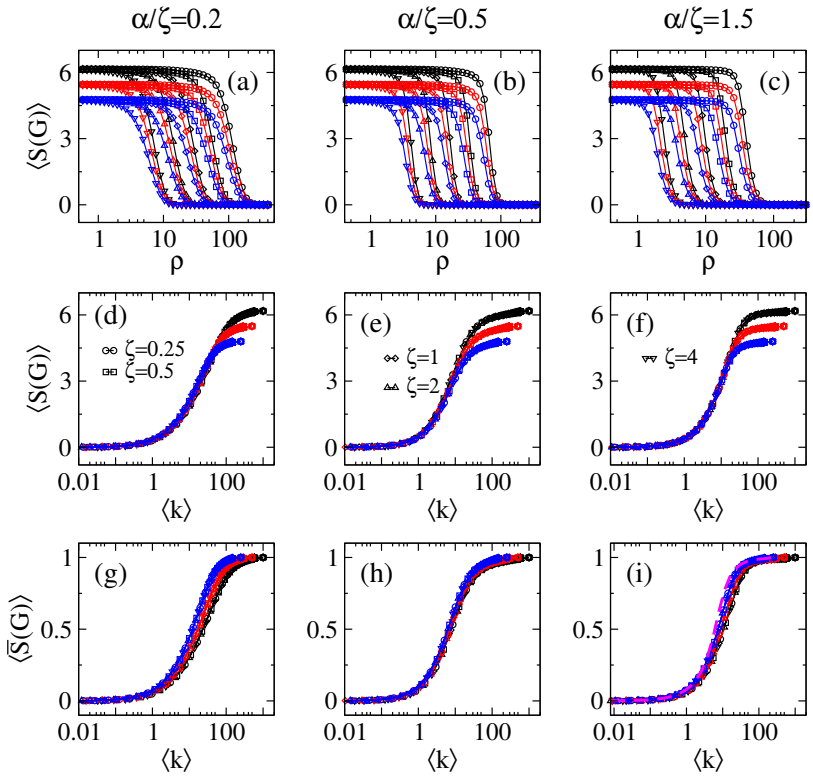

Figure 5.12: Average Shannon entropy $\langle S(G)\rangle$ of hyperbolic random graphs as a function of (a-c) the disk radius ρ and (d-f) the average degree $\langle k\rangle$. (g-i) $\langle \overline{S}(G)\rangle$, see Eq. (3.11), as a function of $\langle k\rangle$. The HRGs are characterized by the ratios $\alpha/\zeta = 0.2$ (left panels), $\alpha/\zeta = 0.5$ (middle panels), and (c) $\alpha/\zeta = 1.5$ (right panels). Each panel displays curves for five values of the curvature $K = -\zeta^2$ (different symbols) for each of three graph sizes: $n = 250$ (blue), $n = 500$ (red) and $n = 1000$ (black). Each data value was computed from an ensemble of $10^6/n$ graphs. Magenta dashed line in panel (i) corresponds to RGGs in the unit square with $n = 250$. Figure and description taken from [153].

that the curves $\langle \overline{X}(G)\rangle$ vs. ξ are *universal* curves, i.e; invariant curves as a function of ξ.

First, we note that all curves $\langle \overline{X}(G)\rangle$ vs. $\langle k\rangle$ show a transition from approximately 0, when $\langle k\rangle \ll 1$, to 1, when $\langle k\rangle \gg 1$, (see Figs. 5.9-5.12) but they are displaced along the $\langle k\rangle$–axis for different values of n. Then, we characterize the position of the curves $\langle \overline{X}(G)\rangle$ vs. $\langle k\rangle$ along the $\langle k\rangle$–axis by the values of $\langle k\rangle$ for which $\langle \overline{X}(G)\rangle \approx 0.5$. We label the values of $\langle k\rangle$ at half of the full transition as $\langle k\rangle^*$. We observe in Fig. 5.15 a linear trend of the data sets (in log-log scale) $\langle k\rangle^*$ vs. n suggesting a power-law behavior of the form

$$\langle k\rangle^* = Cn^{\delta}. \tag{5.9}$$

	$\langle \overline{r}_{\mathbb{R}}(G) \rangle$		$\langle \overline{r}_{\mathbb{C}}(G) \rangle$		$\langle \overline{\mathrm{IPR}}(G) \rangle$		$\langle \overline{S}(G) \rangle$	
α/ζ	C	δ	C	δ	C	δ	C	δ
0.2	1.8	0.277	1.521	0.304	0.362	0.883	0.92	0.462
0.5	4.889	0.013	3.332	0.07	1.02	0.613	2.821	0.146
1.5	1.271	0.418	1.09	0.449	1.424	0.502	1.822	0.254

Table 5.1: Values of the fitting parameters C and δ in Eq. (5.9) as extracted from the curves of $\langle k \rangle^*$ vs. n for the normalized quantities $\langle \overline{r}_{\mathbb{R}}(G) \rangle$, $\langle \overline{r}_{\mathbb{C}}(G) \rangle$, $\langle \overline{\mathrm{IPR}}(G) \rangle$, and $\langle \overline{S}(G) \rangle$.

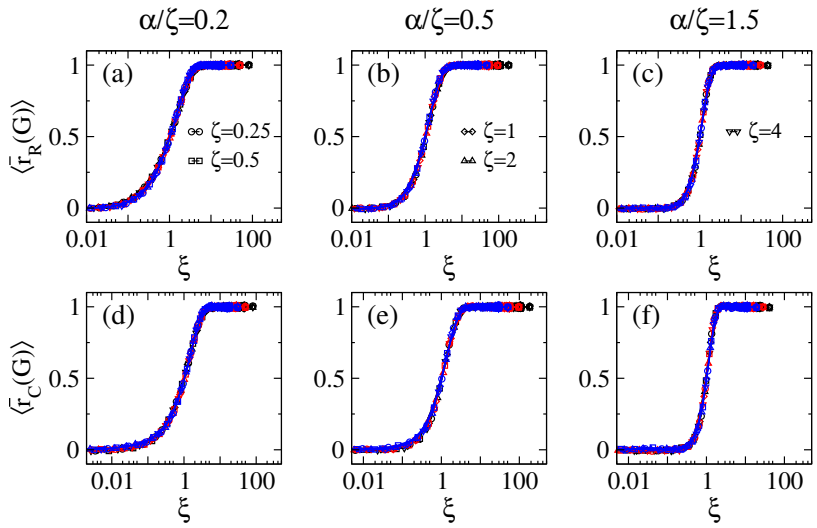

Figure 5.13: (a-c) Normalized average ratio between consecutive eigenvalue spacings $\langle \overline{r}_{\mathbb{R}}(G) \rangle$ and (d-f) normalized average ratio between nearest- and next-to-nearest-neighbor eigenvalue distances $\langle \overline{r}_{\mathbb{C}}(G) \rangle$ of hyperbolic random graphs as a function of the scaling parameter ξ. The HRGs are characterized by the ratios $\alpha/\zeta = 0.2$ (left panels), $\alpha/\zeta = 0.5$ (middle panels), and (c) $\alpha/\zeta = 1.5$ (right panels). Each panel displays curves for five values of the curvature $K = -\zeta^2$ (different symbols) for each of three graph sizes: $n = 250$ (blue), $n = 500$ (red) and $n = 1000$ (black). Each data value was computed from an ensemble of $10^6/n$ graphs. Figure and description taken from [153].

Thus we define the scaling parameter as the ratio between $\langle k \rangle$ and $\langle k \rangle^*$:

$$\xi \equiv \frac{\langle k \rangle}{\langle k \rangle^*} = \frac{\langle k \rangle}{C n^{\delta}} \propto n^{-\delta} \langle k \rangle. \tag{5.10}$$

Therefore, by plotting again the curves of $\langle \overline{X}(G) \rangle$ now as a function of ξ we observe that curves for different graph sizes n collapse on top of universal curves; see Fig. 5.13 for the spectral measures and Fig. 5.14 for the eigenvector measures of HRGs. This means that

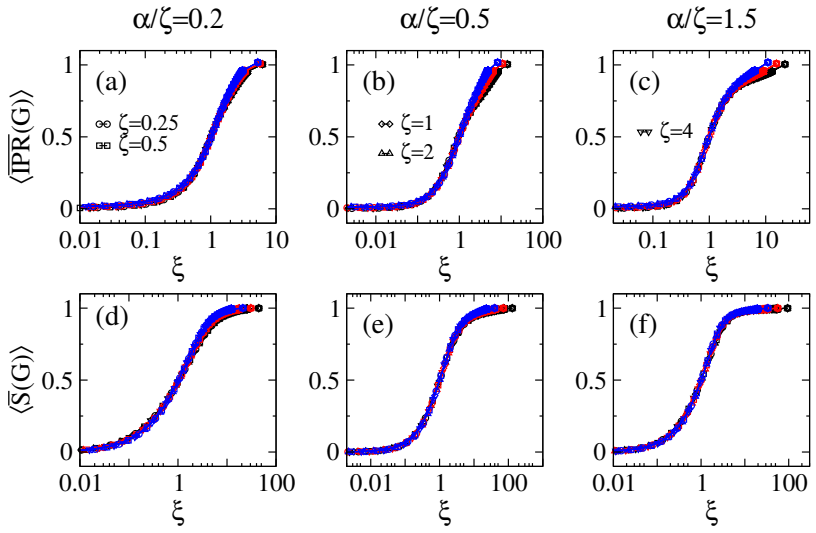

Figure 5.14: (a-c) Normalized average inverse participation ratio $\langle \overline{\mathrm{IPR}}(G) \rangle$ and (d-f) normalized average Shannon entropy $\langle \overline{S}(G) \rangle$ of hyperbolic random graphs as a function of the scaling parameter ξ. The HRGs are characterized by the ratios $\alpha/\zeta = 0.2$ (left panels), $\alpha/\zeta = 0.5$ (middle panels), and (c) $\alpha/\zeta = 1.5$ (right panels). Each panel displays curves for five values of the curvature $K = -\zeta^2$ (different symbols) for each of three graph sizes: $n = 250$ (blue), $n = 500$ (red) and $n = 1000$ (black). Each data value was computed from an ensemble of $10^6/n$ graphs. Figure and description taken from [153].

for a given setup of HRGs, once the value of the scaling parameter is computed, one may predict the spectral properties of the HRGs without actually computing them by looking at the scaled universal curves. Moreover, the scaling parameter of $\langle S(G) \rangle$ allows for the definition of the localization regimes: For $\xi \leq 0.1$ [$\xi \geq 10$], the eigenvectors of the HRGs are in a localized [extended] regime, while the transition from localized to extended eigenvectors occurs for $0.1 < \xi < 10$.

In addition, it is useful to look at the values of the exponent δ of Eq. (5.9) obtained from the fittings of the curves $\langle k \rangle^*$ vs. n, which are reported in Table 5.1. From Table 5.1, since $\delta \approx 0$ for $\langle \overline{r}_{\mathbb{R}}(G) \rangle$ and $\langle \overline{r}_{\mathbb{C}}(G) \rangle$ for $\alpha/\zeta = 0.5$, we can claim that $\langle k \rangle$ is indeed the scaling parameter of $\langle \overline{r}_{\mathbb{R}}(G) \rangle$ and $\langle \overline{r}_{\mathbb{C}}(G) \rangle$; as already observed in Sec. 5.3 but quantified here by means of the scaling analysis.

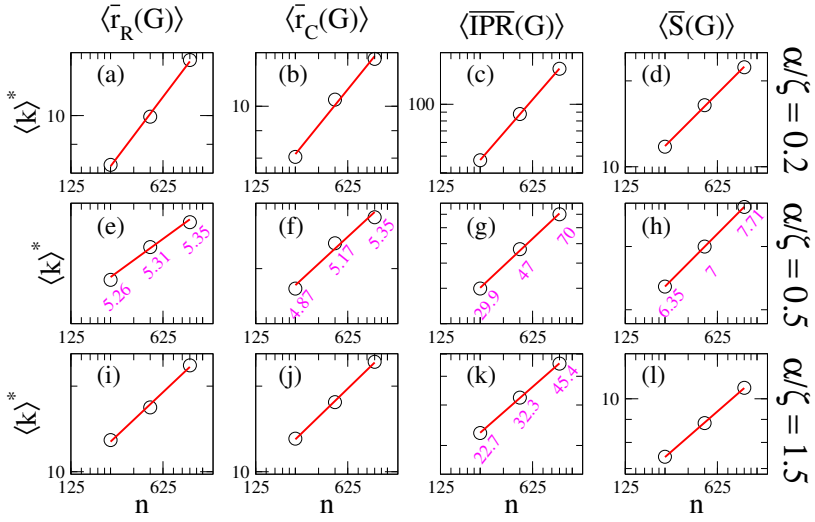

Figure 5.15: Curves $\langle k\rangle^*$ vs. n in log-log scale for the (a, e, i) normalized average ratio between consecutive eigenvalue spacings $\langle \overline{r}_{\mathbb{R}}(G)\rangle$, (b, f, j) normalized average ratio between nearest- and next to-nearest-neighbor eigenvalue distances $\langle \overline{r}_{\mathbb{C}}(G)\rangle$, (c, g, k) normalized average inverse participation ratio $\langle \overline{\mathrm{IPR}}(G)\rangle$, and (d, h, l) normalized average Shannon entropy $\langle \overline{S}(G)\rangle$ of the hyperbolic random graph. We show the three different ratio configurations $\alpha/\zeta = 0.2$ (top row), $\alpha/\zeta = 0.5$ (middle row), and $\alpha/\zeta = 1.5$ (bottom row). In every panel the red line is the best fit to the data as Eq. (5.9). The fiting values are reported in Table 5.1. In some panels the data values are shown to help visualize the scale.

Part II

Survival probability in random network models

Chapter 6

Survival probability in random network models

In this Chapter we study the survival probability of an initial state of the ER network model represented by the orthogonal randomly weighted adjacency matrix $\mathbf{A_O}$ in the context of its full random matrix ensemble (GOE) formulation. We introduce the construction of the random network model, and describe the behaviour of the survival probability of the ER model in terms of its inherent parameters. We show that the relative depth of the correlation hole of the survival probability can be scaled with the average degree $\langle k \rangle$, and that the survival probability can be well characterized at different time scales by fixing the average degree $\langle k \rangle$ with varying network sizes n. Furthermore, we show that the generalized fractal dimensions of the inverse participation ratio describe the decay of the time-averaged survival probability.

6.1 Survival probability in the GOE

The survival probability (SP), also known as return probability, measures the probability of finding a system in its initial state at a later time t. Assuming an initial state $|\Psi(t=0)\rangle$ and its time-evolved counterpart $|\Psi(t)\rangle$, the SP is the squared inner product of both states. In the context of RMT, for full random matrix ensembles (FRME) we assume the existence of a basis of states $|\phi_k\rangle$ used to construct every FRME. In this sense, we can define an initial state $|\phi_{ini}\rangle \equiv |\Psi(0)\rangle$ at the bulk of the spectrum, $ini = n/2$ [161], with n

the size of the matrix. Then the SP is defined as,

$$SP(t) = |\langle\Psi(0)|\,|\Psi(t)\rangle|^2 = \left|\sum_\beta \left|C_{ini}^\beta\right|^2 e^{-iE_\beta t}\right|^2 \tag{6.1}$$

$$= \left|\int \rho(E) e^{-iE_\beta t} dE\right|^2,$$

$$\rho(E) = \sum_\beta \left|C_{ini}^\beta\right|^2 \delta(E - E_\beta) \tag{6.2}$$

where E_β are the eigenvalues of the ensemble, $\left|C_{ini}^\beta\right|^2$ are the components of the evolved initial state on the basis, and $\rho(E)$ corresponds to the energy distribution of the initial state, also known as the local density of states (LDOS). The focus on an initial state at the bulk of the spectrum is derived from the fact that most eigenstates are concentrated at the bulk according to Wigner's simicircle law. On this basis, the dynamics of such a state is therefore representative of the typical behavior in the system. In particular, in quantum chaotic systems, the bulk captures the ergodic and delocalized nature of eigenstates, and helps studies on many-body quantum thermalization [160, 161]

Now, since the SP and LDOS are related by a Fourier transform, the SP can be analytically derived once the LDOS shape is determined. For the GOE, the shape of the LDOS follows the Wigner semicircle law,

$$\rho(E) = \frac{1}{\pi\sigma_{ini}}\sqrt{1 - \left(\frac{E}{2\sigma_{ini}}\right)}, \tag{6.3}$$

where σ_{ini}^2 [161] is the variance of the energy distribution of the initial state. The variance σ_{ini}^2 is given as,

$${\sigma_{ini}}^2 = \sum_\beta \left|C_{ini}^\beta\right|^2 \left(E_\beta - \sum_\beta \left|C_{ini}^\beta\right|^2 E_\beta\right)^2, \tag{6.4}$$

with E_β as the eigenenergies of the FRM. In Fig. 6.1 we plot the local density of states for a FRME with size $n = 1000$ following the Wigner's semicircle law with a spectral width $E \sim (-\sigma_{ini}, \sigma_{ini})$.

Then the analytical expression for the average SP [162] derived from the semicircle shape of the LDOS is given by

$$\langle SP(t)\rangle = \frac{1 - \langle\overline{SP}\rangle}{n-1}\left[n\frac{\mathcal{J}_1^2(2\sigma t)}{(\sigma t)^2} - b_2\left(\frac{\sigma t}{2n}\right)\right] + \langle\overline{SP}\rangle. \tag{6.5}$$

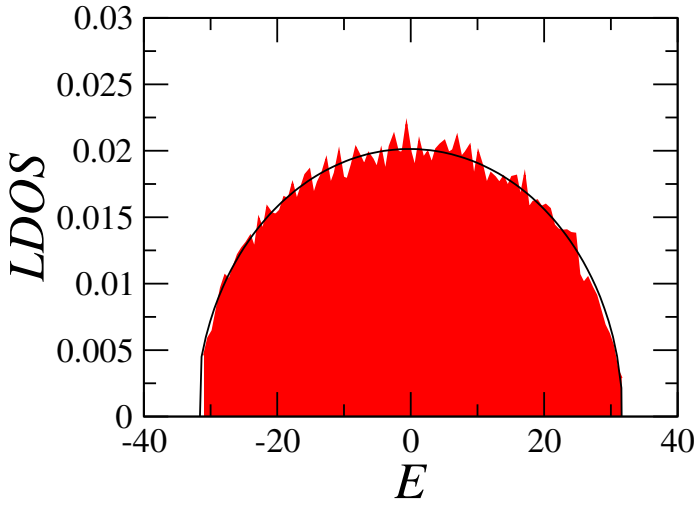

Figure 6.1: Local density of states (LDOS) of the initial state $|\phi_{ini}\rangle$ for a GOE matrix with size $n = 1000$. The Wigner semicircle law of Eq. (6.3) corresponds to the black line.

Where $\mathcal{J}_1$ is a Bessel function of the first kind, the term $[\mathcal{J}_1(2\sigma_{ini}t)/(\sigma_{ini}t)]^2$ corresponds to the Fourier transform of Eq. (6.3), and $b_2(t)$ corresponds to the two-level form factor that predominates on the ramp (correlation hole) until saturation $\langle\overline{SP}\rangle$. This expression predicts slow decaying oscillations of the probability at short times as t^{-3} and a well defined Thouless time $t_{Th} = (3/\pi)^{1/4}$ [163–165]. As indicated in Fig. 6.2 the Thouless time is the time for the survival probability to reach the bottom of the correlation hole. In the context of electrons in disordered systems and localization theory, the Thouless time indicates the characteristic time it takes for an electron to diffuse across a finite disordered system, thus determining its time scale. Regarding RMT, this time marks the time scale at which eigenvalues transition from being uncorrelated (PE) to fully correlated (FRME).

Hence, following this formalism, we study the SP of ER networks using as a reference the diluted GOE presented in Chapter 3, the $\mathbf{A_O}$ randomly-weighted adjacency matrix representation.

6.2 Erdös Renyi network

The Erdös-Renyi (ER) random network model, introduced in 1951 [4] by Solomonoff and Rapoport and later named after Paul Erdös and Alfréd Renyi [5], is generated by independently connecting n separate vertices or nodes with a connection probability of p

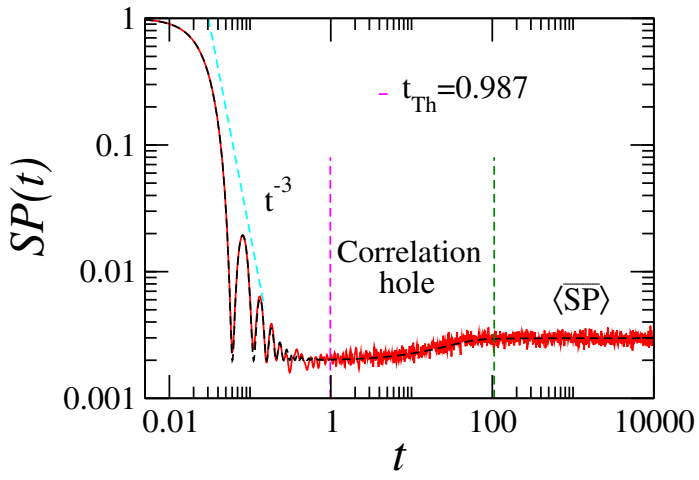

Figure 6.2: Survival probability of a FRME with size $n = 1000$ in red line. Black dashed line indicates the analytical prediction of Eq. (6.5). The slow decay of the SP is indicated in the cyan dashed line as t^{-3}. The correlation hole (ramp) is indicated between magenta and green dashed lines. The Thouless time t_{Th} is depicted with the magenta line. The saturation value $\langle\overline{\mathrm{SP}}\rangle$ is reached at large times after the end of the ramp.

through a random pairing process. This pairing process leads to a graph where the presence or absence of any specific edge is entirely uncorrelated with the others. Thus, given the random and independent nature of edge formation, the degree k of any particular node in an ER graph (network) follows a binomial distribution as it is the sum of $n-1$ independent Bernoulli trials, each with success probability p. Then, the average degree can be calculated directly from the parameters n and p of the ER model. Since each node has $n-1$ potential connections, and each connection exists with probability p, the expected degree $\langle k\rangle$ of any node is:

$$\langle k\rangle = (n-1)p \approx np. \tag{6.6}$$

Here, we can easily identify p as the connectance Ω from Eq. (6.6) and Eq. (2.14). Thus in Fig. 6.3 we observe the evolution of the edge formation as the connection probability p increases for ER networks with $n = 15$ nodes, from isolated to a complete graph. Note, that this is just a visual representation for in the practice ER is random and different p values give essentially different network realizations.

Then, as p increases, the network becomes more densely connected, which influences various properties of the network, such as the emergence of a giant component (a large cluster) and the overall robustness of the network. Moreover, due to the importance of the

average degree $\langle k \rangle$ as a critical parameter that influences the overall structure of the network and connectivity, proved as a scaling parameter of structural and static spectral measures of various random network models [30, 58, 118, 149, 166], we use these two parameters to characterize the survival probability and its relevant features.

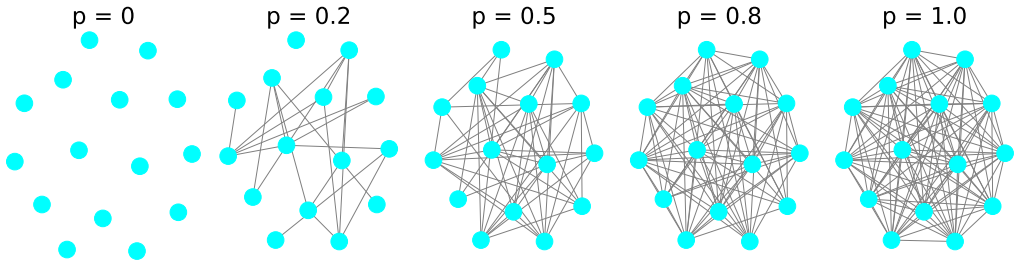

Figure 6.3: Erdös Renyi network with $n = 15$ vertices for five different values of the connection probability p.

6.3 Analysis of the survival probability

First, in Fig. 6.4 we show the local density of states (LDOS) of various configurations of size n and probability p of ER networks. In panels (b, e, h) the distributions are given for a critical value of the connection probability p, given as

$$p_c \sim (n^{2/3})/(n-1), \tag{6.7}$$

which was reported in [167] as the probability up to which, the Wigner semicircle-law of the LDOS is still expected as $n \to \infty$. Thus, panels (c, f, i) show distributions for higher probabilities, and panels (a, d, g) for lower probabilities, as multiples of p_c, to illustrate how semicircle behaviour is lost when p is lower than p_c and when size n decreases as well. As a consequence, we expect to observe GOE-like behaviour of the SP [162] for $p > p_c$. Additionally, as observed in panels (a, d, g), the LDOS shape is clearly non-universal when $p < p_c$. Thus, an analytical prediction of the SP decay can not be derived as with Eq. (6.5), and significant deviations from the GOE are expected as $p \to 0$.

Thus, to assess the general behaviour of the survival probability as the connectance p varies, in Figs. 6.5(a-c), we present the evolution of the SP for several connection probability values p for a 2×10^4 ensemble of ER networks with $n = 1000$ nodes. In panel (a) the

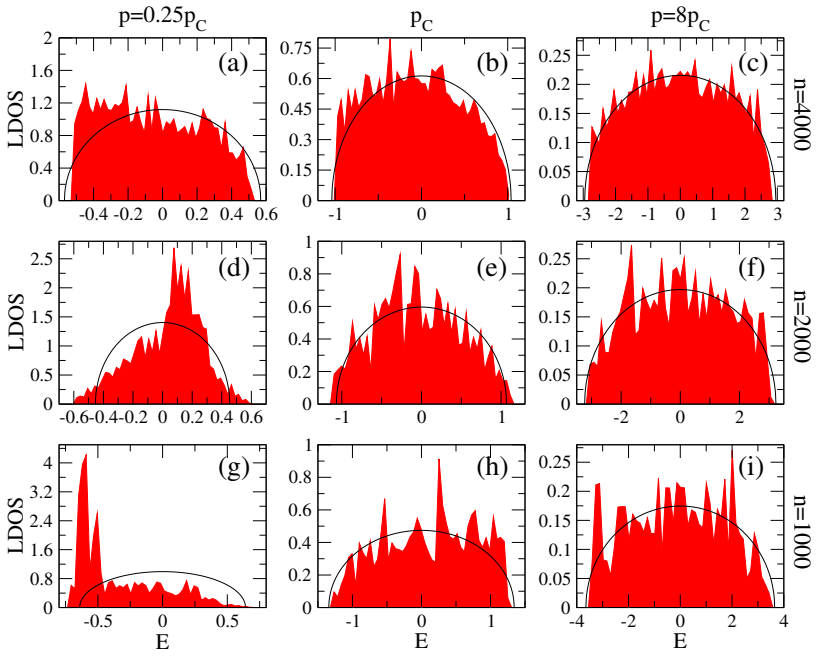

Figure 6.4: Histograms of the local density of states LDOS at the center of the bulk ϕ_{ini} of ER networks for different values of connection probability p in terms of the critical value p_c from Eq. (6.7) and different sizes (number of nodes) n. Panels (b), (e) and (h) show the histograms for the critical value p_c from Eq. (6.7). Panels (a), (c), (d), (f), (g) and (i) are given for multiples of p_c. The size of the network is given per row. Every histogram was constructed from a single realization. Black lines are semicircles (Eq. (6.3)) with σ_{ini} from Eq. (6.4) of the corresponding realization.

SP has an evident power-law decay with null oscillations as well as its saturation values are lowered as the probability p of the network increases (from top to bottom) as indicated by dashed black lines in Fig. 6.5(a) and the insets in Figs. 6.5(b) and (c). Additionally, the SP curves saturate faster as p increases. In panel (b), as p increases, minor oscillations emerge during the slow decay of the SP showing the relevance of $p \to p_c = 0.\overline{11}$ (for $n = 1000$). We also observe in the insets of Figs. 6.5(b-c) that saturation values begin to tend to the GOE prediction $3/n = 0.00\overline{33}$ as the network becomes fully connected $p \to 1$. In panel (c) we observe the oscillations of the SP increase in amplitude at early times and depict the transition into the FRME (GOE) prediction [163–165]. Also in panels (a-c) the drop (ramp) of the SP is rendered as a correlation hole since the localization-to-delocalization transition of the ER model has been reported around $\langle k \rangle \geq 4$ [58, 64, 65, 67, 171].

Additionally, as we dilute the network ($p \to 0$, $\langle k \rangle \to 0$), the correlation hole

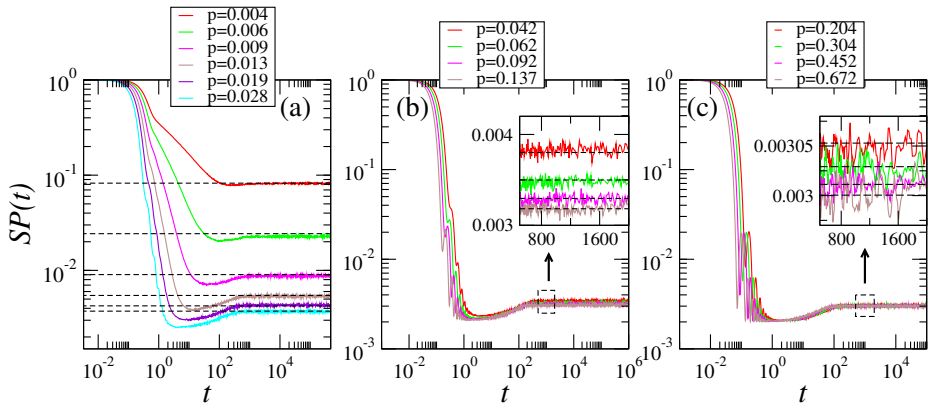

Figure 6.5: (a-c) Survival probability $SP(t)$ of the ER network with size $n = 1000$ for several values of probability p. (d) Inverse participation ratio of the initial state IPR_{ini} over $3/n$ (GOE saturation value) as a function of the probability of connection p, and (e) as a function of the average degree for three network sizes. Insets in panels (b and c) offer an amplification of the marked black dashed squares below. Horizontal dashed black lines indicate the saturation value of the curves. In panels (a-c) the probability of connection p increases from top to bottom. Colored dashed lines in panels (d-e) correspond to fittings of Eq. (6.14) to the data; see Table 6.1.

vanishes according to the localization-to-delocalization transition $\langle k \rangle$ value, and after its disappearance the minimum of the SP is recovered around the t_{Th} of the GOE [162] (not shown here), $t_{Th}^{GOE} = (3/\pi)^{1/4} \approx 1$, indicating the end of the quasi-diffusive behavior of the network and the onset to localization.

6.3.1 Initial fast decay

The initial fast decay of the SP is governed by the Fourier transform of the LDOS. However, in the case of ER networks, the LDOS becomes non-universal as $p \to 0$ ($p < p_c$); see Fig. 6.4. Nevertheless, the dominant first term in the approximation of the inner product $|\langle \Psi(0)|\,|\Psi(t)\rangle|^2$ determines the very initial decay of the SP, which is given by

$$S(t << 1) \approx 1 - \sigma_{ini}^2 t^2. \tag{6.8}$$

Then, in order to characterize the standard deviation σ_{ini} in terms of the connection probability p, in Fig. 6.6(g), we plot the standard deviation of the energy distribution of the initial state σ_{ini} given by Eq. (6.4) for various values of the probability of connection p. Here, we find that the σ_{ini} vs. p curve follows a power-law fit $\sigma_{ini} = Ap^B$ with fitting values $A = 31.68175 \approx n^{1/2}$ and $B = 0.5006$. This shows that the variance of the initial state σ_{ini}^2

is directly related to the average degree $\langle k \rangle$, for now $\sigma_{ini} \approx \sqrt{np} \approx \langle k \rangle^{1/2}$; see Eq. (6.6). Thus, in panels (a-h) in Fig. 6.6, we plot (in green lines) the initial fast decay of the SP, now given by

$$SP(t << 1) \approx 1 - \langle k \rangle t^2, \tag{6.9}$$

and observe a good correspondence with the SP curves across different values of $\langle k \rangle$.

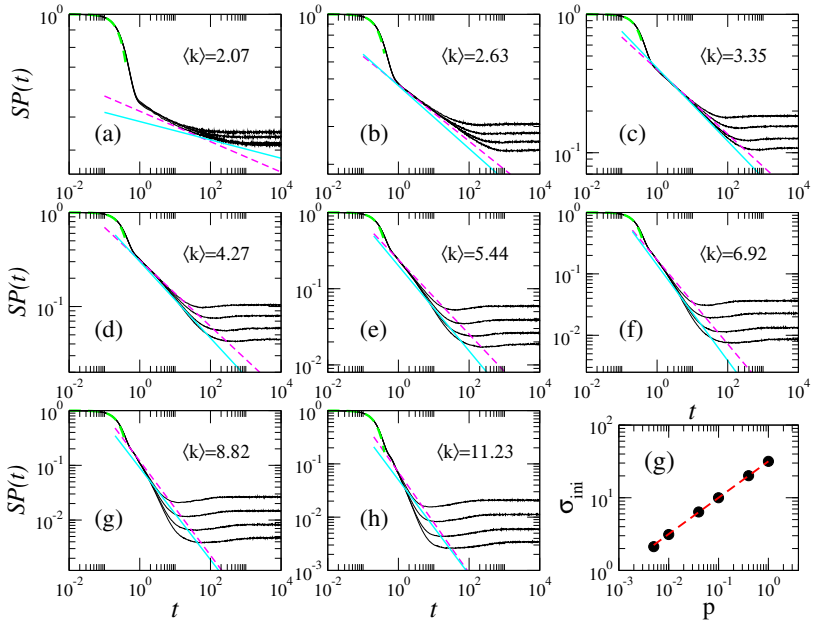

Figure 6.6: (a-h) Survival probability of ER networks for several fixed values of the average degree $\langle k \rangle$. Graph sizes increase from top to bottom ($n = 250, 500, 1000, 2000$). Magenta dashed lines depict t^{-D_2}, where $D_2 = 0.0446$(a), 0.1316(b), 0.234(c), 0.3509(d), 0.4885(e), 0.6868(f), 0.8615(g), and 0.9477(h). Cyan solid lines depict $t^{-\widetilde{D}_2}$, where $\widetilde{D}_2 = 0.0269$(a), 0.1467(b), 0.2647(c), 0.4062(d), 0.5589(e), 0.7786(f), 0.8398(g), and 0.8873(h). Green dashed lines show the decay at very short times of the survival probability as given by Eq. (6.9). (g) Standard deviation of the energy distribution of the initial state σ_{ini} (Eq. (6.4)) as a function of the connection probability p for ER with $n = 1000$. The red dashed line is a fit of the form $y = Ax^B$, with $A = 31.68175$ and $B = 0.5006$. The values of D_2 and $\widetilde{D}_2$ were computed as described in Appendix A.

6.3.2 Slow decay

Since the time evolution of wave functions is directly related to the transport properties of a conducting-insulator system at criticality, at the mobility edge, some studies have focused on its description through the analysis of the correlation dimension D_2; see

Appendix A for the definition of D_2. The analysis of the correlation dimension D_2 has become relevant as the diffusion constant of quantum Hall systems was found related to D_2 [169]. This led to the study of the return probability (or survival probability) of non-interacting electrons in a two-dimensional disordered system under a magnetic field, showing that its slow decay is a power-law with exponent $D_2/2$ [169]. Later, Huckestein and Klesse showed that at the mobility edge, in disordered non-interacting electron systems in two and three dimensions, the survival probability has a slow power-law decay D_2/d, where d is the dimension of the system [180]; also proving that the generalized dimension of the initial state $\widetilde{D}_2$ is related to D_2 as $D_2/d \approx \widetilde{D}_2$ further confirming the findings of [169]. In particular, these critical states have shown multifractal properties, such as in the case of Anderson metal-insulator transition in two and three dimensions, described by the generalized dimensions D_q [176]. The existence of multifractal eigenstates means that eigenstates are neither fully extended nor fully localized causing long-time correlations in the quantum dynamics, leading to a power law decay of the survival probability as explored in [181,182]. Therefore, as the power-law decay of the survival probability has been related to the generalized dimensions D_2 and $\widetilde{D}_2$ we expect to find them as descriptors of the slow decay of the survival probability of ER networks.

Since we aim to characterize the power-law behavior of the SP curves and the average degree fully conveys the localization-to-delocalization crossover of the eigenstates of the network, in Fig. 6.6 we show $SP(t)$ plots for different fixed average degree $\langle k\rangle$, from $\langle k\rangle = 2.07$ (see panel (a)) to $\langle k\rangle = 11.23$ (see panel (h)) and four ER network sizes n increasing from top to bottom. Magenta and cyan lines show the correlation dimension D_2 and the generalized dimension of the initial state $\widetilde{D}_2$, respectively (see Appendix A). We note that in panel (a) nor D_2 neither $\widetilde{D}_2$ match the decay of $SP(t)$, however as $\langle k\rangle$ increases t^{-D_2} predicts the decay at short times as we can see in panels (b, c, and d). Note, however, that the decay predicted as $t^{-\widetilde{D}_2}$ is more persistent when $\langle k\rangle = 4.27, 5.44$ and 6.92 (in panels (d-f)) as the $SP(t)$ curves follow that tendency for longer times, that is, as long as curves fall on on top of the other. Then we conclude that t^{-D_2} is a better decay indicator for small degrees $\langle k\rangle$ (e.g. $\langle k\rangle = 2.63, 3.35$ in panels (b and c)), while $t^{-\widetilde{D}_2}$ does it for $\langle k\rangle = 4.27, 5.44$ and 6.92. Also t^{-D_2} is a better decay indicator at short times ($t \approx 1$), while $t^{-\widetilde{D}_2}$ is a better indicator for longer times $1 < t < 10$. After panel (f) the curves do not fall as the generalized dimensions. Therefore, we can see that there exist only a small interval of $\langle k\rangle$ where the decay of the survival probability can be described by the generalized dimensions.

The full analysis of the generalized dimensions D_q and $\widetilde{D}_q$ is shown in Appendix A.

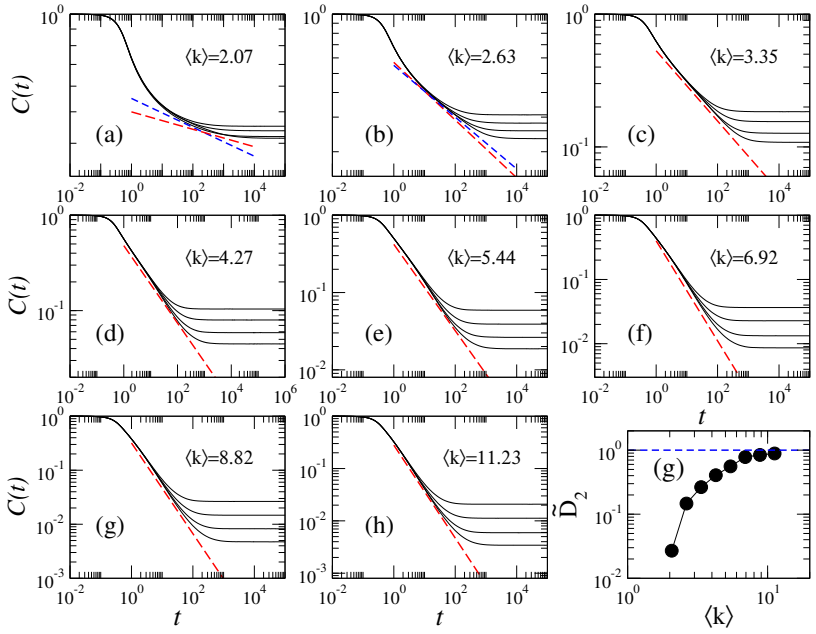

Figure 6.7: (a-h) Time-averaged survival probability $C(t)$ of ER networks for several values of the average degree $\langle k \rangle$. Graph sizes increase from top to bottom ($n = 250, 500, 1000$ and 2000). Red dashed lines depict $t^{\widetilde{D}_2}$ for each value of $\langle k \rangle$. In panel (a) blue dashed line depicts t^{D_2} for comparison. (g) Generalized dimension $\widetilde{D}_2$ of the initial state $|\phi_{ini}\rangle$ as a function of the average degree $\langle k \rangle$, where $\widetilde{D}_2 = 0.0269$(a), 0.1467(b), 0.2647(c), 0.4062(d), 0.5589(e), 0.7786(f), 0.8398(g), and 0.8873(h). The blue dashed line in panel (g) indicates the upper limit of $\widetilde{D}_2 = 1$.

On the other hand, the time-averaged survival probability also known as the temporal autocorrelation function [168] has been extensively used to analyze the dynamics of disordered systems at the mobility edge [168–170]. More recently, it has been applied to the study of the many-body localization transition in the 1D Heisenberg model [172]. In any case, it has been observed that the generalized dimension $\widetilde{D}_2$ directly governs the decay of the time-averaged survival probability, which follows a power law $\sim t^{-\widetilde{D}_2}$. Due to its relevance, the analysis of this quantity seems pertinent for our study. The time-averaged survival probability is defined as:

$$C(t) = \frac{1}{t} \int_0^t SP(\tau) d\tau. \tag{6.10}$$

Thus, in Figs. 6.7(a-h) we present the time-averaged survival probability $C(t)$ for the same values of the average degree $\langle k \rangle$ of Fig. 6.6. In every panel we show $t^{-\widetilde{D}_2}$ as red dashed

lines, illustrating that the decay of $C(t)$ is well-described by the generalized dimension $\widetilde{D}_2$. Notably, the best agreement is observed when $\langle k\rangle \geq 3.35$. Additionally, in panel (a-b), we include t^{-D_2} (blue dashed line) for comparison. As already observed in Figs. 6.6(a-b), this is a good indicator of the $SP(t)$ decay before saturation of the curves. Interestingly, it also proves to be a good descriptor for $C(t)$ in the same context. Then, $\langle k\rangle = 2.07$ and 2.63 are early stages in the crossover from localization to full delocalization. Finally, in panel (g) we present the generalized dimension $\widetilde{D}_2$ vs. $\langle k\rangle$, the curve illustrates the asymptotic transition to $\widetilde{D}_2 = 1$ (horizontal blue dashed line) as $\langle k\rangle$ increases. Here, we observe that the metallic regime is reached when $\langle k\rangle \approx 10$ as suggested in Fig. 6.9 in the analysis of the relative depth of the correlation hole in Subsection 6.3.4, and in Fig. 6.5 for the evolution of the SP.

6.3.3 Thouless time

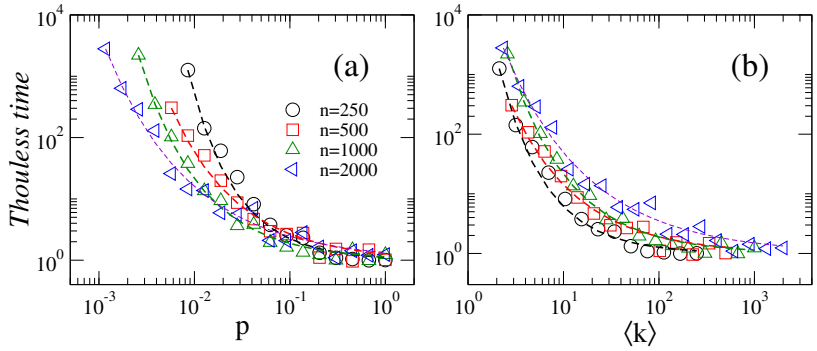

Figure 6.8: (a) Thouless time t_{Th} of ER networks for four different network sizes n in terms of the connection probability p, (b) and the average degree $\langle k\rangle$. Colored dashed lines in panels (a-b) correspond to fittings of Eq. (6.11) to the data; see Table 6.1.

As observed in Fig. 6.5, the correlation holes are displaced owing to the changes in the Thouless time, t_{Th}, and the relaxation time, t_R (the approximate time for the SP to reach its saturation value up to a relative error δ). As previously mentioned, the Thouless time t_{Th} is the time scale for the eigenvalues to fully correlate according to RMT. Thus, we estimate the Thouless time t_{Th} of ER networks of different sizes n as a function of the connectance p and the average degree $\langle k\rangle$ in Figs. 6.8(a-b), respectively. In Fig. 6.8(a) we observe that the smaller the size, the greater the connectance required to observe a displacement of t_{Th}. It should be also noted that as the size n increases, the value of the

Thouless time t_{Th} also increases as a function of $\langle k \rangle$ (see Fig. 6.8(b)). Despite of the possible fluctuations on the calculation of the critical time t_{Th} due to the lack of stability of the SP curves, as can be easily seen for every size n (colored symbols), we observe a rapid decay of the t_{Th} as the network becomes fully connected ($p \to 1$, $\langle k \rangle \to n-1$). Then in Figs. 6.8(a) and (b) we perform a fit to the numerical data as,

$$t_{Th} \approx e^{Ap^{-B}}, \tag{6.11}$$

where A and B are fitting constants; see Table 6.1. We must stress here, that t_{Th} fluctuations were unavoidable and their elimination may require much computing power. Thus, we expect a different correspondence of the expression to the numerical data for larger ensembles. As observed in Fig. 6.8(b), the t_{Th} exhibits an additional dependence on n since curves are displaced to the right on the $\langle k \rangle$ axis as n increases.

6.3.4 Correlation hole

The relative depth of the correlation hole has been used to detect the integrablility-chaos transition of disordered systems and more recently for the many-body localization phase in disordered interacting systems [173]. Therefore, the study of this quantity is relevant for us. The relative depth of the correlation holes is defined as:

$$\eta = \frac{\overline{SP} - SP_{min}}{\overline{SP}}. \tag{6.12}$$

Here, $\overline{SP}$ is the saturation value of the SP at very large times, and SP_{min} is the minimum value of the SP. In the case of the FRME (GOE), $\overline{SP} \approx 3/n$ and $SP_{min} \approx 2/n$. Then, we expect to observe a shift from $\eta \to 0$ when $p \to 0$ to $\eta \to 1/3$ when $p \to 1$. Thus, in Fig. 6.9(a-b) we present the relative depth of the correlation hole η of ER network ensembles in terms of the connection probability p and in terms of the average degree $\langle k \rangle$, respectively. It is observed that the larger the size of the network, the η curves saturate at earlier values of p. That is, the curves are displaced to the left in the p-axis as the size increases. As we plot η in terms of $\langle k \rangle$ all the curves fall one on top of the other, indicating that $\langle k \rangle$ is the scaling parameter of η. Moreover, as $\langle k \rangle > 10$, the relative depth of the correlation hole η reaches practically the GOE regime [58, 174] depicted by the magenta dashed line $\eta = 1/3$, this means that the metallic regime transition is well reflected in the η behavior. Since, the curves overlap we can find a heuristic expression that describes the η behavior. In this case,

we found that

$$\eta \approx \frac{1}{3}\left[1 - \exp\left\{-C\langle k\rangle^{D}\right\}\right] \tag{6.13}$$

describes the general behavior of η when $\langle k\rangle > 3$ as observed in Fig. 6.9(b). Here, C and D are fitting constants; see Fig.6.9(b).

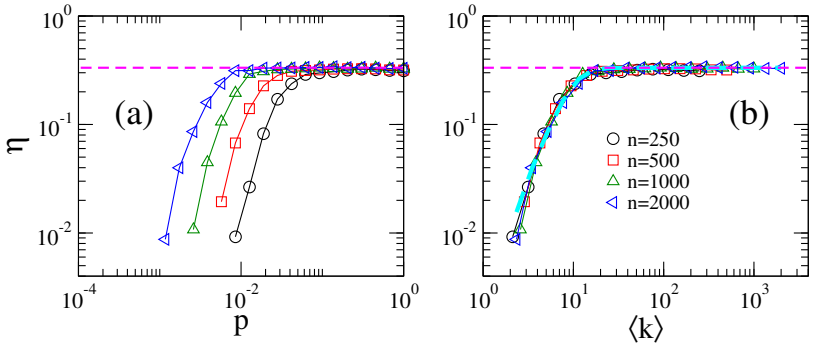

Figure 6.9: (a) Relative depth of the correlation hole η of the survival probability $SP(t)$ for ER networks as a function of the connection probability p and (b) as a function of the average degree $\langle k\rangle$. Cyan dashed line in panel (b) correspond to the best fit of Eq.(6.13), where $C = 0.008$ and $D = 2.186$ are the fitting values. Magenta dashed lines depicts the upper limit $\eta = 1/3$ of the GOE.

6.3.5 Saturation of the survival probability

In Figs. 6.10(d-e) we plot the inverse participation ratio of the initial state IPR_{ini} over $3/n$ for three different sizes $n = 250, 500$ and 1000 (represented by colored symbols) as a function of the connectance p and the average degree $\langle k\rangle$, respectively. Since the IPR_{ini} is the saturation value of the SP, the ratio $\mathrm{IPR}_{ini}/(3/n)$ shows the transition from diluted ensembles of matrices to the FRME as $\mathrm{IPR}_{ini}/(3/n) \to 1$. In this case we perform a similar fit to the numerical data as in Eq. (6.11) since the decay is also fast as the connectance p grows:

$$\mathrm{IPR}_{ini} \approx \frac{3}{n} e^{Ap^{-B}}. \tag{6.14}$$

Where A and B are fitting constants. Then, colored dashed lines in panels (d-e) correspond to the best fit to the numerical data for every size n; see Table 6.1.

Here, as in the case of the t_{Th} we stress that the variations of the saturation value IPR_{ini} will be lessen as the size of the ensemble becomes larger, so the correspondence to

	$\mathrm{IPR_{ini}}$		t_{Th}	
n	A	B	A	B
250	0.0240755	1.09585	0.104712	0.886255
500	0.00475391	1.28734	0.238992	0.615046
1000	0.00368026	1.22414	0.130568	0.684641
2000	0.0016593	1.23125	0.287341	0.491692

Table 6.1: Values of the fitting parameters A and B in Eqs. (6.14) and (6.11) as extracted from the curves $\mathrm{IPR_{ini}}$ vs. p and t_{Th} vs. p, respectively.

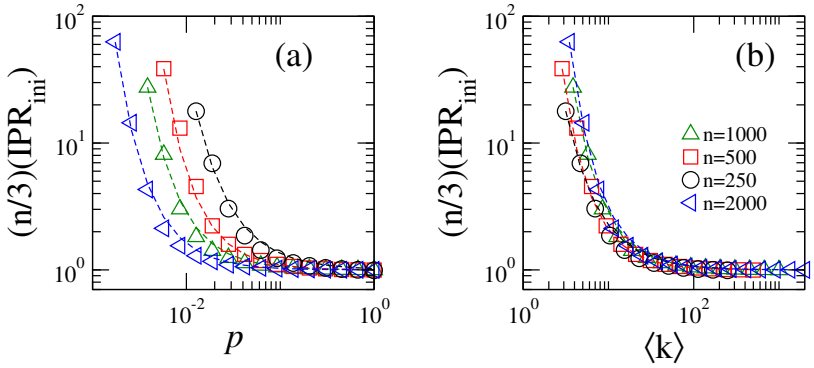

Figure 6.10: (a) Inverse participation ratio of the initial state IPR_{ini} over the FRME saturation value $(3/n)$ as a function of the connectance p and (b) as a function of the average degree. We report four different sizes denoted by symbols. Dashed colored curves indicate the best fit to the data as given by Eq. (6.14).

Eq. (6.14) may vary. Eq. (6.14) is an indicator of the tendency of the IPR_{ini} decay.

Chapter 7

Conclusions

In this thesis we studied structural, eigenvalue and eigenvector properties of two spatial random network models: the directed random geometric graph (dRGG) and the hyperbolic geometric graph (HRG). We also studied the survival probability of a reference random network model: the Erdös Renyi (ER) random model. All these studies where performed using random matrix theory ensembles as a numerical approach.

7.1 Conclusions of Part I

In the first part of this thesis, we performed an extensive numerical analysis of two random network models embedded in a geometric space: the directed random geometric graph and the hyperbolic random graph. First, we focused on the study of topological indices using large ensembles of binary adjacency matrices. Second we focused on the study of the eigenvector and eigenvalue properties of the models through the use of randomly-weighted adjacency matrices that transit from the Poisson ensemble to full random matrix ensembles when the network models transit from isolated to complete networks as a function of their inherent parameters. In this way, we enabled the analysis of standard measures from random matrix theory to the study of networks.

The directed random geometric graphs (dRGGs) were characterized by the parameter set (n, α, ℓ_0), where n is the number of vertices uniformly and independently distributed on the unit square, α is the power-law decay of the Pareto distribution that determines the connection radius of each vertex, and ℓ_0 is the lower bound of the Pareto distribution

support. We observed that by fixing (n, α), as ℓ_0 increased, the dRGGs transited from being isolated to fully connected. In the analysis of the structural properties of dRGGs, we found that for exponents $\alpha > 3$ the degree $k(G)$ is a self-averaging quantity, while it is not for $\alpha < 3$. Then, we were able to propose a phenomenological expression for the average degree $\langle k(G)\rangle$ (that stands as the summation of the out-degree and in-degree; see Eq. (2.9)), see Eq. (4.4) which indeed fails when k is a non-self-averaging quantity. Moreover, we demonstrated that the average number of nonisolated vertices of G, normalized to the graph size, $\langle V_x(G)\rangle/n$, perfectly scales with $\langle k\rangle$, following a quite simple relation, see Eq. (4.7). This fact, stresses the universality of Eq. (4.7) for random geometric graphs in both cases: directed and undirected versions. On the other hand, regarding spectral measures, we computed the standard spectral measures of random matrix theory by using two random matrix constructions: a non-Hermitian $\mathbf{A_{nH}}$ and a Hermitian $\mathbf{A_H}$ random matrix ensemble; see Eqs. (3.2) and Eq. (3.3). While the ensemble defined by $\mathbf{A_{nH}}$ corresponds to a diluted Real Ginibre Ensemble, we named the ensemble defined by $\mathbf{A_H}$ as the magnetic random matrix ensemble (MRME). Even though, both random matrix ensembles provide similar results, we found that the scaling of the eigenvalue and eigenvector properties of the dRGGs with $\langle k\rangle$ is observed in a wider range of α for the MRME.

As for the analysis of the hyperbolic random graphs (HRGs), we presented the graph model characterized by four parameters (n, ρ, α, ζ), where n is the number of vertices embedded inside the hyperbolic disk $\mathbb{H}^2$ of radius ρ, α determines the distribution of radial coordinates of the vertices, and ζ is the control parameter of the curvature; where $K = -\zeta^2$ is the gaussian curvature. We also computed structural and spectral properties of HRGs along the transition from isolated to fully connected networks. We were able to generalize the previously known expression for the number of non-isolated vertices $V_x(G)$, which we showed valid for Euclidean random geometric graphs in the undirected and undirected cases, see Eq. (4.7) and Eq. (5.7). We achieved this by the incorporation of a parameter that depends on the ratio α/ζ, see Eq. (5.8), thus validating the relevance of this ratio as the controller of heterogeneity of the network. This parameter α/ζ enabled the study of the HRGs in three regimes of heterogeneity: $\alpha/\zeta < 1/2$, $\alpha/\zeta = 1/2$, and $\alpha/\zeta > 1/2$. Thus, we performed numerical studies of this regimes without loss of generality by choosing $\alpha/\zeta = 0.2$, 0.5, and 1.5. In addition, we also computed average topological indices and clustering coefficients finding that $\langle k\rangle$ scales them properly when k is a self-averaging quantity. For the exploration of we spectral properties we used randomly-weighted adjacency

matrices of HRGs $G(n, \rho, \alpha, \zeta)$ represented by a Hermitian diluted random matrix ensemble that corresponds to the diluted GOE; see Eq. (3.1). We also found that while properly normalized average eigenvalue measures reasonably scale with the average degree $\langle k \rangle$, the average eigenvector measures needed the derivation of a compound scaling parameter that also incorporates the network size $\xi \equiv \xi(n, \langle k \rangle)$. The importance of this scaling parameter ξ relies on the fact that having universal curves for each quantity permits us to predict spectral properties of the models without actually computing them and to identify different regimes of the random network models as well: the localized regime, the localization-to-delocalization crossover, and the fully delocalized regime or metallic-regime. The derivation of the scaling parameter $\xi \equiv \xi(n, \langle k \rangle)$ was performed for both random network models: dRGGs and HRGs.

7.2 Conclusions of Part II

In the second part of this work, we have analyzed the survival probability of Erdös Renyi (ER) networks in the crossover from isolated nodes to full networks within a random matrix theory (RMT) approach. We have showed that the survival probability of ER networks exhibits an initial fast decay followed by power-law decay (which we called slow decay) before reaching the Thouless time or the correlation hole. In addition, we found that the inverse participation ratio of the initial state IPR_{ini}, the Thouless time t_{Th}, and the relative depth of the correlation hole η can be described by simple functions that depend solely on the parameters of the networks p and $\langle k \rangle$ as they transit from PE towards GOE limit values. Particularly, we observed that the relative depth of the correlation hole η is solely scaled by the average degree $\langle k \rangle$. We also showed that by fixing the average degree $\langle k \rangle$, the curves of the survival probability and curves of its time average fell one on top of the other for different network sizes before reaching their corresponding correlation hole. This allowed us to characterize in a general form the fast initial decay of the survival probability in terms of $\langle k \rangle$, and its slow decay as a power law of the correlation dimensions D_2 and $\widetilde{D}_2$. And in the case of the time-averaged survival probability we observed a full characterization of the power-law decay by the correlation dimension associated to the inital state $\widetilde{D}_2$, which is better for $\langle k \rangle > 3$. Finally, we showed that the ER model exhibits finite-size multifractality at every fixed value $\langle k \rangle$; see Appendix A.

We hope that this study may motivate further research on the application of RMT tech-

niques to the study of spectral and dynamical properties of different random network models by the use of randomly-weighted adjacency matrix ensembles.

Appendix A

Multifractal analysis of the Erdös Renyi network model

The multifractal nature of eigenstates in disordered systems at the Anderson transition is reflected in their spatial fluctuations. Lattice models, such as the Anderson tight-binding model, power-law random banded matrix (PRBM) models, and certain critical random matrix ensembles, have been extensively used to investigate the Anderson metal-insulator transition [175–177]. In particular, Anderson transition in random graph generic models have shown the existence of multifractal wave functions [178], and random networks represented as a diluted PRBM version have shown also multifractional eigencfunctions in [179]. An eigenstate is considered multifractal when it is extended but only covers a limited portion of the configuration space. The multifractality of these states is characterized by the generalized dimension D_q, where $D_q = 1$ corresponds to fully delocalized states, $0 < D_q < 1$ corresponds to multifractal states, and $D_q = 0$ corresponds to localized states. The generalized dimensions D_q quantify the spatial fluctuations of the eigenstates Ψ_i and are determined by the scaling of the averaged inverse participation ratio IPR with the size of the system n,

$$\langle \mathrm{IPR}(q) \rangle \equiv \begin{cases} \left\langle \sum_{i=1}^{n} |\Psi_i|^{2q} \right\rangle \sim n^{-(q-1)D_q}, & \text{for } q \neq 1, \\ \left\langle -\sum_{i=1}^{n} |\Psi_i|^2 \ln |\Psi_i|^2 \right\rangle \sim D_1 \ln n, & \text{for } q = 1. \end{cases} \tag{A.1}$$

Some studies of disordered noninteracting systems have shown that the survival probability [168, 169, 180] exhibits a power-law behaviour that is directly related to the

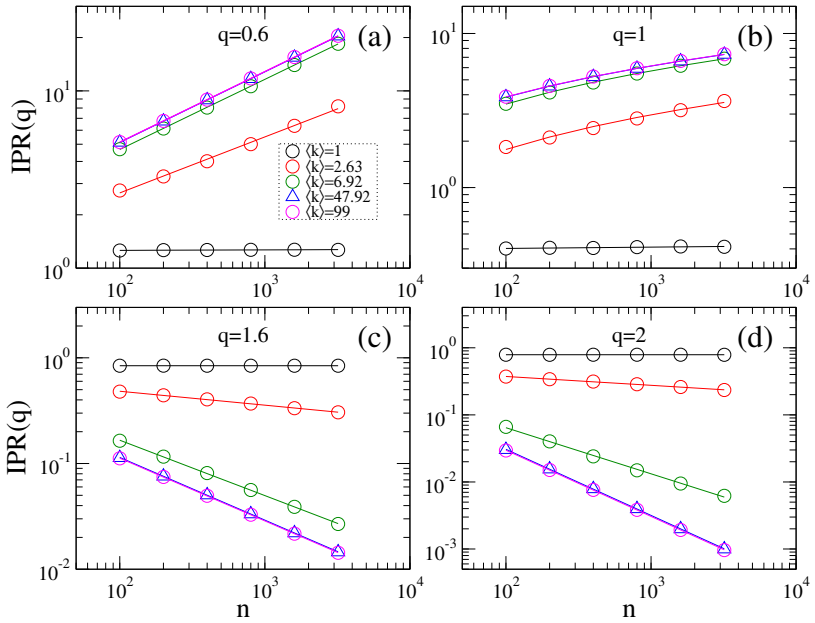

Figure A.1: Generalized participation ratio IPR(q) of ER network ensembles as a function of the network size n for (a) $q = 0.6$, (b) $q = 1$, (c) $q = 1.6$, and (d) $q = 2$. Several values of the average degree $\langle k \rangle$ are presented in every panel.

correlation dimension D_2. Also, in the study of dynamics at the Many-Body localization transition, the generalized dimension associated with the initial state $\tilde{D}_2$ has been related to the power-law decay of the survival probability in [172].

In this section, we compute the generalized dimensions D_q of the ER network model by setting the average degree $\langle k \rangle$ of every network ensemble. Since fully connected networks reach the GOE limit, we expect a transition in D_q from $D_q \to 0$ as $\langle k \rangle \to 0$ to $D_q \to 1$ as $\langle k \rangle \to n - 1$. For this, we average IPR(q) over an eigenvalue window of 20% of the matrix size and over $10^6/(0.2n)$ random realizations of the matrix. To compute D_q we have used six network sizes $n = 100, 200, 400, 800, 1600$, and 3200.

In Fig. A.1 we present plots of IPR(q) vs. n in log-log scale for different fixed average degrees $\langle k \rangle$ of ensembles of ER networks. In panels (a-b) we observe that as the average degree $\langle k \rangle$ increases the slope (D_q) of the IPR(q) vs. n curves grows. In panels (c-d) for $q > 1$ the sign of the slope changes according to Eq. (A.1) and decreases with $\langle k \rangle$. Not surprisingly, when $\langle k \rangle > 10$ the IPR(q) vs. n curves begin to overlap as we can see for $\langle k \rangle = 47.92$, and 99 in all panels. This indicates a transition to a metallic regime, consistent with the fact that for ER networks this transition occurs at $\langle k \rangle \approx 10$.

Finally, in all panels (a-d), when $\langle k \rangle = 1$, the slope is close to 0, meaning that the system is localized, further confirming that the average degree is below its delocalization transition value. Thus the generalized inverse participation ratio IPR(q) completely exhibits the fully delocalization transition (metallic regime) inherent of the network model as already discussed in the analysis of the correlation hole and critical Thouless time of the survival probability of the initial state $|\phi_{ini}\rangle$.

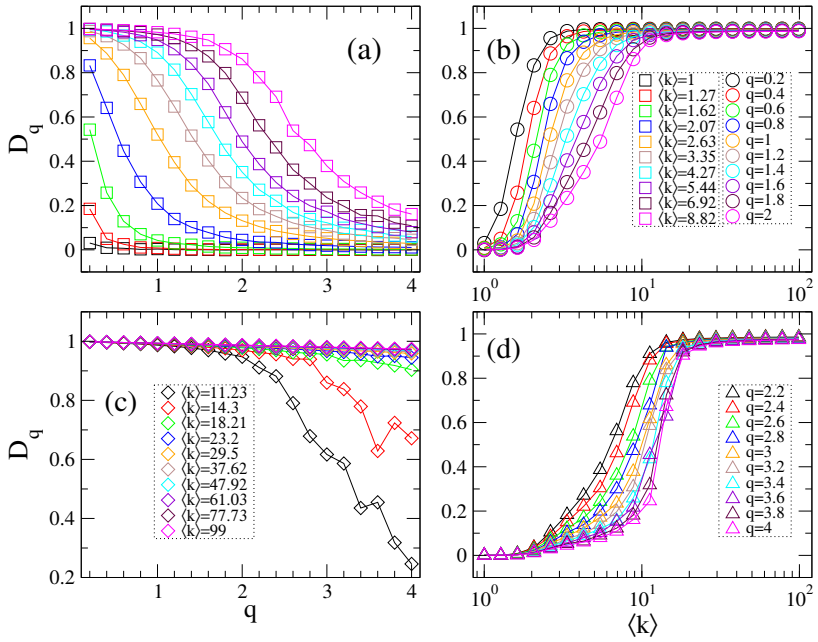

Figure A.2: (a), (c) Multifractal dimension D_q as a function of the parameter q of ER networks for several values of the average degree $\langle k \rangle$. (b), (d) Multifractal dimension D_q as a function of the average degree $\langle k \rangle$ for several values of the multifractal dimension q.

Following the scaling of equation (A.1) we obtain the generalized dimensions D_q of ER networks; see Fig. A.2. In panels (a, c) we present the generalized dimensions D_q in terms of the parameter q with fixed average degrees $\langle k \rangle$. We see that D_q decreases as the parameter q grows and the curves move upwards tending to $D_q \to 1$ as the average degree increases $\langle k \rangle$ (see square and diamond symbols). Also as $q \to 0$, D_q reaches its maximum value for a given $\langle k \rangle$. This shows that low values of $\langle k \rangle$ produce strongly localized eigenstates for all q, while extended states feel the entire system as the network structure is significantly changed with higher $\langle k \rangle$ values. Then in panels (b, d) we display D_q vs. $\langle k \rangle$, with $\langle k \rangle$ ranging from 1 to 99 for several values of q (see circle and triangle symbols), where curves transit from $D_q \to 0$ when $\langle k \rangle \to 1$ to $D_q \to 1$ when $\langle k \rangle$ grows. That is, a

transition from localized states to delocalized states is shown. Also the curves saturate at $D_q \to 1$ more quickly for lower values of q, with these curves being displaced to the left in the $\langle k \rangle$-axis.

Furthermore, the study of the survival probability has also been related to the generalized dimension of the initial state $|\phi_k\rangle$. This quantity is obtained in a similar way to D_2 by a scaling analysis of the inverse participation ratio of the initial state [172],

$$\langle \mathrm{IPR}(2) \rangle_{ini} = \left\langle \sum_{\beta} \left| C_{ini}^{\beta} \right|^4 \right\rangle \sim n^{-\tilde{D}_2}. \tag{A.2}$$

Bibliography

[1] L. Euler, Solutio problematis ad geometriam situs pertinentis. *Commentarii academiae scientiarum Petropolitanae*, 128-140, (1741).

[2] J. L. Gross, J. Yellen, and P. Zhang, *Handbook of Graph Theory Discrete Mathematics and Its Applications*, (CRC Press, 2nd edition, 2013).

[3] G. Kirchhoff, Über die Auflösung der Gleichungen auf welche man bei der Untersuchung der in einem galvanischen Kreise fließenden elektrischen Ströme geführt wird, *Annalen der Physik*, **148**(12), 497–508 (1847).

[4] R. Solomonoff and A. Rapoport, Connectivity of random nets *B. Math. Biophys.*, **13**, 107 (1951).

[5] P. Erdös and A. Rényi, On random graphs, *Publ. Math.*, (Debrecen) **6**, 290 (1959).

[6] O. Mülken and A. Blumen, Continuous-time quantum walks: Models for coherent transport on complex networks, *Phys. Rep.* **502**(2), 37 (2011).

[7] M. E. J. Newman, The structure and function of complex networks. *SIAM review* **45**(2), 167–256 (2003).

[8] J. Michel, S. Reddy, R. Shah, S. Silwal, and R. Movassagh, Directed random geometric graphs, *Journal of Complex Networks* **00** 1–25 (2019).

[9] O. Dousse *2012 IEEE Int. Symp. on Information Theory Proc.*, pp 601–605 (2012).

[10] S. Boccaletti, V. Latora, Y. Moreno, M. Chavez, and D. U. Hwang, Complex networks: Structure and dynamics, *Phys. Rep.* **424**, 175 (2006).

[11] L. da F. Costa, O. N. Oliveira Jr., G. Travieso, F. A. Rodrigues, P. R. Villas Boas, L. Antiqueira, M. P. Viana, and L. E. C. Rocha, Analyzing and modeling real-world phenomena with complex networks: a survey of applications, *Adv. Phys.* **60**, 329 (2011).

[12] M. Newmann, *Networks* (Oxford University Press, New York, 2nd edition, 2018).

[13] A. Barrat and M. Weigt, On the properties of small-world network models, *Eur. Phys. J. B* **13**, 547 (2000).

[14] D. Krioukov, F. Papadopoulos, M. Kitsak, A. Vahdat, and M. Boguñá, Hyperbolic geometry of complex networks, *Phys. Rev. E* **82**, 036106 (2010).

[15] A. L. Barabasi and R. Albert, Emergence of scaling in random networks, *Science* **286**, 509 (1999).

[16] D. J. Watts and S. H. Strogatz, Collective dynamics of small-world networks, *Nature* **393**(6684), 440 (1998).

[17] G. Caldarelli, A. Capocci, P. De Los Rios, and M. A. Munoz, Scale-free networks from varying vertex intrinsic fitness, *Phys. Rev. Lett.* **89**, 258702 (2002).

[18] B. Söderberg, General formalism for inhomogeneous random graphs, *Phys. Rev. E* **66**, 066121 (2002).

[19] M. Boguná and R. Pastor-Satorras, Class of correlated random networks with hidden variables, *Phys. Rev. E* **68**, 036112 (2003).

[20] C. Cannings, D.B. Penman, *Ch. 2. Models of random graphs and their applications, Handbook of Statistics*, (Elsevier, Volume 21, 51-91, 2023).

[21] M. Barthelemy, Spatial networks, *Phys. Rep.* **499**, 1 (2011).

[22] Y.-J- Zhang, K.-C Yang, and F. Radicchi, Model-free hidden geometry of complex networks, *Phys. Rev. E* **103**, 012305 (2021).

[23] G. Bianconi and C. Rahmede, Emergent hyperbolic network geometry, *Sci. Rep.* **7**, 41974 (2017).

[24] E. N. Gilbert, Random plane networks, *Journal of the society for industrial and applied mathematics* **9**(4), 533-543 (1961).

[25] M. Nekovee, Worm epidemics in wireless ad hoc networks, *New J. Phys.* **9**(6), 189 (2007).

[26] V. Isham, J. Kaczmarska, and M. Nekovee, Spread of information and infection on finite random networks, *Phys. Rev. E* **83**(4), 046128 (2011).

[27] M. Haenggi, J. G. Andrews, F. Baccelli, O. Dousse, and M. Franceschetti, Stochastic geometry and random graphs for the analysis and design of wireless networks. *IEEE J. Sel. Areas Commun.* **27**(7), 1029-1046 (2009).

[28] J. Dall and M. Christensen, Random Geometric Graphs *Phys. Rev. E* **66**, 016121 (2002).

[29] R. B. Ellis, J. L. Martin, and C. Yan, in Graph Drawing, edited by J Pach (Springer, Berlin, Heidelberg, 2005), GD 2004 (Lecture Notes in Computer Science, Vol. 3383, p. 167–172).

[30] K. Peralta-Martinez and J. A. Méndez-Bermúdez, Directed random geometric graphs: structural and spectral properties, *J. Phys. Complex.* **4**, 015002 (2023).

[31] A. Allen-Perkins, Random Spherical Graphs, *Phys. Rev. E* **98**, 032310 (2018).

[32] W. Whi, S. Ha, H. Kang, and D. S. Lee, Hyperbolic disc embedding of functional human brain connectomes using resting-state fMRI, *Netw. Neurosci.* **6**(3), 745–764 (2022).

[33] A. Allard and M. A. Serrano, Navigable maps of structural brain networks across species., *PLoS Comput. Biol.* **16**(2), 1007584 (2020).

[34] D. Krioukov, F. Papadopoulos, A. Vahdat, and M. Boguñá Curvature and temperature of complex networks, *Phys. Rev. E* **80**, 35101 (2009).

[35] G. García-Pérez, A. Allard, M. Á. Serrano, and M. Bogu˜ná, Mercator: uncovering faithful hyperbolic embeddings of complex networks, *New J. Phys.* **21**, 123033 (2019).

[36] M. Boguñá, F. Papadopoulos, and D. Krioukov, Sustaining the internet with hyperbolic mapping, *Nat. Commun.* **1**, 62 (2010).

[37] M. Kitsak, I. Voitalov, and D. Krioukov, Link prediction with hyperbolic geometry, *Phys. Rev. Res.* **2**, 043113 (2020).

[38] A. Rossi, S. Deslauriers-Gauthier, and E. Natale, Temporal Hyperbolic Graphs as Null Models for Brain Dynamics, The 12th International Conference on Complex Networks and their Applications - CNA 2023, (Menton, France, Nov 2023).

[39] Y. Moreno, M. Nekovee, and A. F. Pacheco, Dynamics of rumor spreading in complex networks, *Phys. Rev. E* **69**, 066130 (2004).

[40] R. G. Margiotta1, R. Kühn, and P. Sollich, Glassy dynamics on networks: local spectra and return probabilities *J. Stat. Mech.:Theory and Experiment* **2029**, 093304 (2019).

[41] P. Chelminiak, Return probability for random walks on scale-free complex trees, *Phys. Lett. A* **375**, 3114-3118 (2011).

[42] A. P. Riascos and J. L. Mateos, Random walks on weighted networks: Exploring local and non-local navigation strategies, *arXiv:1901.05609 [cond-mat.stat-mech]* (2019).

[43] A. P. Riascos and J. L. Mateos, Fractional dynamics on networks: Emergence of anomalous diffusion and Lévy flights, *Phys. Rev. E* **90**, 032809 (2014).

[44] A. P. Riascos and J. L. Mateos, Fractional quantum mechanics on networks: Long-range dynamics and quantum transport, *Phys. Rev. E* 92, 052814 (2015).

[45] O. Mülken and A. Blumen, Continuous-time quantum walks: Models for coherent transport on complex networks, *Physics Reports* **502**, 37-87 (2011).

[46] E. Estrada, d-Path Laplacians and Quantum Transport on Graphs, Mathematics **8**(4), 527 (2020).

[47] J. Wishart, The generalised product moment distribution in samples from a normal multivariate population, *Biometrika*, 32-52 (1928).

[48] E. P. Wigner, *Statistical properties of real symmetric matrices with many dimensions*,(Princeton University, 1957).

[49] E. P. Wigner, On the statistical distribution of the widths and spacings of nuclear resonance levels, *Proc. Cam. Phil. Soc.* **47**(4), 790 (1951).

[50] C. E. Porter and N. Rosenzweig, Statistical properties of atomic and nuclear spectra, *Ann. Acad. Sci. Fennicae, Ser. A, VI Physica* **44**, 1-66 (1960).

[51] C. E. Porter and N. Rosenzweig, Repulsion of energy levels in complex atomic spectra, *Phys. Rev.* **120**, 1698-1714 (1960).

[52] F. J. Dyson, The Threefold Way. Algebraic Structure of Symmetry Groups and Ensembles in Quantum Mechanics, *J. Math. Phys.* **3**, 1199 (1962).

[53] F. J. Dyson, A Brownian motion model for the eigenvalues of a random matrix, *J. Math. Phys.* **3**(6), 1191 (1962).

[54] F. J. Dyson, Statistical theory of the energy levels of complex systems. I, II, III, *J. Math. Phys.* **3**(1), 140, 157, 166 (1962).

[55] G. Akemann, J. Baik, and P. Di Francesco (Eds.), The Oxford handbook of random matrix theory (Oxford University Press, New York, 2011).

[56] Special issue editors, Special issue on random matrices. *J. Phys. A* **36**(12) (2003).

[57] D. Sherrington and S. Kirkpatrick, Solvable model of spin-glass, *Phys. Rev. Lett.* **35**(26), 1792 (1975).

[58] J. A. Mendez-Bermudez, A. Alcazar-Lopez, A. J. Martinez-Mendoza, F. A. Rodrigues, and T. K. DM. Peron, Universality in the spectral and eigenfunction properties of random networks, *Phys. Rev. E* **91**, 032122 (2015).

[59] R. Gera, L. Alonso, B. Crawford, J. House, J. A. Mendez-Bermudez, T. Knuth, and R. Miller, Spectral and localization properties of random bipartite graphs, *Appl. Net. Sci.* **3**, 2 (2018).

[60] A. J. Martínez-Mendoza, A. Alcazar-López, and J. A. Méndez- Bermúdez, Scattering and transport properties of tight-binding random networks, *Phys. Rev. E* **88**, 012126 (2013).

[61] A. D. Jackson, C. Mejia-Monasterio, T. Rupp, M. Saltzer, and T. Wilke, Spectral ergodicity and normal modes in ensembles of sparse matrices, *Nucl. Phys. A* **687**, 405 (2001).

[62] G. Rodgers and A. J. Bray, Density of states of a sparse random matrix, *Phys. Rev. B* **37**, 3557 (1988).

[63] G. Rodgers and C. deDominicis, Density of states of sparse random matrices, *J. Phys. A: Math. Gen.* **23**, 1567 (1990).

[64] Y. V. Fyodorov and A. D. Mirlin, On the density of states of sparse random matrices, *J. Phys. A: Math. Gen.* **24**, 2219 (1991).

[65] S. N. Evangelou and E. N. Economou, Spectral density singularities, level statistics, and localization in a sparse random matrix ensemble, *Phys. Rev. Lett.* **68**, 361 (1992).

[66] A. D. Mirlin and Y. V. Fyodorov, Universality of level correlation function of sparse random matrices, *J. Phys. A: Math. Gen.* **24**, 2273 (1991).

[67] S. N. Evangelou, A numerical study of sparse random matrices, *J. Stat. Phys.* **69**, 361 (1992).

[68] G. Semerjian and L. F. Cugliandolo, Sparse random matrices: the eigenvalue spectrum revisited, *J. Phys. A: Math. Gen.* **35**, 4837 (2002).

[69] A. Khorunzhy and G. J. Rodgers, Eigenvalue distribution of large dilute random matrices, *J. Math. Phys.* **38**, 3300 (1997).

[70] R. Kühn, Spectra of sparse random matrices, *J. Phys. A: Math. Gen.* **41**, 295002 (2008).

[71] T. Rogers, I. Peres-Castillo, and R. Kühn, Cavity approach to the spectral density of sparse symmetric random matrices, *Phys. Rev. E* **78**, 031116 (2008).

[72] F. Slanina, Equivalence of replica and cavity methods for computing spectra of sparse random matrices, *Phys. Rev. E* **83**, 011118 (2011).

[73] Y. V. Fyodorov and A. D. Mirlin, Localization in ensemble of sparse random matrices, *Phys. Rev. Lett.* **67**, 2049 (1991).

[74] Y. Kabashima, H. Takahashi, and O. Watanabe, Cavity approach to the fi

rst eigenvalue problem in a family of symmetric random sparse matrices, *J. Phys.: Conf. Series* **233**, 012001 (2010); Y. Kabashima, and H. Takahashi, First eigenvalue/eigenvector in sparse random symmetric matrices: Influences of degree fluctuation, *J. Phys. A: Math. Gen.* **45**, 325001 (2012).

[75] I. Neri, and F. L. Metz, Spectra of sparse non-hermitian random matrices: An analytical solution, *Phys. Rev. Lett.* **109**, 030602 (2012).

[76] J. A. Mendez-Bermudez, G. Ferraz-de-Arruda, F. A. Rodrigues, and Y. Moreno, Scaling properties of multilayer random networks, *Phys. Rev. E* **96**, 012307 (2017).

[77] J. A. Mendez-Bermudez, G. Ferraz-de-Arruda, F. A. Rodrigues, and Y. Moreno, Diluted banded random matrices: Scaling behavior of eigenfunction and spectral properties, *J. Phys. A: Math. Theor.* **50**, 495205 (2017).

[78] C. T. Martinez-Martinez, J. A. Mendez-Bermudez, Y. Moreno, J. J. Pineda-Pineda, and J. M. Sigarreta, Spectral and localization properties of random bipartite graphs, *Chaos Soliton Fract. X* **3**, 100021 (2019).

[79] C. T. Martinez-Martinez, T. Peron, J. A. Mendez-Bermudez, and Y. Moreno, Spectral and localization properties of random mutualistic graphs, *Chaos Soliton Fract. X* **3**, 100021 (2019).

[80] S. H. Strogatz, Exploring complex networks, *Nature* **410**, 268, (2001).

[81] R. Albert and A. L. Barabasi, Statistical mechanics of complex networks, *Rev. Mod. Phys.* **74**, 47 (2002).

[82] A. L. Barabasi, Network science, *Phil. Trans. R. Soc. A* **371**, 20120375 (2013).

[83] https://kids.frontiersin.org/articles/10.3389/frym.2019.00049#:~:text=The%20field%20for%20using%20networks,network%20are%20often%20used%20interchangeably.

[84] A.-L. Barabási, *Network Science*, (Cambridge University Press, 1st edition, 2016).

[85] I. Gutman, Degree-Based Topological Indices, *Croat. Chem. Acta* **86**(4), 351–361 (2013).

[86] L. B. Kier and L. H. Hall, *Molecular Connectivity in Chemistry and Drug Research*, (Academic Press, New York, 1976).

[87] D. T. Stanton, On the importance of topological descriptors in understanding structure–property relationships, *J Comput Aided Mol Des* **22**,441–460 (2008).

[88] H. Wiener, Structural determination of paraffin boiling points, *J. Am. Chem. Soc.* **69**, 17 (1947).

[89] C. Hansch, Quantitative approach to biochemical structure-activity relationships, *Acc. Chem. Res.* **2** 8, 232–239 (1969).

[90] H. M. Patel, M. N. Noolvi, P. Sharma, et al., Quantitative structure–activity relationship (QSAR) studies as strategic approach in drug discovery, *Med Chem Res* **23**, 4991–5007 (2014).

[91] A. Sabljic and M. Protic, Molecular connectivity: A novel method for prediction of bioconcentration factor of hazardous chemicals, *Chem. Biol. Interactions* **42**, 301–310 (1982).

[92] N. Trinajstif, *Chemical Graph Theory*, (CRC Press, Boca Raton, FL, 1985).

[93] R. D. Cramer III, BC(DEF) Parameters. 1. The intrinsic dimensionality of intermolecular interactions in liquid state, *J. Am. Chem. Soc.* **102**, 1837-1849 (1980).

[94] B. Bollobás and P. Erdös, *Ars Combin.*, Graphs of extremal weights **50**, 225 (1998).

[95] B. Bollobás, P. Erdös, and A. Sarkar, Extremal graphs for weights, *Discr. Math.* **200**, 5 (1999).

[96] Z. Du, A. Jahanbani, and S. M. Sheikholeslami, Relationships between Randić index and other topological indices, *Commun. comb. optim.* **6** 1, 137-154 (2021).

[97] L. B. Kier, L. H. Hall, Molecular connectivity: intermolecular accessibility and encounter simulation, *J. Mol. Graph. Model.* **20**, 76–83 (2001).

[98] M. Randic, The connectivity index 25 years after, *J. Mol. Graph. Model.* **20**, 19–35 (2001).

[99] M. Randić, Characterization of molecular branching, *J. Am. Chem. Soc.* **97**, 6609–15 (1975).

[100] P. de Meo, F. Messina, D. Rosaci, G. M. L. Sarné, and A. V. Vasilakos, Estimating graph robustness through the Randić index, *IEEE Trans. Cybern.* **99**, 1 (2017).

[101] N. Nikolova, and J. Jaworska, Approaches to measure chemical similarity a review, *QSAR Comb. Sci.* 22, 1006 (2003).

[102] E. Estrada, Quantifying network heterogeneity, *Phys. Rev. E* **82**, 066102 (2010).

[103] C. T. Martínez-Martínez, J. A. Méndez-Bermúdez, J. M. Rodríguez, and J. M. Sigarreta, Computational and analytical studies of the Randić index in Erdös–Rényi models, *Appl. Math. Comput.* **377**, 125137 (2020).

[104] S.Fajtlowicz, On conjectures of Graffiti, *Congr. Numer.* **60**, 187–97 (1987).

[105] S. Ediz, M. R. Farahani and M. Imran, On novel harmonic indices of certain nanotubes, *Int. j. adv. biotechnol. res.* **8** 4, 277-282 (2017).

[106] K. Sayehvand and M. Rostami, Further Results on Harmonic Index and Some New Relations Between Harmonic Index and Other Topological Indices, *J. Math. Computer Sci.* **11**, 123–136 (2014).

[107] O. Favaron, M. Maho, J. F. Sacl, Some eigenvalue properties in graphs (conjectures of Graffiti-II), *Discrete Math.* **111**, 197-220 (1993).

[108] M. S. Sardar, S. A. Xu, W. Sajjad, S. Zafar, I. N. Cangul, and M. R. Farahani, An explicit formula for the harmonic indices and harmonic polynomials of carbon nanocones CNC_k[n]. *J. INFORM. OPTIM. SCI.* **41** (4), 879-890 (2020).

[109] J. M. Rodríguez and J. M. Sigarreta, New Results on the Harmonic Index and Its Generalizations, *MATCH Commun. Math. Comput. Chem.* **78**, 387-404 (2017).

[110] R. Wu, Z. Tang and H. Deng, A lower bound for the harmonic index of a graph with minimum degree at least two. *Filomat* **27**(1), 51-55 (2013).

[111] L. Zhong, On the harmonic index and the girth for graphs. *Rom. J. Inf. Sci. Tech* **16**(4), 253-260 (2013).

[112] K. P. Narayankar, A. T. Kahsay and D. Selvan, Harmonic temperature index of certain nanostructures, *Int. j. math. trends technol.* **56**, 3 (2018).

[113] L. Yan, W. Gao and J. S. Li, General harmonic index and general sum connectivity index of polyomino chains and nanotubes, *J Comput Theor Nanosci* **12** 10, 3940-3944 (2015).

[114] R. Pradeep Kumar1, N. D. Soner, and M. R. Rajesh Kanna, Redefi

ned zagreb, Randic, Harmonic and GA Indices of Graphene, *Int. J. Math. Anal.* **11** 10, 493-502 (2017).

[115] R. Rasi and S. M. Sheikholeslami, The harmonic index of unicyclic graphs. Asian-European Journal of Mathematics **10**(03), 1750039 (2017).

[116] L. Zhong, K. Xu, The Harmonic index for bicyclic graphs, *Utilitas Math.* **90**, 23–32 (2013).

[117] L. Zhong, The Harmonic index for graphs, *Appl. Math. Lett.* **25** 3 561–566 (2012).

[118] R. Aguilar-Sánchez, J. A. Méndez-Bermúdez, F. A. Rodrigues, and J. M. Sigarreta, Topological versus spectral properties of random geometric graphs, *Phys. Rev. E* **102**, 042306 (2020).

[119] M. E. J. Newman, *Networks: An Introduction*, (Oxford University Press, New York, 2010).

[120] S. Wang, L. Huang, C. H. Hsu, and F. Yang, Collaboration reputation for trustworthy Web service selection in social networks, *Journal of Computer and System Sciences*, **82**(1), 130-143 (2016).

[121] Y. Wang, E. Ghumare, R. Vandenberghe, P. Dupont, Comparison of Different Generalizations of Clustering Coefficient and Local Efficiency for Weighted Undirected Graphs, *Neural Computation* **29**(2), 313–331 (2017).

[122] M. E. J. Newman, The structure of scientific collaboration networks, *Proc. Natl. Acad. Sci. USA* **98**, 404–409, (2001).

[123] S. Wasserman and K. Faust, *Social Network Analysis* (Cambridge University Press, Cambridge, 1994).

[124] A. E. Brouwer and W. H. Haemers, *Spectra of graphs.* (Springer, Science & Business Media, 2011).

[125] M. L. Mehta, *Random Matrices*, (Elsevier: Amsterdam, 2004).

[126] B. L. Altshuler and B. I. Shklovskii, Repulsion of energy levels and conductivity of small metal samples, *Sov. Phys. JETP* **64**, 127 (1986).

[127] J. Ginibre, Statistical Ensembles of Complex, Quaternion, and Real Matrices, *J. Math. Phys.* **6**, 440 (1965).

[128] D. J. Albers and J. C. Sprott, Probability of local bifurcation type from a fixed point: A random matrix perspective, *J. Stat. Phys.* **125**, 889 (2006).

[129] J. Feng, V. Jirsa, and M. Ding, Synchronization in networks with random interactions: theory and applications, *Chaos* **16**, 015109 (2006).

[130] P. J. Forrester and T. Nagao, Eigenvalue statistics of the real Ginibre ensemble, *Phys. Rev. Lett.* **99**(5), 050603 (2007).

[131] B. Ye, L. Qiu, X. Wang, and T. Guhr, Spectral statistics in directed complex networks and universality of the Ginibre ensemble, *Commun. Nonlinear Sci. Numer.* **20**(3), 1026-1032 (2015).

[132] E. H. Lieb and M. Loss, *Fluxes, Laplacians, and Kasteleyn's Theorem*, (B. Nachtergaele, J. P. Solovej, and J. Yngvason (eds), In Statistical Mechanics. Springer, Berlin, Heidelberg, (1993)).

[133] G. Berkolaiko, Nodal count of graph eigenfunctions via magnetic perturbation, *Analysis & PDE* **6**(5), 1213 (2013).

[134] M. Fanuel, C. M. Alaiz and J. A. Suykens, Magnetic eigenmaps for community detection in directed networks, *Phys. Rev. E* **95**(2), 022302 (2017).

[135] S. Furutani, T. Shibahara, M. Akiyama, K. Hato, and M. Aida, Graph signal processing for directed graphs based on the hermitian laplacian, (2020). (In Machine Learning and Knowledge Discovery in Databases: European Conference, ECML PKDD 2019, Würzburg, Germany, September 16–20, 2019, Proceedings, Part I (pp. 447-463). Springer International Publishing).

[136] K. Guo and B. Mohar, Hermitian adjacency matrix of digraphs and mixed graphs, *Journal of Graph Theory* **85**(1), 217-248 (2017).

[137] J. Liu and X. Li, Hermitian-adjacency matrices and Hermitian energies of mixed graphs, *Linear Algebra and its Applications* **466**, 182-207 (2015).

[138] Bruno Messias F. de Resende and Luciano da F. Costa, Characterization and comparison of large directed networks through the spectra of the magnetic Laplacian, *Chaos* **30**(7), 073141 (2020).

[139] M. Reed and B. Simon, *Methods of modern mathematical Physics I: Functional Analysis*, (Academic Press Inc, 1972)

[140] V. Oganesyan and D. A. Huse, Localization of interacting fermions at high temperature, *Phys. Rev. B—Condensed Matter and Materials Physics* **75**(15), 155111 (2007).

[141] Y. Y. Atas, E. Bogomolny, O. Giraud, and G. Roux, Distribution of the ratio of consecutive level spacings in random matrix ensembles, *Phys. Rev. Lett.* **110**(8), 084101 (2013).

[142] L. Sá, P. Ribeiro and T. Prosen, Complex spacing ratios: A signature of dissipative quantum chaos, *Phys. Rev. X* **10**(2), 021019 (2020).

[143] B. Mirbach and H. J. Korsch, A generalized entropy measuring quantum localization, *Annals of Physics* **265**(1), 80-97 (1998).

[144] C. E. Shannon, A mathematical theory of communication, *Bell Syst. Tech. J* **27**(3), 379–423 (1948).

[145] G. F. de Arruda, F. A. Rodrigues, and Y. Moreno, Fundamentals of spreading processes in single and multilayer complex networks *Phys. Rep.* **756**, 1-59 (2018).

[146] A. V. Goltsev, S. N. Dorogovtsev, J. G. Oliveira, and J. F. F. Mendes, Localization and Spreading of Diseases in Complex Networks, *Phys. Rev. Lett.* **109**, 128702 (2012).

[147] G. Ferraz de Arruda, J. A. Mendez-Bermudez, F. A. Rodrigues, and Y. Moreno, Universality of eigenvector delocalization and the nature of the SIS phase transition in multiplex networks, *J. Stat. Mech.*, 103405 (2020).

[148] T. Guhr, A. Müller-Groeling, H. A. Weidenmüller, Random-matrix theories in quantum physics: Common concepts, *Phys. Rep.* **299**, 189 (1998).

[149] T. Peron, B. M. F. de Resende, F. A. Rodrigues, L da F. Costa, and J. A. Mendez-Bermudez, Spacing ratio characterization of the spectra of directed random networks, *Phys. Rev. E* **102**, 062305 (2020).

[150] R. M. May, Will a large complex system be stable?, *Nature* **238**, 413 (1972).

[151] E. Estrada and M. Sheerin, Random rectangular graphs, *Phys. Rev. E* **91**, 042805 (2015).

[152] J. Diaz, D. Mitsche, and X. Perez, Large Connectivity for Dynamic Random Geometric Graphs, *IEEE Trans. Mob. Comput.* **8**, 821-35 (2009).

[153] K. Peralta-Martinez, J. A. Méndez-Bermúdez, and José M. Sigarreta, Hyperbolic random geometric graphs: Structural and spectral properties, *Phys. Rev. E* **111**, 024309 (2025).

[154] F. Papadopoulos, M. Kitsak, M. Á. Serrano, M. Boguñá, and D. Krioukov, Popularity versus similarity in growing networks, *Nature* **489**, 537 (2012).

[155] K. Zuev, M. Boguñá, G. Bianconi, and D. Krioukov, Emergence of soft communities from geometric preferential attachment, *Sci. Rep.* **5**, 9421 (2015).

[156] M. Á. Serrano, D. Krioukov, and M. Boguñá, Self-similarity of complex networks and hidden metric spaces, *Phys. Rev. Lett.* **100**, 078701 (2008).

[157] M. Bode, N. Fountoulakis, and T. Müller, The probability of connectivity in a hyperbolic model of complex networks, *Random Structures Algorithms* **49**, 65–94 (2016).

[158] C. T. Martinez-Martinez, J. A. Mendez-Bermudez, F. A. Rodrigues, and E. Estrada, Nonuniform random graphs on the plane: A scaling study, *Phys. Rev. E* **105**, 034304 (2022).

[159] C. Stegehuis, R. Van Der Hofstad, and J. S. Van Leeuwaarden, Scale-free network clustering in hyperbolic and other random graphs, *J. Phys. A: Math. Theor.* **52**, 295101 (2019).

[160] F. Borgonovi and F. M. Izrailev, Localized thermal states, *AIP Conf. Proc.* **1912**, 020003 (2017).

[161] E. J. Torres-Herrera, J. Karp, M. Távora, and L. F. Santos, Realistic many-body quantum systems vs. full random matrices: Static and dynamical properties *Entropy* **18**, 359 (2016).

[162] M. Schiulaz, E. J. Torres-Herrera, L. F. Santos, Thouless and relaxation time scales in many-body quantum systems, *Phys. Rev. B* **99**, 174313 (2019).

[163] M. Távora, E. J. Torres-Herrera, and L. F. Santos, Inevitable power-law behavior of isolated many-body quantum systems and how it anticipates thermalization, *Phys. Rev. A* **94**, 041603(R) (2016).

[164] M. Távora, E. J. Torres-Herrera, and L. F. Santos, Power-law decay exponents: A dynamical criterion for predicting thermalization, *Phys. Rev. A* **95**, 013604 (2017).

[165] E. J. Torres-Herrera, D. Kollmar, and L. F. Santos, Relaxation and thermalization of isolated many-body quantum systems, *Phys. Scr.* **T165**, 014018 (2015).

[166] L. Alonso, J. A. Mendez-Bermudez, A. Gonzalez-Melendrez, and Y. Moreno, Weighted random-geometric and random-rectangular graphs: Spectral and eigenfunction properties of the adjacency matrix, *J. Complex Netw.* **6**, 753 (2018).

[167] L. Erdös, A. Knowles, H-T. Yau, and J. Yin, Spectral statistics of Erdős–Rényi graphs I: Local semicircle law, *Ann. Probab.* **41**(3B), 2279-2375 (2013).

[168] R. Ketzmerick, G. Petschel, and T. Geisel, Slow decay of temporal correlations in quantum systems with Cantor spectra, *Phys. Rev. Lett.* **69**, 695 (1992).

[169] B. Huckstein and L. Schweitzer, Relation between the correlation dimensions of multifractal wave functions and spectral measures in integer quantum Hall systems, *Phys. Rev. Lett.* **72**, 713 (1994).

[170] G. Seng Ng, J. Bodyfelt, and T. Kottos, Critical fidelity at the metal-insulator transition, *Phys. Rev. Lett.* **97**, 256404 (2006).

[171] G. Palla and G. Vattay, Spectral transitions in networks, *New J. Phys.* **8**, 307 (2006).

[172] E. J. Torres-Herrera and L. F. Santos, Dynamics at the many-body localization transition, *Phys. Rev. B* **92**, 014208 (2015).

[173] E. J. Torres-Herrera and L. F. Santos, Dynamical manifestations of quantum chaos: correlation hole and bulge, *Phil. Trans. R. Soc. A* **375**, 20160434 (2017).

[174] G. Torres-Vargas, R. Fossion and J. A. Méndez-Bermúdez, Normal mode analysis of spectra of random networks, *Physica A* **545**, 123298 (2020).

[175] J. A. Méndez-Bermúdez, A. Alcázar-López, and I. Varga, Multifractal dimensions for critical random matrix ensembles, *EPL* **98**, 37006 (2012).

[176] F. Evers and A. D. Mirlin, Anderson transitions, *Rev. Mod. Phys.* **80**, 1355 (2008).

[177] A. D. Mirlin, Y. V. Fyodorov, F. M. Dittes, J. Quezada, and T. H. Seligman, Transition from localized to extended eigenstates in the ensemble of power-law random banded matrices, *Phys. Rev. E* **54**, 3221 (1996).

[178] I. García-Mata, O. Giraud, B. Georgeot, J. Martin, R. Dubertrand, and G. Lemarié, Scaling theory of the Anderson transition in random graphs: Ergodicity and universality, *Phys. Rev. Lett.* **118**, 166801 (2017).

[179] D. A. Vega-Oliveros, J. A. Méndez-Bermúdez and F. A. Rodrigues, Multifractality in random networks with power-law decaying bond strengths, *Phys. Rev. E* **99**, 042303 (2019).

[180] B. Huckestein and R. Klesse, Wave-packet dynamics at the mobility edge in two- and three-dimensional systems, *Phys. Rev. B* **59**, 9714 (1999).

[181] A. K. Das, A. Ghosh and I. M. Khaymovich, Emergent multifractality in power-law decaying eigenstates, *arXiv preprint arXiv:2501.17242* (2025).

[182] G. De Tomasi, M. Amini, S. Bera, I. M. Khaymovich, and V. Kravtsov, Survival probability in Generalized Rosenzweig-Porter random matrix ensemble, *SciPost Physics* **6**(1), 014 (2019).